THESIS FOR THE DEGREE OF DOCTOR OF PHILOSOPHY

Oxidative dissolution of UO_2 by α-radiolysis

Niklas L. Hansson

Department of Chemistry and Chemical Engineering
CHALMERS UNIVERSITY OF TECHNOLOGY
Göteborg, Sweden 2022

Oxidation of UO_2 by α-radiolysis
NIKLAS L. HANSSON

ISBN: 978-91-7905-682-7

Doktorsavhandlingar vid Institutionen för Kemi och Kemiteknik
Chalmers tekniska högskola
Ny serie nr 5148
ISSN: 0346-718X

Nuclear Chemistry
Department of Chemistry and Chemical Engineering
Chalmers University of Technology
SE-412 96 Gothenburg
Sweden
Telephone +46 (0)31-772 1000

Cover: Valence band region showing the O2p and U5f peaks of the UO_2 pellets exposed to the 1.85 and 3.30 MBq Am-241 sources under Ar atmosphere.

Printed by:
Chalmers Digitaltryck
Gothenburg, Sweden 2022

Oxidation of UO_2 by α-radiolysis

NIKLAS L. HANSSON

Nuclear Chemistry
Department of Chemistry and Chemical Engineering
Chalmers University of Technology

Abstract

To prevent the spread of radiotoxic nuclides in the environment, spent nuclear fuel generated by decades of nuclear power operation must be safely stored for at least 100 000 years. The KBS-3 method is a highly developed deep geological repository concept and is the first final repository design for high-level nuclear waste to be constructed. It contains a number of engineered barriers designed to prevent groundwater from coming into contact with the spent nuclear fuel. However, the consequences of groundwater coming into contact with the fuel must be considered when assessing the safety of this repository concept. After ~1000 years, the initially dominant γ-emitting elements have largely decayed, and the α-emitters dominate the radiation field. At the fuel-water interface, the fuel's strong α-radiation field causes extensive radiolysis, creating locally oxidizing conditions. The oxidants formed can cause oxidation of the UO_2 matrix from the U(IV) state to the U(VI) state, significantly increasing its solubility in the process. The water intrusion also leads to anoxic corrosion of the iron inserts, forming large amounts of H_2 in the process. This process has been shown to protect nuclear fuel against oxidative dissolution.

The oxidative dissolution of UO_2-based materials has been experimentally studied and modelled in this work. Oxidation and dissolution of UO_2 pellets were studied under an external irradiation source, in both Ar and H_2 atmospheres. In the Ar atmosphere, the oxidation of UO_2 was shown to take place through the incorporation of a significant U(V) oxidation state fraction. In the H_2 atmosphere, the surface was protected during exposure to the external irradiation source against both surface oxidation and dissolution. Very low dissolution yields were found in the study of SIMFUEL, with H_2 catalytically activated on the pellet surface, efficiently causing catalytic decomposition of H_2O_2 without leading to oxidative dissolution of the UO_2 matrix. Highly Pu-doped MOX pellets showed a strong oxidative dissolution in the Ar atmosphere. This was somewhat mitigated in the D_2 atmosphere. The modelled data were shown to accurately replicate the experimental results. Dissolved U(VI) was shown to be strongly reductively precipitated on corroding iron foils under anoxic conditions. This decreased the initially dissolved concentrations by three orders of magnitude over relatively short periods.

This work furthers the understanding of oxidative dissolution of UO_2-based materials under α-radiation fields and the effect of reducing agents present in the canister.

Keywords: UO_2, MOX, α-radiolysis, hydrogen effect, ε-particles, dose rate, kinetics

List of Publications

This thesis is based on the following papers and manuscripts:

Paper I

Bauhn, L., **Hansson, N.**, Ekberg, C., Fors, P., Delville, R., & Spahiu, K. (2018). The interaction of molecular hydrogen with α-radiolytic oxidants on a $(U,Pu)O_2$ surface. *Journal of Nuclear Materials*, *505*, 54-61. https://doi.org/10.1016/j.jnucmat.2018.04.006

Contribution: main part of the experimental work, part of the writing.

Paper II

Bauhn, L., **Hansson, N**., Ekberg, C., Fors, P., & Spahiu, K. (2018). The fate of hydroxyl radicals produced during H_2O_2 decomposition on a SIMFUEL surface in the presence of dissolved hydrogen. *Journal of Nuclear Materials*, *507*, 38-43. https://doi.org/10.1016/j.jnucmat.2018.04.028

Contribution: part of the experimental work, part of the writing.

Paper III

Hansson, N., Tam, P. L., Ekberg, C., & Spahiu, K. (2021). XPS study of external α-radiolytic oxidation of UO_2 in the presence of argon or hydrogen. *Journal of Nuclear Materials*, *543*, 152604. https://doi.org/10.1016/j.jnucmat.2020.152604

Contribution: lead author. Most of the experimental work, analysis and data evaluation.

Paper IV

Hansson, N., Jonsson, M., Ekberg, C., & Spahiu, K. (2022). Geometrical Aspects of Alpha Dose Rates from UO_2 Based Fuels. *Radiation Physics and Chemistry, 199,* 110336, https://doi.org/10.1016/j.radphyschem.2022.110336

Contribution: lead author, all modelling, most writing and conceptualization.

Paper V

Hansson, N., Jonsson, M., Ekberg, C., & Spahiu, K. (2022). A novel numerical modelling approach for radiation-induced oxidative dissolution of UO_2-based spent nuclear fuel. *Journal of Nuclear Materials.* Submitted.

Contribution: lead author, all modelling, main part of the writing. Conceptualization by all authors.

Paper VI

Hansson, N., Ekberg, C., & Spahiu, K. (2022). Oxidative dissolution of highly doped MOX under D_2 and Ar atmospheres. *Journal of Nuclear Materials.* Submitted.

Contribution: lead author, all experimental work and analysis. Main part of the writing.

Paper VII

Hansson, N., Saleh, M., Tam, P. L., Ekberg, C., & Spahiu, K. (2022). Influence of groundwater composition on the reductive precipitation of U(VI) on corroding iron foil surfaces. Manuscript. *Journal of Nuclear Materials*. Submitted.

Contribution: lead author. Most experimental work and analysis.

Paper VIII

Hansson, N., Jonsson, M. (2022). Exploring H_2-effects on radiation-induced oxidative dissolution of UO2-based spent nuclear fuel using numerical simulations. Manuscript.

Contribution: lead author. All modelling and part of the writing.

Related publications not covered in this thesis:

Hansson, N., Ekberg, C., & Spahiu, K. (2020). Alpha dose rate calculations for UO_2 based materials using stopping power models. *Nuclear Materials and Energy*, *22*, 100734. https://doi.org/10.1016/j.nme.2020.100734

Contribution: lead author. All experimental work, modelling, and main part of writing and conceptualization.

Table of Contents

1. Introduction

Global electricity demand is increasing, with 6% growth during 2021. This constitutes a new record in absolute terms [1]. In the same year, CO_2 emissions from electricity generation increased by almost 7%, largely due to cheap, coal-fired electricity production [1]. Facing the climate crisis, low-carbon electricity production has a crucial role to play in the transition to a sustainable global energy system. One such production source is nuclear power, which constitutes approximately 10% of global electricity production [2]. It is estimated to have prevented 60 gigatonnes of CO_2 emissions over the last 50 years, equivalent to almost two years' worth of global energy emissions [3]. Henceforth, it may play an important role in transforming the global energy system. However, nuclear power faces a number of challenges, such as large capital costs for new nuclear power constructions and rather low public support [4, 5]. An important factor for the latter has been severe nuclear accidents, such as the 2011 Fukushima Daiichi disaster. This led to a large-scale shutdown of nuclear power globally and halted or cancelled construction plans [6]. Furthermore, nuclear power generates long-lived highly radioactive waste which must be safely stored for substantial periods to ensure that radiotoxic nuclides do not spread to the environment. Due to the long half-lives of the actinides, this period amounts to roughly 100 000 years before radiotoxicity has reached that of the mined uranium ore used to make fuel. The design and safety assessment of final repositories remains one of the main challenges of nuclear power [4].

In Sweden, nuclear power constitutes 30% of the country's electricity production, with a total capacity of 6885 MWe as of April 2022 [7]. In Sweden and Finland, the KBS-3 repository concept has been accepted for construction, and in Finland's case is already under construction [8]. In this design, spent nuclear fuel (SNF) is encapsulated in copper canisters, which are buried ~500 m deep in the granitic bedrock and surrounded by compacted bentonite clay. Despite well-engineered barriers designed to prevent groundwater from reaching the SNF, the most credible route for radionuclide transport into the biosphere is through groundwater. Therefore, as part of the safety analysis, the water-intrusion scenario must be thoroughly investigated [9]. After roughly 1000 years, α-radiation dominates the SNF's radiation field [10]. Due to the high radioactivity of the nuclear fuel, extensive radiolysis occurs at the UO_2-H_2O interface leading to oxidizing conditions due to the strong oxidizing nature of H_2O_2. The nuclear fuel bundles are housed in massive iron inserts within the copper canisters. These inserts corrode extensively under anoxic conditions, forming significant amounts of iron corrosion products and H_2, both of which can strongly mitigate the effect of radiolytic oxidants on the fuel. H_2 is catalytically activated on metallic fission product particles on the surface of the spent nuclear fuel, making it a strong reducing agent, and iron can efficiently reductively precipitate oxidized UO_2. However, the influence of these reducing effects depend on the chemical state and composition of the UO_2-based material, as well as groundwater composition. Furthermore, recent improvements in the understanding of the oxidative dissolution of UO_2 by H_2O_2 have been made.

This work studies nuclear fuel models and their behavior in synthetic groundwaters. The work focuses on α-emitting UO_2-based materials, from which the dose rate and radiolytic production is modelled (Paper IV). The oxidation of the U(IV)O_2 surface from an external α-radiation

source was studied (Paper III), plus the release of oxidized uranium as $U(VI)O_2^{2+}$ (Papers I, III and VI). Moreover, the effect of H_2 on the α-radiolysis-induced UO_2 and MOX dissolution was studied (Papers I, III and VI) as well as H_2 activated on ε-particles (Papers II and VIII). The reducing effect of corroding iron on the stability of dissolved U(VI) was also investigated (Paper VII). The oxidation mechanism of UO_2 was modelled using a combined radiolysis, diffusion and kinetic model which was compared to experimental data (Papers V and VIII). A summary of the contents appears in Figure 1.1.

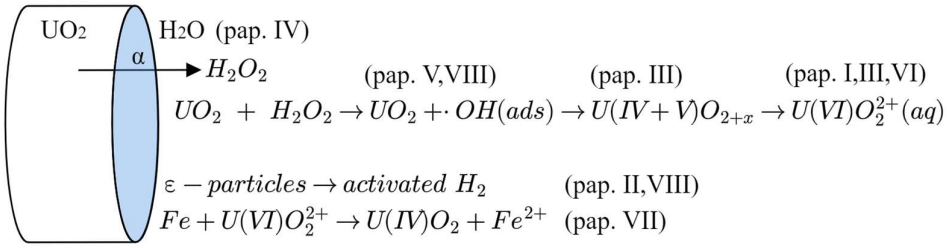

Figure 1.1. Summary of the concepts covered in this thesis. The chemical reactions are to illustrate the different steps in the oxidation of UO_2, and are unbalanced.

2. Background

2.1. Uranium

Since Roman times, uranium compounds have been used as colorants for glasses and ceramics [11]. The element was first identified by Klaproth in 1789, and later isolated by Peligot in 1841 [12]. In 1896, Henri Becquerel discovered that uranium emits penetrating radiation, a property later named radioactivity by Marie and Pierre Curie [11]. Uranium is relatively abundant in the earth's crust, with a concentration of 2-3 ppm [13]. It is more abundant than silver, cadmium, antimony, and mercury [12]. It is present in a wide variety of minerals [14], notably pitchblende [12]. It is present as the isotopes U-234 ($t_{½}$=2.46·10^5 y), U-235 ($t_{½}$=7.04·10^8 y) and U-238 ($t_{½}$=4.47·10^9 y) with abundances of 0.005 at.%, 0.72 at.% and 99.275 at.% respectively [15], giving an atomic weight of natural uranium of 238.0289±0.0001 [11]. The principal oxidation states are U(IV), U(V) and U(VI). Uranium is largely insoluble in the U(IV) state, and can be oxidized into the more soluble U(V) and U(VI) states. U(VI)O_2 exists as the linear $(O=U=O)^{2+}$ moiety, which is highly soluble in the presence of e.g., hydroxides or carbonates. Due to the high solubility of the U(VI) form, uranium is present in seawater at concentrations of 3 ppb [13].

2.2. Nuclear fuel

UO_2 is highly suitable as a nuclear fuel, as it has a high melting point, does not undergo phase transformations with increased temperature (unlike metallic uranium), and is highly stable under irradiation [16]. However, its heat conductivity is rather poor, which constrains the maximum pellet size [16, 17]. UO_2 pellets are produced by pressing powders and then sintering at high temperatures (~1700 °C) under reducing conditions. This achieves a density close to 95% of the theoretical value for freshly produced UO_2 pellets [11, 18]. The freshly produced nuclear fuel is slightly hyper-stoichiometric, and consists of UO_{2+x} with x being approximately 0.05 [18]. This slight hyper-stoichiometry takes the form of interstitial oxygen, which can occupy two different lattice positions [11]. Pellets sintered at ~1700 °C are resistant to oxidation through the formation of a thin, slightly oxidized protective surface film [11].

2.3. Nuclear reactors

In light water reactors (LWR), which are of two principal designs, boiling water reactors (BWR) and pressurized water reactors (PWR), heat is generated through the fission reaction, in which a neutron splits a heavy nucleus into fission fragments. In both light and heavy water reactors, the nuclear fuel is almost exclusively UO_2 [16]. In the U-235 fission reaction, a large amount of energy, ~200 MeV (equivalent to 2·10^7 kWh·kg^{-1}) is released as kinetic energy distributed between the fission products and neutrons [11]. In most LWR's, the enrichment level of U-235 is 3-5%, which is achieved almost entirely through the gaseous diffusion and gaseous centrifugation processes [19]. The fission reaction of U-235 can be expressed as:

$$ {}^{1}_{0}n + {}^{235}_{92}U \rightarrow {}^{A_1}_{Z_1}FP_1 + {}^{A_2}_{Z_2}FP_2 + x\ {}^{1}_{0}n + energy \quad (1) $$

where x is ~2.5 [20]. The fission product yield distribution has two peaks centered around mass numbers 97 and 137 [21]. The neutrons generated are used to sustain a fission chain-reaction. This must be carefully maintained at criticality by controlling the neutron economy, to ensure that the number of neutrons does not significantly increase over the duration of a neutron generation. The highly abundant U-238 is fertile, meaning it can undergo the neutron capture (n,γ) reaction, whereby the U-238 nucleus absorbs a neutron, forming the less stable U-239:

$$ {}^{1}_{0}n + {}^{238}_{92}U \rightarrow {}^{239}_{92}U + \gamma \tag{2} $$

U-239 undergoes β^--decay, leading to the formation of Pu-239 ($t_{½}$=24.110 y):

$$ {}^{239}_{92}U \xrightarrow{\beta^-} {}^{239}_{92}Np \xrightarrow{\beta^-} {}^{239}_{92}Pu \tag{3} $$

which is fissile [11], contributing to the neutron economy and energy generation. The neutron absorption reaction also results in the formation of other heavier actinides, such as neptunium, americium and curium [14].

2.4. Plutonium

Plutonium was first synthesized in 1940 by Seaborg et al. [22] by bombarding uranium with deuterons. Less than five years later, plutonium was used in the first nuclear weapons, profoundly impacting the course of human history [23]. In nuclear reactors, large amounts of plutonium are produced through the neutron absorption reaction, and can be separated out. Over 2000 metric tons of plutonium exist globally, and must be carefully managed [23]. In addition to electricity generation, certain isotopes of plutonium have been used as a power source in pacemakers, and in space exploration missions [12, 23]. It has a highly complex chemistry, with six possible oxidation states, four of which may occur simultaneously in solution [23].

2.5. Spent nuclear fuel

A light-water reactor typically generates 20-30 metric tons of spent nuclear fuel (SNF) per year [24], leading to a considerable global accumulation of SNF. In terms of oxidation state, the irradiated fuel is very close to stoichiometric UO_2. The radioactivity of the fuel increases by a factor 10^6 during irradiation as compared to the slightly enriched fresh UO_2 fuel [25]. This extremely radioactive fuel must be handled and stored safely, as a person standing next to a freshly spent nuclear assembly would sustain lethal exposure in under a minute [24, 25]. The radiotoxicity (in units Sv/metric ton of used fuel) of the actinides and fission products generated in 4% U-235 enriched nuclear fuel with 45 MWd/kg burnup was modelled by Holm [26] (Figure 2.1). It takes somewhat over 10^5 years for the SNF to reach the defined reference level for radiotoxicity of mined uranium. The fission products constitute most of the radiotoxicity during the initial 100 years, after which the transuranic actinides and their decay chain daughters dominate, up until approximately a million years.

The SNF may be chemically treated to extract plutonium and uranium. This has been done on an industrial scale since 1954 by using TBP (tributyl phosphate) in the PUREX process [27].

The streams extracted from this processing may be used in the manufacturing process of new fuel, such as mixed-oxide fuels (MOX).

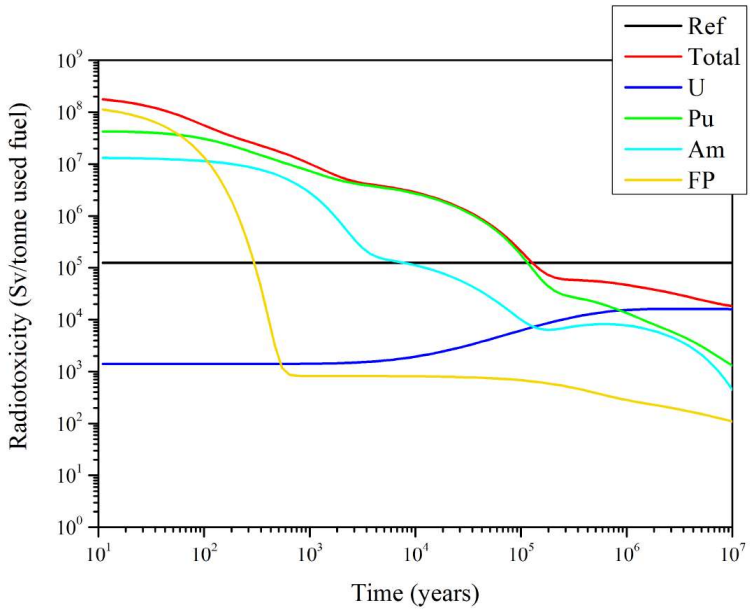

Figure 2.1. Radiotoxicity of the actinides and fission products of 4% enriched nuclear fuel with 45 MWd/kg burnup [26]. The reference level shown in black refers to the radiotoxicity of mined uranium.

2.6. Fission products

The fission products can be separated into groups according to their solubility in the UO_2 matrix. In order of decreasing solubility [28, 29] these are:

i. Soluble fission products such as lanthanides and minor actinides. The vast majority of radionuclides belong in this category. The release of the elements in this category depends on the dissolution of the UO_2 matrix.

ii. Fission products that accumulate in grain boundaries, forming metallic precipitates such as ε-particles consisting of Mo, Ru, Rh, Tc, and Pd. The perovskite phase $(Ba/Sr)ZrO_3$ also belongs to this category, despite Zr not being present solely as the perovskites phase but dissolved to a lesser extent (~25%) in the UO_2 matrix [29].

iii. Highly volatile fission products, such as Ar, Kr, Xe, and to lesser extent Cs and I. These migrate to the fuel gap and constitute the instant release fraction [25, 30], which is rapidly released in the case of canister failure. The volatile fission products constitute the bulk of the activity during the SNF's early stages. Considering the quick release and significant volatility of these species, the repository must sustain the initial few hundred years without structural compromise.

2.7. Deep geological repository

Radioactive waste is categorized according to its decay rate and initial radioactivity level. The commonly used categories are low, intermediate, and high-level waste, with subcategories of short or long-lived [31]. The Swedish Nuclear Fuel and Waste Management Company (SKB), uses three combined categories:

i. high-level, long-lived waste.
ii. low and intermediate level long-lived waste (from e.g. decommissioning of nuclear installations).
iii. low and intermediate level short-lived operational waste.

Depending on which category the waste belongs to, it is sent for disposal to repositories of different designs [31]. Waste in category (iii) is stored in the final repository for short-lived radioactive waste, SFR at Forsmark. SNF belongs in the high-level, long-lived waste category, the repository design for which is engineered to a much higher standard than the other repositories, as it should safely contain the waste for one million years [31]. These extreme periods are very hard to predict accurately by extrapolating experimental data, without there being substantial uncertainties. It is, therefore, very useful to study the behavior of UO_2 and other actinides in the environment. The most relevant case is the uranium-rich deposits in Oklo, Gabon, which sustained a natural fission chain reaction approximately two billion years ago [32]. The chain reaction was intermittently critical, through cycles of evaporating the moderating water, after which the reactor sites regained sufficient moderator to reach criticality again. The variety of mineral types present in the host rocks makes the reactor sites highly suitable analogs for the migration of long-lived actinides. The radionuclides were found to be very largely retained at the reaction site, showing the migration of both actinides and fission products to be highly limited [32]. This implies that the deep geological repository design is highly suitable for the extended time storage required for SNF.

SKB and Posiva Oy jointly developed and researched the KBS-3 geological repository concept, designed for the safe disposal of high-level, long-lived waste. The concept consists of three main barriers, the 5 cm thick copper canister, the bentonite buffer, and the crystalline bedrock [33]. The UO_2 fuel itself could also potentially be considered a barrier, due to the low solubility of the UO_2 matrix under reducing conditions. The filled copper canister has an estimated total weight of 24600 kg, of which the iron insert represents ~13600 kg, the copper canister itself ~7400 kg, and the nuclear fuel bundles (BWR reactor) ~3600 kg [33]. The repository will be constructed at a depth of 500 m, with a tunnel system used to deposit the canisters in drill holes. A general overview of the KBS-3 design is shown in Figure 2.2.

At the repository's depth, the conditions will be completely anoxic relatively soon after closure through reactions with organic material, minerals, and the copper canisters [34, 35]. The canister breach scenario followed by groundwater intrusion is considered in the main safety report on the SR-Site project by SKB, and is summarized as two main scenarios [9]:

1. Canister failure due to shear load (principally, a large earthquake in the vicinity of the repository).
2. Canister failure due to corrosion (under advective conditions in the bentonite buffer, assumed to be caused by buffer erosion).

These scenarios are highly unlikely to occur during the initial 1000 years after closing the repository, after which time period α-radiation dominates the radiation field [10]. The repository concept is currently under construction in Finland at the Olkiluoto reactor site. The application for the repository system consisting of the interim storage, encapsulation facility and final repository was approved by the Swedish government on January 27, 2022 [36].

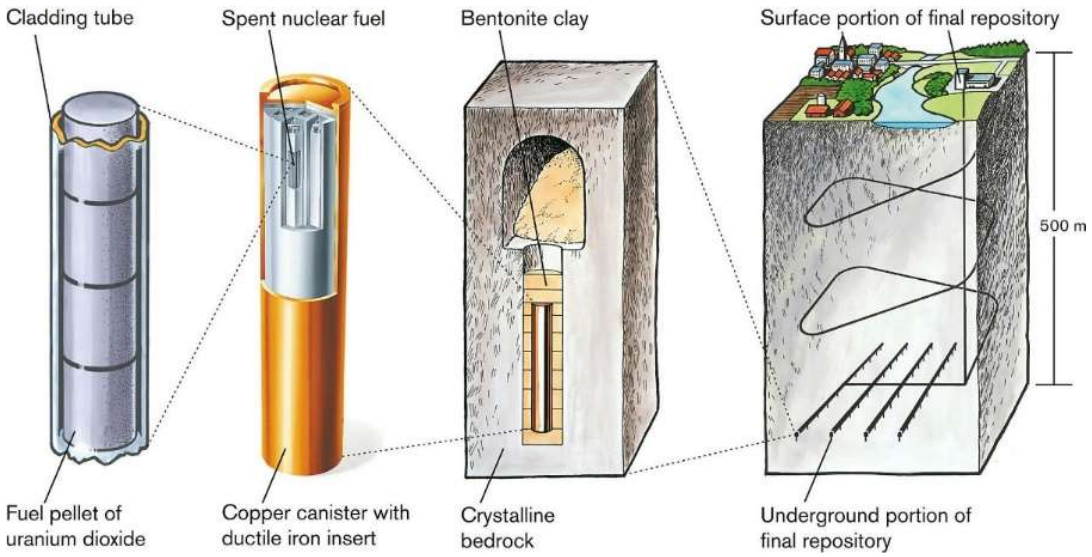

Figure 2.2. KBS-3 design with the fuel pellet, copper canister, bentonite clay and crystalline bedrock safety barriers. Courtesy of Swedish Nuclear Fuel and Waste Management Co., Illustrator: Jan Rojmar.

2.8. Radiolysis

In the process of radioactive decay, an unstable nucleus undergoes spontaneous transformation, emitting energy in the process. This process is categorized according to the type of radiation emitted. The main types of decay are α-, β-, and γ-decay, whereby α-, β-, and γ-particles are emitted. These particles consist, respectively, of a helium nucleus, an electron (emitted with an antineutrino) or positron (emitted with a neutrino), and high-energy electromagnetic radiation [37]. The γ-decay process occurs after α- and β-decay, which leaves the nucleus in an excited state, subsequently de-excited through the emission of a γ-particle. Other types of radioactive decay can occur, but are relatively rare and will not be considered in this work.

The ionizing radiation has sufficient energy to cause molecular dissociation in its interaction with matter through a process known as radiolysis. In the primary interaction with H_2O, which occurs in the 10^{-16} s timescale, an excited H_2O^* or ionized H_2O^+ is formed. The latter can react with water molecules to produce ·OH and H_3O^+ in the process. The excited H_2O^* splits into H· and ·OH, or H_2 and O· [38]. The full radiolysis scheme with corresponding timescales is shown in Figure 2.3.

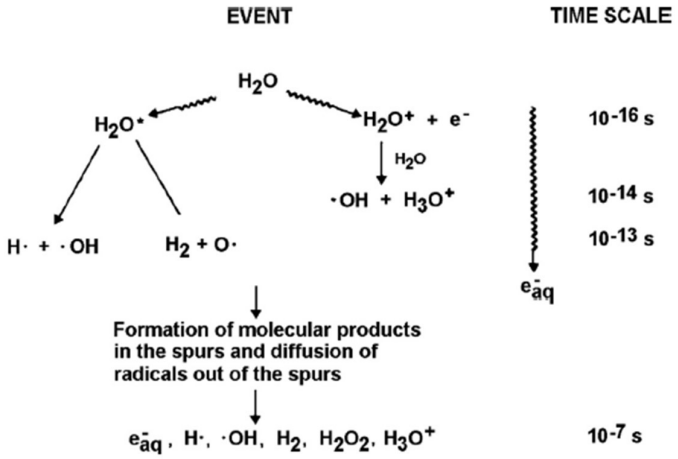

Figure 2.3. Radiolysis process with related timescales. Illustration from Choppin et al. [38].

The primary yields, or G-values, are the number of moles of a species produced or decomposed through ionization per unit energy emitted of the ionizing particle. For particles with high linear energy transfer (LET), meaning high dE/dx, a high density of radiolysis products is formed in the particle track. This promotes the formation of molecular species, as a greater degree of recombination of radicals into molecules can occur in the particle track. This is typical for α-particles, which have high G-values for molecular species relative to β-, and γ-radiation. G-values for α- and γ-radiation from the work of Pastina and LaVerne are shown in Table 2.1 [39]. The values in their work were obtained from the references [40-46], and were somewhat modified to improve the correspondence between their modelled and experimental concentrations.

Table 2.1. G-values (μmol·J^{-1}) for the water radiolysis products under α- and γ-radiolysis [39].

Species	$G(H_2O_2)$	$G(OH\cdot)$	$G(OH^-)$	$G(e_{aq}^-)$	$G(H_2)$	$G(H\cdot)$	$G(H^+)$	$G(HO_2)$
α - 5 MeV	0.104	0.036	0.003	0.016	0.124	0.010	0.019	0.010
γ-rays	0.073	0.280	0.052	0.269	0.047	0.068	0.321	0.002

2.9. Oxidative dissolution

$UO_{2.0}$ is a p-type semiconductor with low conductivity. In its tetravalent state, amorphous UO_2 will dissolve at a concentration of approximately 10^{-9} M at a typical groundwater pH of 7 – 9 [47]. Under these conditions, dissolution depends on efficient transport of uranium away from the surface through diffusion and advection. The UO_2 matrix must therefore be oxidized to cause significant dissolution. When stoichiometric $UO_{2.0}$ is oxidized, electron holes are created in the U5f sub-band, giving rise to a slight conductivity [11]. The higher conductivity of the oxidized UO_{2+x} can facilitate charge transfers, which increases its reactivity toward, e.g., O_2 and H_2O_2 [48]. H_2O_2 is the main oxidizing radiolysis species toward UO_2, with a relative impact of >99% [49]. The oxidative dissolution of UO_2 through reaction with H_2O_2 may be simply described through a two-electron transfer reaction from H_2O_2 to U(IV) as described in Eq.(4):

$$U(IV)O_2(s) + H_2O_2 \rightarrow U(VI)O_2^{2+}(aq) + 2OH^- \quad (4)$$

Before 2004-2005, the U(V) oxidation state was not considered relevant in the oxidation of UO_2 under environmental conditions due to the rapid disproportionation reaction of U(V) in solution [50]. However, UO_2 can be effectively stabilized as U(V) through reduction of U(VI) by Fe(II)-containing minerals [51], and during oxidative dissolution of SIMFUEL [52, 53] and UO_2 particles [54, 55]. The U(V) state was identified by Leinders et al. and Kvashnina et al. in their HERFD-XANES studies of the intermediate oxides U_4O_9, U_3O_7, and U_3O_8. These authors found that U_4O_9 and U_3O_7 are mixtures of U(IV) and U(V), and the first U(VI)-containing oxide is U_3O_8 [56, 57]. The oxidative dissolution threshold of $UO_{2.33}$, which is discussed in several works [28, 58], therefore corresponds to an oxide of U(IV) and U(V) whereby any further oxidation results in the formation of U(VI). The oxidation of U_3O_7 to U_3O_8 also involves an increase in unit cell volume by approximately 30%, as it transitions from a fluorite structure to a layered structure [59].

2.10. Anoxic Fe corrosion

In contact with groundwater, the massive iron inserts in the canisters will corrode extensively under the anoxic conditions present at repository depth, producing a significant amount of H_2 in the process [60]:

$$Fe(s) + H_2O \rightarrow Fe(OH)_2 + H_2(g) \quad (5)$$

$$3Fe(s) + 4H_2O \rightarrow Fe_3O_4(s) + 4H_2(g) \quad (6)$$

where Fe_3O_4 is magnetite, containing both Fe(II) and Fe(III) in a 1:2 ratio [61]. The H_2 produced initially dissolves, until pressures greater than the hydrostatic pressure of approximately 50 bar are reached (plus swell pressure from the bentonite) [62]. Following this, gas bubbles start forming [60].

Several studies have shown that both dissolved H_2 and Fe(II) suppress the corrosion rates of UO_2 fuels [63-65]. Dissolved U(VI) is also efficiently reduced to U(IV) and sorbed on the surface of metallic iron [66, 67]. Several studies have shown that dissolved U(VI) is efficiently reduced in contact with Fe(II)-containing minerals such as magnetite [61, 68] or green rust [67, 69]. In the water intrusion scenario, this can strongly influence the migration of dissolved UO_2 [60]. The system with a corroding metallic iron surface has a greater capacity for reduction than that of reduction by homogeneous Fe(II) in solution, or reaction with an anoxic iron corrosion product [64, 70]. In Cui and Spahiu's work, an initial concentration of 1 ppm U(VI) was decreased by almost three orders of magnitude in a 10 mM NaCl and 2 mM $NaHCO_3$ solution in contact with pure iron foil pieces, by the formation of carbonate green rust and UO_2 crystal precipitates [67].

2.11. The effect of H_2

H_2 is generated mainly through the anoxic corrosion reactions of Fe(s) (Eq.(5) – (6)), and, to a lesser extent, through radiolysis. At the relevant repository temperatures, H_2 is expected to be quite inert [71]. Although the reaction between H_2 and H_2O_2 is thermodynamically favorable, it is very slow [72]. However, the metallic ε-particles (Mo, Ru, Rh, Tc and Pd) can catalytically activate H_2, lending the fuel a very strong protective effect against oxidative dissolution. This

has been shown for both radioactively doped and non-radioactively doped UO_2-based fuels containing ε-particles [73]. A major effort has been made to study the effect of H_2 on the oxidative dissolution of SNF, with the finding that extremely low U concentrations are found under H_2 atmosphere, due to activation on the ε-particles [62, 74-76]. Under H_2 atmosphere, the reduction of dissolved U(VI) to U(IV) is observed in contact with Pd(s) (as a proxy for ε-particles) [77].

Activation on ε-particles is not the only pathway through which H_2 has a noticeable influence on both the oxidative dissolution of UO_2 and quantity of dissolved UO_2. However, the effect in the absence of ε-particles is less well-understood. A study by King et al., examined the corrosion potential of a UO_2 electrode under 50 bar H_2 and a γ-radiation field [78]. This study measured very low corrosion potentials, indicating a reduction of the UO_2 electrode. These potentials were even lower than under H_2 atmosphere without irradiation [78]. Sunder et al. studied UO_2 oxidation in an α-radiation field under 0.1 – 1 bar H_2 and 100 °C, and found that increasing α-activity caused greater reduction of the UO_2 pellet surfaces. The H_2 effect in the absence of ε-particles still requires activation on a UO_2 surface, as shown by Spahiu et al. [79], who found that dissolved uranyl-carbonato species were not homogeneously reduced by H_2.

2.12. Surface site reaction system

Besides causing oxidative dissolution of UO_2, H_2O_2 can also undergo catalytic decomposition on the UO_2 surface, resulting in H_2O and O_2 as products. The results of the works of Barreiro Fidalgo et al. [80] and Kumagai et al. [81] show that the dissolution of uranium through oxidative dissolution by H_2O_2 does not strictly follow first-order reaction kinetics. These authors measured dissolved uranium and H_2O_2 concentrations in solutions initially spiked with H_2O_2. Their results showed that the oxidative dissolution yield was a function of initial H_2O_2 concentration. H_2O_2 has been shown to form surface-adsorbed ·OH radicals on oxide surfaces, which could be the initiating step in the oxidation of the UO_2 surface [80-82]. The suggested reaction mechanism accounting for these observations is described in Table 2.2 [80, 81]:

Table 2.2. Surface site reaction system describing the surface adsorbed ·OH radical mediated UO_2 oxidation and decomposition reaction scheme.

$H_2O_2 + UO_2 - site \rightarrow 2\ OH \cdot (ads)$	ks1	(7)
$OH \cdot (ads) \rightarrow OH^- + U(V)O_2$	ks2	(8)
$H_2O_2 + OH \cdot (ads) \rightarrow HO_2 + H_2O + 0.5\ UO_2 - sites$	ks3	(9)
$HO_2 + HO_2 \rightarrow H_2O_2 + O_2$	kL58	(10)

The suppressing effect of H_2 on the oxidation of UO_2 by H_2O_2 in the absence of ε-particles could potentially be described as a reaction between the surface-adsorbed ·OH radical and H_2. The activation of H_2 on ε-particles could also be described in the context of the surface site reaction system. These effects are further described in Chapter 3.1.6.

2.13. Uranium speciation in groundwater

In typical granitic groundwaters, the carbonate concentrations are 2-10 mM [83], with CO_3^{2-}, HCO_3^-, and H_2CO_3 in equilibrium based on pK_{a1}=6.35 and pK_{a2}=10.33 [84]. Carbonate is a

fairly strong complexing agent of the UO_2^{2+} ion, forming the $UO_2(CO_3)_3^{4-}$ and $UO_2(CO_3)_2^{2-}$ complexes, which dominate in carbonate-rich conditions [85, 86]. The dissolution rate of oxidized UO_2 in O_2, or air-saturated perchlorate solution with pH 9.5, has been shown to increase significantly in the presence of 10 mM $NaHCO_3$, going from $1\text{-}9\cdot10^{-8}$ $g\cdot cm^{-2}\cdot d^{-1}$ to $4.8\cdot10^{-6}$ $g\cdot cm^{-2}\cdot d^{-1}$ [87]. Thus, carbonate can efficiently remove oxidized U(VI) from UO_2 surfaces, preventing corrosion product deposits on the surface which could prevent further oxidative dissolution [28]. Additionally, the chemical speciation of the dissolved uranyl ions can have a significant influence on its reduction by dissolved Fe(II). Free uranyl and its hydrolysis products are quickly reduced by dissolved Fe(II) and surface-bound Fe(II) [70, 88], while the process is significantly slower if the uranyl is in the uranyl-carbonato chemical form [70, 89]. In the presence of calcium, which is ubiquitous in groundwaters, the uranyl-carbonato complexes were quite recently found to form the calcium-uranyl-carbonato complexes $CaUO_2(CO_3)_3^{2-}$ and $Ca_2UO_2(CO_3)_3$ [90-94], through the reactions:

$$UO_2(CO_3)_3^{4-} + Ca^{2}+ \rightleftharpoons CaUO_2(CO_3)_3^{2-}, \log k = 5.2 \pm 0.2 \quad (11)$$

$$UO_2(CO_3)_3^{4-} + 2Ca^{2}+ \rightleftharpoons Ca_2UO_2(CO_3)_3, \log k = 9.0 \pm 0.4 \quad (12)$$

These complexes have been shown to kinetically inhibit the homogeneous reduction of uranyl by Fe(II)(aq) and slow down the heterogeneous reduction [89]. This effect has also been seen in the case of microbial reduction of U(VI), which is likely due to thermodynamic or steric factors, or a combination of the two [95, 96]. The calcium-uranyl-carbonato complexes also limit the sorption of U(VI) [97, 98].

3. Theory

3.1. Modelling

In order to theoretically estimate the dissolution rates of UO_2-based materials, the dose rates stemming from the strong α-activity and the resulting H_2O_2 production rates have to be estimated. These production rates were combined with mass transfer as well as chemical kinetics to give theoretical estimations which can be compared to experimental results.

3.1.1. Alpha dose rate

To model the α-particles emitted in a UO_2-based material, an isotropic distribution of emission paths must be implemented. This is achieved by randomizing a random emission coordinate in the UO_2 material, and calculating a particle path using "Archimedes theorem" [99]. The method entails mapping particle coordinates on a $z0$ = [-1,1] by θ = [0,2π] cylinder for each particle and calculating the inverse axial projection on the unit sphere, scaled by the maximum range of an α-particle in the UO_2 matrix, δ_{UO2}:

$$x = \sqrt{1 - z0^2} \cdot \cos(\theta) \cdot \delta_{UO_2} \tag{13}$$

$$y = \sqrt{1 - z0^2} \cdot \sin(\theta) \cdot \delta_{UO_2} \tag{14}$$

$$z = z0 \cdot \delta_{UO_2} \tag{15}$$

The distribution of $3 \cdot 10^3$ particles generated on the surface of a unit sphere is shown in Figure 3.1. The particle paths also need to be associated with a random emission coordinate in the UO_2 material. The planar geometry allows for generalization of the emission coordinate with respect to the x-y plane, because that the surface is perpendicular to the z-axis. Therefore, only the z-coordinate needs to be considered when randomizing the emission coordinate.

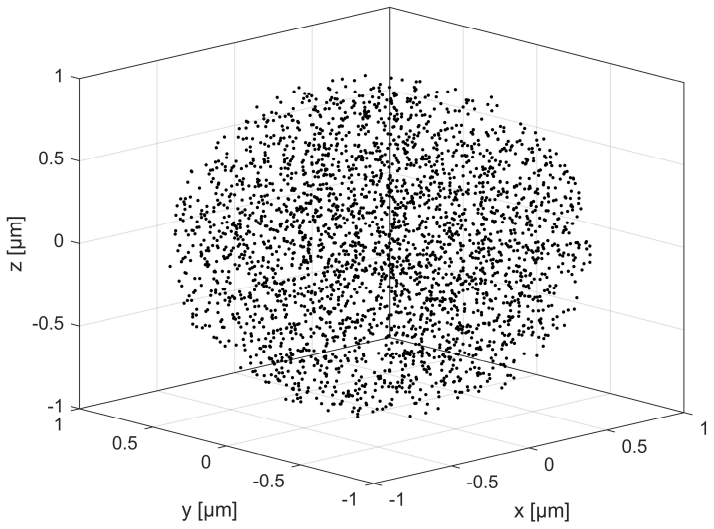

Figure 3.1. Distribution of $3 \cdot 10^3$ particles on the surface of a unit sphere using "Archimedes theorem" [99].

The probability of an α-particle emitted in the outermost layer with thickness δ_{UO_2} of a planar UO_2 material to escape can be calculated as [100]:

$$P(d) = \left(\delta_{UO_2} - d\right)/2\delta_{UO_2} \tag{16}$$

where d is the emission depth. The probability is a linear function equal to 0.5 and 0 between $d = 0$ and δ_{UO_2} respectively, giving an average escape probability of 25%. The experimentally studied pellets can be estimated as planar with virtually no error. (Further details may be found in Paper IV.) The total α-activity of a UO_2-based material can be calculated as:

$$A_{tot} = S \cdot V \cdot \rho_{UO_2} \tag{17}$$

where S is the mass-specific α-activity of the material, V is the volume, and ρ_{UO_2} is the density of the material. The emission time, (the time it takes for the chosen number of α-particles to be emitted) can be directly calculated from the total activity of the modelled fuel. Mass stopping powers ($MeV \cdot cm^2 \cdot g^{-1}$) were obtained from ASTAR for UO_2 and H_2O [101], and were converted into linear stopping powers ($MeV \cdot cm^{-1}$) using the mass density. The α-particles are attenuated in steps from their emission point, with an arbitrary step size. The particles lose energy equal to the step size multiplied by the linear energy stopping power in each step. Due to the energy dependence of the stopping power, the stopping power has to be updated in each step as the energy of the α-particles decreases. Storing the energy absorbed in the UO_2 and H_2O layers for each particle gives a dose rate profile in both UO_2 and H_2O. Based on the energy of particles crossing the UO_2-H_2O interface, the average escape energy and α-particle escape fraction can be calculated. Comparing the escape fraction resulting from the isotropic emission model with the theoretical value (25% for planar surfaces) allows for verification of the particle emission distribution and resolution, in terms of step sizes, layer sizes, and number of particles emitted. More details may be found in Paper IV.

3.1.2. Diffusion

Diffusion is the process through which particles or molecules accumulate or deplete at a rate proportional to the curvature (or second derivative) of the concentration and diffusivity. The process is described through Fick's second law of diffusion:

$$\frac{\partial c}{\partial t} = D\frac{\partial^2 c}{\partial x^2} \tag{18}$$

The equation can be solved by discretizing and using a backward difference approximation of the concentration time derivative and a second order central difference approximation of the curvature. See Paper V for further details.

3.1.3. Chemical kinetics model

A combined radiolysis and carbonate species reaction system was implemented in MATLAB 2019a, combined with the α-dose rate calculation model. The kinetic rate constants for the radiolysis species reactions were obtained from references [102-106]. The rate constants for carbonate species reacting with the radiolysis products were obtained from the work of Cai et

al. [106]. A second order rate constant for the reaction between H_2O_2 and UO_2 of $7.56 \cdot 10^{-8}$ $m \cdot s^{-1}$ in solution with 1-100 mM HCO_3^- was obtained from the work of Hossain et al. [107]. The full reaction rate table is shown in Appendix B (Table S.1). The reaction system was solved using the MATLAB ode15s function, which is highly suitable for the stiff system.

3.1.4. Steady-state approximation

The H_2O_2 steady-state concentration in a system where H_2O_2 consumption can be approximated to only occur through oxidative dissolution of the UO_2 surface can be expressed as [76, 108]:

$$[H_2O_2]_{ss} = \frac{r_{H_2O_2} \cdot \delta_{max}}{k_{H_2O_2}} \tag{19}$$

where r_{H2O2} is the production rate of H_2O_2 in the irradiated volume which is defined by the maximum range of an α-particle in H_2O, δ_{max}, and k_{H2O2} is the rate of UO_2 oxidation by H_2O_2. Under H_2 atmosphere, the steady-state concentration can be calculated using the equation from the work of Trummer and Jonsson [109]:

$$\frac{[H_2O_2]_{ss,H_2}}{[H_2O_2]_{ss}} = \frac{[H_2O_2]_{ss,H_2} \cdot k_{H_2O_2}}{r_{H_2O_2} \cdot \delta_{max}} = 0.026 \frac{1}{\sqrt{D}} + 0.005 \tag{20}$$

However, this equation is only applicable above a critical H_2 pressure, which depends on the dose rate and HCO_3^- concentration [109].

3.1.5. Surface site reaction system

The surface site reaction system described by reactions Eq.(7)–(10) in Table 2.2 can be defined using a UO_2 surface site density of $2.1 \cdot 10^{-4}$ $mol \cdot m^{-2}$, determined by Hossain et al. [107]. A reaction to describe the dissolution of U(VI) was assigned in the model as a reaction between U(V) formed on the surface:

$$U(V)O_2 + U(V)O_2 \rightarrow U(VI)O_2(aq) + UO_2 - site \qquad \text{ks4} \tag{21}$$

with a rate constant ks4. The rate constants ks1 – ks4 can be fitted to the experimental data series from the work of Barreiro Fidalgo et al. in which UO_2 dissolution under additions of H_2O_2 was studied in a 10 mM $NaHCO_3$ solution with 0.2, 0.5, 1.0 and 2.0 mM initial H_2O_2 concentrations [80]. The fit can be made through minimizing the residual sum of squares between the experimental data and the modelled reaction system, through iterations over the rate constants, ks1, ks2, ks3 (described by Eq.(7)–(9) in Table 2.2) and ks4. (The rate constant labelled kL58 in Eq.(10) Table 2.2 has been previously determined and is included in the full kinetic reaction scheme (Appendix B, Table S.1).)

3.1.6. H_2 surface site reaction system

The effect of H_2 can be described using an extended version of the surface site reaction system. In order to be able to describe reduction of U(VI) the UO_2 surface, the oxidation to U(VI) cannot directly give dissolved U(VI) as described in reaction (21). Therefore, in the extended surface site reaction system, the dissolution of $U(VI)O_2(s)$ by HCO_3^- is described by:

$$HCO_3^- + U(VI)O_2(s) \rightarrow UO_2CO_3(aq) + H^+ + UO_2 - site \qquad \text{ks5} \qquad (22)$$

with a reaction rate constant, ks5. This reaction is experimentally found to be diffusion controlled, and is therefore described by a value of 10^3 $M^{-1}\cdot s^{-1}$ (which corresponds to diffusion controlled in our system). In the absence of ε-particles, the inhibiting effect of H_2 could potentially be described as a reaction between the surface-adsorbed ·OH radical and H_2 shown in Eq.(23) with a rate constant ks6. In order to describe the reaction between H_2 and ε-particles in the model, the reducing species labelled "red" is formed, which reacts very quickly with the oxidized U(VI) to form U(IV). Similarly, ε-particles have been shown to catalyze the oxidation of UO_2 by H_2O_2 [110]. In the context of the modelled reaction system, this is described as a reaction between H_2O_2 and ε-particles, forming the species "ox", which reacts quickly with U(IV) to form U(VI). The reactions describing this are shown in Table 3.1, with rate constants ks6 – ks10. More details may be found in Paper VIII.

Table 3.1. Extended surface site reaction system, describing the effect of H_2 and catalyzed oxidation of UO_2 by H_2O_2.

$OH\cdot(ads) + H_2 \rightarrow H\cdot + 0.5\,UO_2 - sites + H_2O$	ks6	(23)
$\varepsilon - site + H_2 \rightarrow red$	ks7	(24)
$red + U(VI)O_2(s) \rightarrow UO_2 - site + 2H^+ + \varepsilon - site$	ks8	(25)
$H_2O_2 + \varepsilon - site \rightarrow ox$	ks9	(26)
$ox + UO_2 - site \rightarrow UO_2^{2+}(s) + \varepsilon - site + 2OH^-$	ks10	(27)

The rate of oxidation of UO_2 pellets containing Pd (to represent ε-particles) by H_2O_2 was shown by Trummer et al. to occur approximately 100 times faster [111] compared to the oxidation of pure UO_2 [107] ($(6.92\pm1.52)\cdot10^{-6}$ $m\cdot s^{-1}$ compared to $7.56\cdot10^{-8}$ $m\cdot s^{-1}$). This can be described by assigning a value to the rate constant ks7 (Eq.(24)) of 100 times that of reaction ks1 (Eq. (7)).

3.1.7. Integrated radiolysis, kinetics, and diffusion model

The radiolytic production, diffusion, and kinetic models were coupled in an iterative procedure, using the scheme in Figure 3.2. The initially present species, such as HCO_3^-, react with the radiolytically produced species in the kinetics step, after which the species diffuse between layers in the diffusion step. The diffused system is then used as in-data for the next time step in the kinetic model. The time steps for the kinetic and diffusion steps are equal, with 50 computational steps within each one. The system may be divided into an arbitrary number of time steps and spatial steps irradiated by an arbitrarily strong radiation source.

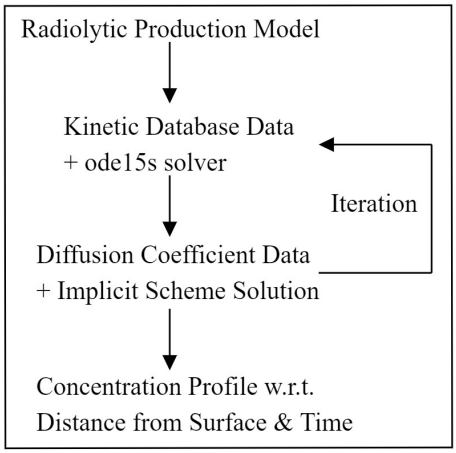

Figure 3.2. Coupled radiolysis, kinetic- and diffusion model scheme

3.2. X-ray photoelectron spectroscopy

X-ray photoelectron spectroscopy (XPS) utilizes the photoelectric effect by firing ~1 keV X-rays at a surface under a vacuum (10^{-8} – 10^{-9} mbar). Electron binding energies are determined by measuring the ejected atomic core electrons [112]. These energies depend on the chemical state of the element. The U(IV) and U(VI) $U4f_{7/2}$ peak positions have been determined in many works as ~380 and ~382 eV respectively [51, 113-115]. To determine the oxidation state, the $U4f_{7/2}$ peak may therefore be analyzed based on the properties of the U(IV), U(V) and U(VI) chemical states (Table 3.2).

Table 3.2. Characteristic features of the U(IV), U(V), U(VI) states and associated satellite positions.

Uranium oxidation State	Position (eV) [113, 116]	FWHM (eV) [52]	Satellite shift (eV) [52]	Satellite shift (eV) [117]
U(IV)	380.0±0.2	1.65	7.0	6.7
U(V)	380.8±0.2	1.65	8.5	9.0
U(VI)	382.0±0.3	1.65	4.2, 10.0	4.0, 10.0

4. Materials

Fuel pellets, chemicals and solutions are presented in this chapter followed by descriptions of the instruments and equipment used in the experiments.

4.1. Pellets and radiation sources

4.1.1. UO_2 pellets

Pellets with a natural uranium composition of 99.3% U-238 and 0.7% U-235 as well as slightly enriched pellets composed of 98.0% U-238 and 2.0% U-235 were used in the experiments. The specific α-activity of the slightly enriched pellets was $2.64 \cdot 10^4$ $Bq \cdot g^{-1}$.

4.1.2. MOX pellets

MOX pellets with 10 and 24 wt.% Pu-doping were used in the experiments. The 24 wt.% Pu-doped MOX pellet was produced in 2006 using the MIMAS (MIcronized MASter blend) process at Belgonucleaire in Belgium. The pellet grain size was roughly 7 µm at 93% theoretical density and specific α-activity of 4.96 $Gbq \cdot g^{-1}$. The americium content was determined as 77.8 $\mu g \cdot g^{-1}$ using gamma spectrometry. A thermal conductivity technique was used to measure the carbon content as 37 wt. ppm. The pellet had a mass of 1.302 g, with a half-cylinder geometry and geometrical surface area of 1.60 cm^2 (without roughness factor). The composition and dimensions of the 24 wt.% Pu-doped MOX pellet appear in Table 4.1. Further details about the characterization and manufacturing process may be found in Paper I.

Table 4.1. Calculated composition and dimensions of the 24 wt.% Pu-doped MOX piece.

Oxide composition			Pu/Am isotopic composition		Dimensions	
UO_2	PuO_2	AmO_2	**June 2019**		Diameter	Height
75.11 wt.%	23.61 wt.%	1.29 wt.%	^{238}Pu	2.06%	8.73 mm	4.43 mm
			^{239}Pu	55.09%		
			^{240}Pu	25.91%		
			^{241}Pu	4.82%		
			^{242}Pu	6.96%		
			^{241}Am	5.17%		

Two 10 wt.% Pu-doped MOX pellets (produced through the MIMAS process in the MELOX factory in France) were also used in the experiments. These were manufactured to a 95% theoretical density and specific activity of 1.72 $GBq \cdot g^{-1}$. The pellets had a heterogeneous microstructure, with three separate phases with varying degrees of Pu-concentration. Additional characterization of the 10 wt.% Pu-doped pellets may be found in Odorowski et al, where MOX pellets were produced with the same microstructure using the same process [118]. The composition and dimensions of the 10 wt.% Pu-doped MOX pellets are shown in Table 4.2.

Table 4.2. Composition and dimensions of the 10 wt.% Pu-doped MOX pieces.

Oxide composition			Pu/Am isotopic composition		Dimensions	
UO_2	PuO_2	AmO_2	**June 2019**		Diameter	Height
89.76 wt.%	10.23 wt.%	0.01 wt.%	^{238}Pu	1.32%		
			^{239}Pu	64.37%	8.08 mm	4.22 mm
			^{240}Pu	26.60%	8.08 mm	3.27 mm
			^{241}Pu	2.54%		
			^{242}Pu	5.05%		
			^{241}Am	0.12%		

4.1.3. SIMFUEL

The SIMFUEL pellet used in this work was manufactured by ACEL Research, Chalk River Laboratories. The pellet consisted of UO_2 with Sr, Y, Zr, Mo, Ru, Rh, Pd, Ba, La, Ce and Nd doping analogous to a burnup level of 50 $MWd \cdot kg^{-1}$. The pellet had distinct metallic ε-particles phases on its surface. Additional information on the pellet characterization may be found in [119].

4.1.4. Am-241 sources

Eckert & Ziegler Am-241 sources with α-activities 1.85 and 3.30 MBq were used. The AmO_2 powder was covered by a 2 μm layer of pure gold to prevent leakage. The inner dimensions of the AmO_2-powder compartment were Ø 15.5 x 0.4 mm which was contained in a SS 304 frame exposing a cross-section of Ø 11.5 mm.

4.2. Chemicals and solutions

All solutions throughout this work were diluted using MQ water with a resistivity of 18.2 MΩ·cm. 30 wt.% H_2O_2 (Sigma-Aldrich) was used to spike the solutions in the SIMFUEL leaching experiments. O_2-traps with siderite ($FeCO_3$) were produced by mixing $FeSO_4 \cdot 7H_2O$, ascorbic acid and $(NH_4)_2CO_3$ in an autoclave at a molar ratio of 1:1:3, reacted in a 50 mL MQ solution at 140 °C for 1.5h. This process is described in detail in Nassar et al. [120], yielding roughly 1 g of product.

4.2.1. Iron foils

Iron foils (≥99.99% metal basis Thermo Scientific Alfa Aesar) of approximately 0.1 mm thickness and ~1.56 cm^2 area weighing 0.125 g were used in the uranyl + synthetic groundwater experiments. Prior to the experiments, the iron foils were polished using 1200 grit (FEPA-P) SiC sandpaper in the glove box atmosphere to remove any pre-oxidized layer.

4.2.2. Groundwaters

The synthetic groundwaters were prepared using ≥99.0% ACS reagent-grade chemicals (Sigma-Aldrich and Merck). Two groundwaters measured at the Forsmark site (labelled 01D and 02A) were synthesized [121]. The additions of Mn and Fe was performed in the inert glove box atmosphere directly prior to the experiments to minimize the oxidation of these elements. Two other simplified groundwater compositions were also studied. The "10-2" solution

consists of 10 mM NaCl with 2 mM $NaHCO_3$, prepared from 99.99% Merck and 99.7-100.3% Sigma-Aldrich respectively. A "10-2-Ca" groundwater using 10 mM NaCl with 0.546 mM $CaCO_3$ (≥99.0% Sigma-Aldrich), and 2 mM total carbonate concentration was prepared to study the influence of calcium. The groundwater compositions are shown in Table 4.3.

Table 4.3. Compositions of synthetic groundwaters. Concentrations in units mmol·L^{-1}.

Ground-water	$[Na^+]$	$[K^+]$	$[Ca^{2+}]$	$[Mg^{2+}]$	$[HCO_3^-]$	$[Cl^-]$	$[SO_4^{2-}]$	$[Br^-]$	$[F^-]$	[Si]	$[Fe^{2+}]$	$[Mn^{2+}]$	$[Sr^{2+}]$	pH
01D	77.02	0.187	45.91	0.448	0.280	168.56	0.324	0.581	0.061	0.152	0.014	0.0016	0.237	8.40
02A	96.57	0.931	22.21	10.04	2.065	148.91	5.275	0.304	0.077	0.216	0.041	0.0377	0.099	7.19
10-2	12.00	0	0	0	2.000	10.00	0	0	0	0	0	0	0	8.34
10-2-Ca	10.47	0	0.526	0	2.000	9.00	0	0	0	0	0	0	0	8.34

In the iron foil experiments, a stock solution prepared with 10 ppm U(VI) was diluted with the synthetic groundwaters, resulting in an initial volume of 20 mL with U(VI) concentration equal to 1 ppm or $4.2 \cdot 10^{-6}$ M equivalently.

4.3. Instruments

4.3.1. XPS

XPS measurements were conducted using a PHI 5000 VersaProbe III. The instrument was equipped with an Al K-α X-ray source with energy 1486.6 eV [122]. Calibration utilized the $Au4f_{7/2}$, $Ag3d_{5/2}$, and $Cu2p_{3/2}$ energies of 83.96±0.05, 368.21±0.05 and 932.63±0.05 eV respectively through sputtering metallic pieces [123]. A Shirley background with 70-30% Gaussian-Lorentzian fit was used in the $U4f_{7/2}$ peak deconvolution process. A transfer vessel (model 04-111) tailor-made to fit the sample inlet of the XPS instrument was used to transfer samples from the inert glove box atmosphere, without O_2 contaminating the sample during transportation. The measurement uncertainties were considered to be very small and were not considered in the analysis of the data.

4.3.2 Mass spectrometry

Solution concentrations were determined by inductively coupled plasma mass spectrometry (ICP-MS), using a Thermo Scientific iCAP Q instrument. The samples were diluted with 0.5 M HNO_3 (Suprapur, Merck) containing 10 ppm Th-232 internal standard (CPAchem). External calibration series of the analyzed elements in the 0 – 50 ppb concentration range were prepared from 10 ppm stock solutions (CPAchem). When measuring iron and calcium, kinetic energy discrimination was used to eliminate polyatomic ion interferences [124]. Measurement uncertainties were found to be quite insignificant (<2% relative uncertainty) for any concentrations significantly above 0.1 ppb due to the high resolution of the instrument. The uncertainties were therefore not plotted in the concentration series, since they overlap considerably with the datapoints.

4.3.3. UV-VIS spectroscopy

H_2O_2-concentrations were measured using the Ghormley tri-iodide method with a Shimadzu UV-1800 UV-VIS instrument. This method is based on the oxidation of iodide by H_2O_2 in the presence of an ammonium molybdate tetrahydrate catalyst (≥99.0%, Sigma-Aldrich) [125-127]. 2 mL samples were mixed with 100 µL 1M KI (≥99.5% Sigma-Aldrich) and 100 µL

catalyst in acetate buffer solution (pH 4.65 Sigma-Aldrich). Calibrations were carried out in the 0.01 – 0.1 mM H_2O_2 (Sigma-Aldrich) concentration range.

4.3.4. Autoclaves

Parr Instruments Co. stainless-steel autoclaves of 450 mL internal volume were used in the leaching experiments. Original NPT (national pipe thread) lid connections were replaced with VCR (vacuum coupling radiation) ones to ensure more leak-tight connections under H_2 atmosphere. Graphite gaskets covered in a thin layer of grease were placed in the lid groove. These deform as the lid screws are tightened, forming a gas-tight seal. T316 stainless steel or PEEK dip tubes were used in the sampling process, utilizing the overpressures in the autoclaves.

4.3.5. X-ray diffraction spectroscopy

X-ray diffraction (XRD) measurements were made using a BRUKER D2 PHASER instrument with copper K-α lines with λ_1=1.54045 Å and λ_2=1.54439 Å. The instrument was kept in a glove box with a low O_2 atmosphere to ensure no surface oxidation of the samples occurred during the measurements.

4.3.6. Glove box

Several experiments were conducted in a glove box (Inert Technology) with an Ar atmosphere at a very low partial pressure of O_2 (approximately 0.1 ppm) under normal operating conditions. The glove box is equipped with a catalytic bed which efficiently removes O_2 from the glove box atmosphere.

4.3.7. Furnace

The MOX pellets were annealed prior to the leaching experiments in a 1000-2560-FP20 High Temperature graphite furnace (from Thermal Technology), using 5% H_2 in N_2 or 5% H_2 in Ar at 1200 °C for 5h. A 1h heating and cooling period was used in both cases. The furnace was located in a glove box with a N_2 atmosphere to prevent any pellet oxidation during cooling.

4.3.8. HDO analysis

The H/D isotope analysis was conducted using a Liquid Water Isotope Analyzer (Los Gatos Research, Inc.) at the UC Davis Stable Isotope Facility. Results are reported relative to Standard Mean Ocean Water (SMOW) with an isotopic ratio of $155.76 \cdot 10^{-6}$.

4.3.9. SEM/EDS

A Phenom tabletop scanning electron microscope (SEM) with energy-dispersive spectroscopy (EDS) was used to analyze the iron foil surfaces after contact with uranyl and synthetic groundwater solutions.

5. Experimental

The experimental work in this thesis is based on four experimental setups: external irradiation of UO_2 using Am-241 sources, uranyl in contact with iron foils, SIMFUEL leaching experiments in solution spiked with H_2O_2 and the leaching of highly Pu-doped MOX-pellets. The setups, conditions, and pre-treatment of materials used in the experiments are described in this chapter. Duplicate experiments were in general conducted, which were analyzed and interpreted separately. Uncertainties from the duplicate experiments could not be directly calculated, but are discussed based on the differences in the results.

5.1. External irradiation of UO_2 (Paper III)

The surfaces of the 0.72% and 1.96% U-235 enriched UO_2 pellets were polished inside the glovebox using 600 and 2400 grit (FEPA-P) SiC paper prior to the experiments. This removed any pre-oxidized layer and exposed a fresh surface. The pellets were then washed in four steps using 80 mL solutions with $NaHCO_3$ concentrations of 50, 10, 10 and 0 mM for 24h in each washing step.

The 1.85 and 3.30 MBq Am-241 sources were used to externally irradiate the solution close to the UO_2 pellet surfaces, under 10 bar H_2 and Ar atmospheres. The sources were separated from the UO_2 pellet surfaces by placing 30 µm diameter Pyrex threads on top of the gold-plated source. The experimental setup is shown in Figure 5.1. This setup is analogous to the one in the work of Sunder et al., where the radiolytic oxidation of UO_2 pellets exposed to Am-241 sources with activities of up to 14.8 MBq was studied [58]. The Am-241 sources and UO_2 pellets were placed in beakers inside autoclaves which, in turn, were kept in the glove box to ensure that the conditions were as anoxic as possible. Experiments were conducted in both 0 mM and 10 mM $NaHCO_3$ solutions. The 0 mM $NaHCO_3$ experiments retained the oxidized uranium on the surface of the pellets, which allowed for oxidation to be measured using XPS. The presence of HCO_3^- in the 10 mM $NaHCO_3$ experiments led to dissolution of oxidized uranium, allowing it to be measured in solution using ICP-MS.

The 10 mM $NaHCO_3$ experiments were conducted under H_2 and Ar atmospheres in ~150 mL solution using the 3.30 MBq source for ~45 days. Samples of ~7.5 mL were taken roughly every 6 days and were measured using ICP-MS. The 0 mM $NaHCO_3$ experiments were conducted in ~45 mL MQ solution using both the 1.85 and 3.30 MBq sources under 10 bar H_2 and Ar atmospheres, for durations of 11 days. An additional 45-day experiment in ~150 mL 0 mM $NaHCO_3$ solution was conducted to allow for comparison between the 0 mM and 10 mM $NaHCO_3$ conditions. At the end of the 0 mM $NaHCO_3$ experiments, samples were taken for ICP-MS measurement. Samples were ultra-centrifugated at 23377 rpm for 20 minutes under temperature-controlled conditions of 25 °C, to remove any particles and colloids. Both ultracentrifuged and non-centrifuged samples were measured using ICP-MS.

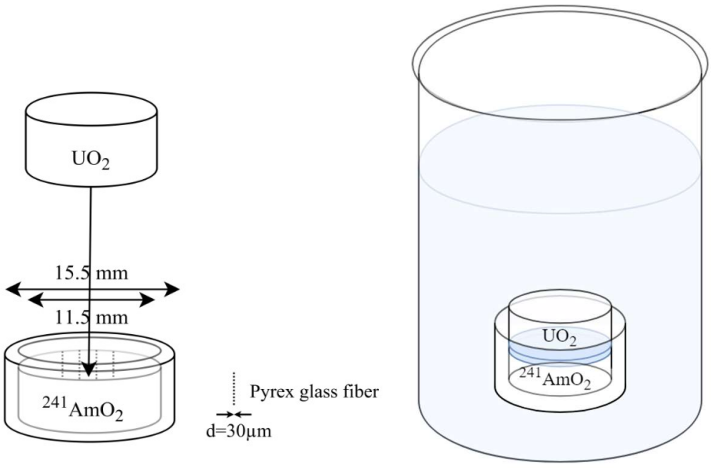

Figure 5.1. UO_2 pellet separated by 30 µm from the Am-241 source by placing Pyrex glass fibres in-between.

5.2. Uranyl in contact with corroding iron foils (Paper VII)

A uranyl stock solution was mixed with synthetic groundwaters and placed in contact with iron foils in plastic vials for ~1000 h. The experiments were continuously flushed with a CO_2 + Ar gas mixture and carried out batchwise in a ~2L glass reaction vessel, to ensure that the atmosphere was shared between all samples in the batch. To further ensure anoxic conditions, the reaction vessel was kept in the glove box throughout the experiment. To prevent evaporation, a gas washing bottle was used to saturate the gas mixture before it entered the reaction vessel. O_2-traps were used to remove traces of O_2 leaking into the glove box via gloves, antechambers or gas connections, as well as traces of O_2 from the glove box Ar gas supply and Ar + CO_2 gas mixtures. The experimental setup can be seen in Figure 5.2. The temperature in the glove box was close to 293.15K for all experiments. The iron and manganese additions to the synthetic groundwaters (Table 4.3) were carried out in the glove box directly prior to the experiments, to minimize oxidation of these species.

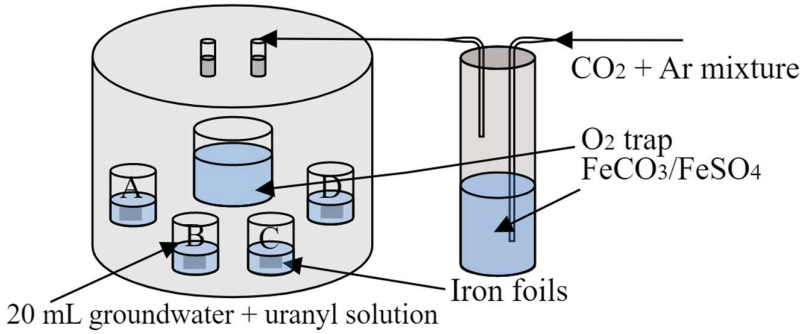

Figure 5.2. Experimental setup for the iron foil experiments, with reaction vessel and gas washing bottle containing O_2-traps and groundwater + uranyl solutions. The setup was kept in the inert glovebox atmosphere throughout the experiment.

The groundwaters and atmospheres present in the four batches with samples A-P are shown in Table 5.1. In the experiment batches containing samples A-D and I-L, the O_2-trap solution in both the reaction vessel and gas washing bottle consisted of 50 mL MQ with 2g $FeSO_4$ and 2.5g $CaCO_3$. In experiment batches E-H and M-P, a 50 mL solution saturated with $FeCO_3$ + 2.5g $CaCO_3$ was used instead.

Table 5.1. Groundwater and atmosphere compositions with their corresponding sample label.

Groundwater	Sample
01D	A, E, I, M
02A	B, F, J, N
10-2	C, G, K, O
10-2-Ca	D, H, L, P
Atmosphere	**Sample**
3000 ppm CO_2 in Ar	A, B, C, D
400 ppm CO_2 in Ar	E, F, G, H, I, J, K, L, M, N, O, P

Samples of ~1 mL were taken approximately every 24 hours during the initial stages, and once every ~100 hours during the later stages. The samples were analyzed using ICP-MS. The iron foil pieces were removed from the solutions at the end of the experiments and analyzed using XPS and SEM/EDS.

5.3. SIMFUEL leaching experiment (Paper II)

The SIMFUEL leaching experiments were conducted in an autoclave, with a 100 mL 10 mM $NaHCO_3$ solution. Prior to the experiments, the SIMFUEL pellet was washed in three 30 min steps in 10 mM $NaHCO_3$ solution under Ar bubbling to remove pre-oxidized uranium on the surface of the pellet. The autoclave solution was bubbled for at least 30 minutes to remove dissolved O_2 before the pellet introduced to the solution. Approximately 25 µL of concentrated H_2O_2 stock was added to the solution, giving an initial concentration of 2.5 mM. The autoclave was pressurized to 10 bar of D_2. Samples of 7 – 7.5 mL were taken at roughly 15 h intervals. The H/D isotope ratios and amounts of dissolved uranium in the samples were measured using a Liquid Water Isotope Analyzer and ICP-MS respectively.

5.4. MOX leaching experiments (Papers I and VI)

Glass beaker inserts were put into the autoclaves so that the autoclave surface would not come in contact with the solution during leaching of the MOX pellets. These glass beakers initially contained 150 – 250 mL of 10 mM NaCl + 2 mM $NaHCO_3$ solution, which was purged using Ar or D_2 gases for at least 30 minutes to remove dissolved O_2. The freshly annealed MOX pellet was then put into the solution, after which the autoclaves were closed using a graphite gasket into the lid groove, which deformed as the autoclave bolts were tightened. The autoclaves were placed in a vise while tightening the screws using a torque wrench set to 10 Nm. This ensured even pressure on all bolts and an even deformation of the graphite gasket. During bolt tightening, the atmosphere gas was bubbled through the dip tube connection to ensure no O_2 was dissolved from air in-leakage. After the bolts were properly tightened, the autoclaves were pressurized to ~10 bar and then flushed down to ~3 bar. This was repeated approximately 15 times to remove any O_2 in the gas connection lines. The initial pressure was then set to 10 bar. Roughly 10 samples of ~7.5 mL were taken throughout the 60 – 400-day experiments. Samples were ultra-centrifugated at 23377 rpm for 20 minutes under temperature-controlled conditions at 25 °C to remove any particles and colloids. Both ultracentrifuged and non-centrifuged samples were measured using ICP-MS. Samples sent for H/D analysis were distilled to remove any radioactivity.

6. Results and Discussion

In this section, results of the α-dose rate and radiolytic production modelling are presented, followed by the results of the experiments described in Chapter 5. Lastly, the experimental dissolution rates and H_2O_2 production rates are compared to the combined radiolysis, diffusion and kinetic model.

6.1. Alpha dose rate modelling (Paper IV)

The radiolytic production and α-dose rate of the 24 wt.% Pu-doped MOX pellet was modelled using the stepwise isotropic emission model (described in Chapter 3.1). The UO_2 and H_2O sections were divided into layers of thickness 0.1 µm. Both β- and γ-dose rates were shown to be negligible for MOX fuels, as modelled in Paper I, and in the works of Kerleguer et al., and Odorowski et al. [118, 128]. The energy absorbed in the H_2O section was used to calculate the radiolysis product generation in each water layer, using the G-values from the work of Pastina and LaVerne (Table 2.1) [39]. The dose rate profile at the H_2O-UO_2 interface is shown with the H_2O_2 production rate in Figure 6.1. The average dose rate in the irradiated water volume was 7.26 $kGy \cdot h^{-1}$ with a specific H_2O_2 production rate equal to $2.03 \cdot 10^{-7}$ $M \cdot s^{-1}$. In Paper I, the dose rate was calculated using the Sunder method, with a mass stopping-power ratio between H_2O and UO_2 of 1.39. This yielded an incorrect and significantly higher dose rate of ~23 $kGy \cdot h^{-1}$, as discussed in detail in Hansson et al. [129].

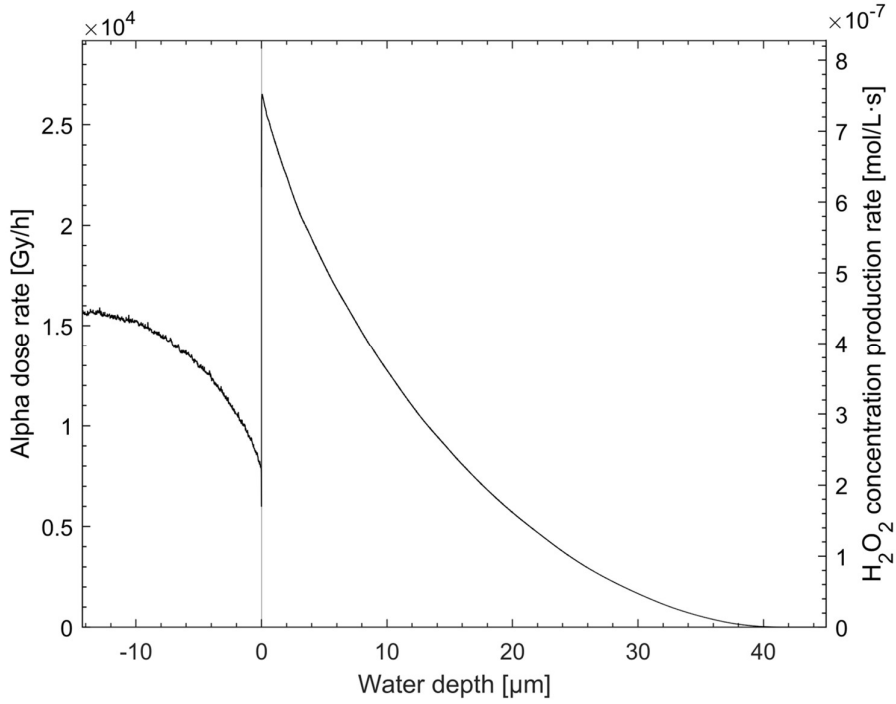

Figure 6.1. UO_2-H_2O interface dose rate for the 24 wt.% Pu-doped MOX pellet with α-particle energy of 5.44 MeV, specific α-activity of 4.96 $GBq \cdot g^{1}$ and a mass density of 10.31 $g \cdot cm^{-3}$.

6.2. Radiolytic production from MOX (Paper VI)

The α-dose rates and H_2O_2 production rates of the 10 wt.% Pu-doped MOX pellets were also modelled. The resulting H_2O_2 production rates were $1.24 \cdot 10^{-7}$ mol·d^{-1}, $3.67 \cdot 10^{-8}$ mol·d^{-1}, and $3.46 \cdot 10^{-8}$ mol·d^{-1} for the 24 wt.% Pu-doped MOX pellet, and large and small 10 wt.% Pu-doped MOX pellets respectively. The theoretical steady-state concentrations may be calculated using Eq.(19), assuming that the reaction rate between H_2O_2 and MOX can be approximated by the reaction between H_2O_2 and UO_2 using the Hossain et al. constant of $7.56 \cdot 10^{-8}$ m·s^{-1} [107]. For the small 10 wt.% Pu-doped MOX pellet, the steady-state concentration is calculated from Eq.(19) using δ_{max} = 43 µm and $r_{H2O2} = 7.21 \cdot 10^{-8}$ M·s^{-1}, resulting in $[H_2O_2]_{ss} = 4.10 \cdot 10^{-5}$ M. Under D_2 atmosphere, Eq.(20) can be used. For the 24 wt.% Pu-doped pellet with an average α-particle energy of 5.44 MeV, δ_{max}=44.1 µm, $r_{H2O2} = 2.03 \cdot 10^{-7}$ M·s^{-1}, and D = 2.02 Gy·s^{-1}, gives a value for $[H_2O_2]_{ss}$ equal to $1.19 \cdot 10^{-4}$ M, which yields $[H_2O_2]_{ss,H2} = 2.77 \cdot 10^{-6}$ M. However, care must be taken to apply the equation to values below the theoretically predicted critical concentration. These predicted steady-state concentrations are compared to the experimental values in Chapter 6.6.4.

6.3. External irradiation of UO_2 (Paper III)

6.3.1. NaHCO3 solution experiments

In the external irradiation experiments, a 30 µm solution layer between the Am-241 sources and UO_2 pellet surfaces was irradiated. In the 10 mM $NaHCO_3$ solution experiments using the 3.30 MBq Am-241 source under 10 bar Ar and H_2 atmospheres, the concentrations over the experiment were measured using ICP-MS. The concentration evolution is shown in Figure 6.2. The initial 15-day period shows almost no dissolution. This might be due to the low initial oxidation state of the surface not being sufficiently oxidized to cause notable dissolution. After this period, the dissolution under Ar atmosphere was significantly faster than under H_2 atmosphere. This shows that H_2 has an inhibiting effect on dissolution by radiolytic oxidation, even with external α-radiolytic induced oxidation of UO_2 at room temperature. Ultracentrifugation of the samples from the Ar atmosphere experiment showed no colloids or particles present.

The volumes, $NaHCO_3$ concentrations, source strengths, exposure times, and resulting dissolved uranium concentrations in the external Am-241 irradiation experiments are summarized in Table 6.1. The H_2 atmosphere leads to a significantly lower uranium release under exposure to both the 1.85 and 3.30 MBq sources, in both 0 and 10 mM $NaHCO_3$ solutions. In two experiments studying exposure to the 1.85 MBq Am-241 source in MQ solution under H_2 atmospheres for 11 days, the dissolved uranium concentrations were below limit of detection of the ICP-MS measurement. In one of the two Ar atmosphere experiments where exposure to the 1.85 MBq Am-241 source was studied in MQ solution, the concentration was also below the detection limit ("Ar, 10 bar 1" Table 6.1), while in the other ("Ar, 10 bar 2" Table 6.1) it reached $5.1 \cdot 10^{-8}$ M.

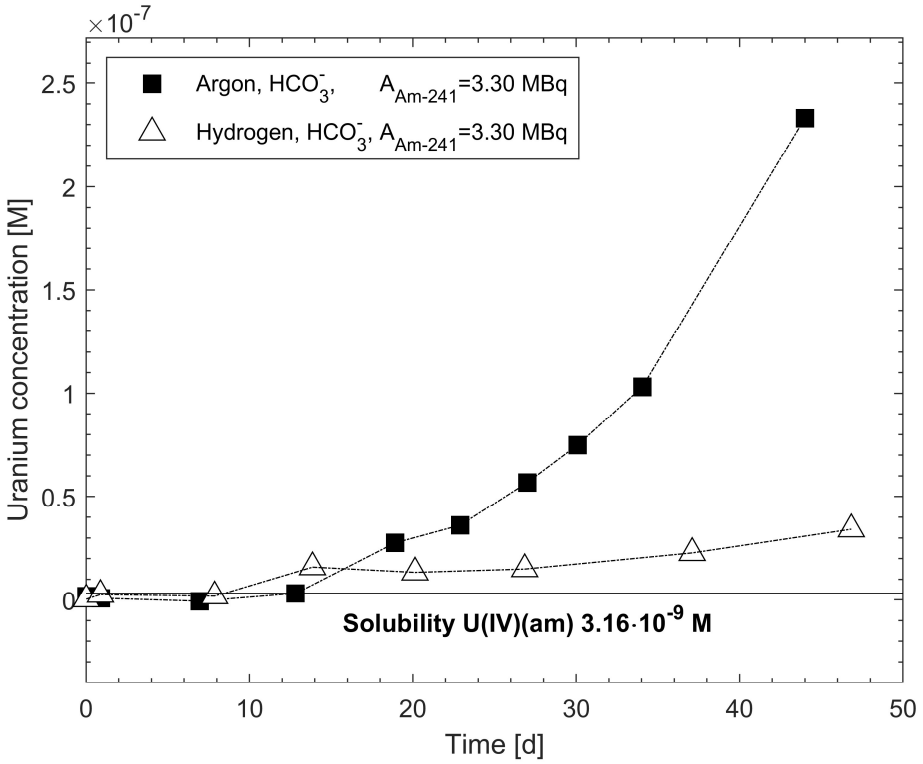

Figure 6.2. Dissolved uranium concentrations in 10 mM $NaHCO_3$ solution in contact with the UO_2 pellet next to the 3.30 MBq Am-241 source under Ar and H_2 atmospheres. The U(IV)(am) solubility is taken from the work of Neck and Kim [47].

Using the 3.30 MBq Am-241 source led to measurable concentrations under both atmospheres during both short and long exposure times. The 11-day exposure experiments in MQ solution using the 3.30 MBq source led to higher dissolved uranium concentrations, as compared to the 10 mM $NaHCO_3$ solution after the same time. This was unexpected due to the rather strong complexing nature of HCO_3^- toward U(VI) [130]. Increased dissolution in $NaHCO_3$ solution would also prevent the formation of an oxidation layer, which could block further dissolution [49]. However, the MQ solution volumes were a factor 3-4 lower than the 10 mM $NaHCO_3$ ones (~45 mL compared to ~150 mL), which may have influenced the dissolution behavior and concentration in the solution. The decreased uranium releases in HCO_3^- solution were also observed in the early stages in the work of de Pablo et al., where it was hypothesized that the radical scavenging effect of HCO_3^- would contribute to lower production of H_2O_2 and a decrease in surface oxidation. This leads to the formation of $CO_3^{\cdot -}$, which itself is a strong oxidant [131], making the radical scavenging effect somewhat difficult to assess. However, it is argued that the $CO_3^{\cdot -}$ radical is much less reactive than the ·OH radical, which may have caused the observed effect [132]. At the end of the 45 days under Ar atmosphere, the $NaHCO_3$ solution experiment gave a factor two higher uranium concentration under exposure to the 3.30 MBq Am-241 source, as compared to in pure MQ solution. A higher uranium concentration was also found at the end of the experiments in the work of de Pablo et al. in HCO_3^- solution compared to MQ solution [132]. This indicates that HCO_3^- only delays the dissolution during the initial stages, and gives a higher overall dissolution towards the later stages of the experiment.

At the end of the 45-day exposure to the 3.30 MBq source in MQ solution, the pH was measured at 6.9±0.5 using an electrode outside of the glove box. The low ionic strength of the sample and exposure to air during the pH measurement contributed to the uncertainty of the measurement.

Table 6.1. Concentrations, volumes and times of the external irradiation experiments.

A_{Am-241} [MBq]	Atmosphere	Volume [mL]	$NaHCO_3$ [M]	Time [d]	U concentration [M]
1.85	H_2, 10 bar 1	45.09	0	11	- †
1.85	H_2, 10 bar 2	44.06	0	11	- †
1.85	Ar, 10 bar 1	45.15	0	11	- †
1.85	Ar, 10 bar 2	42.73	0	11	$5.09 \cdot 10^{-8}$
3.30	H_2, 10 bar 1	44.43	0	11	$1.84 \cdot 10^{-8}$
3.30	H_2, 10 bar 2	43.34	0	11	$3.53 \cdot 10^{-8}$
3.30	Ar, 10 bar 1	43.45	0	11	$2.29 \cdot 10^{-7}$
3.30	Ar. 10 bar 2	43.64	0	11	$3.19 \cdot 10^{-7}$
3.30	Ar, 10 bar	153.01	0	45	$1.26 \cdot 10^{-7}$
3.30	H_2, 10 bar	154.54	$10 \cdot 10^{-3}$	47	$3.42 \cdot 10^{-8}$
3.30	Ar, 10 bar	153.93	$10 \cdot 10^{-3}$	44	$2.33 \cdot 10^{-7}$

† Below the detection limit of the ICP-MS measurement.

In the analogous experimental setup by Sunder et al., shorter exposure times of 100 h and considerably stronger Am-241 sources (of up to 14.8 MBq) were studied under 100 °C [58]. In their work, the dissolved uranium concentrations increased with increasing source strength under N_2 atmosphere. Under H_2 atmosphere, the opposite was found, with decreasing uranium concentrations and increasing Am-241 source strength. It should be mentioned that the uncertainties in the uranium concentration measurements in the work of Sunder et al. were rather large, making the trends somewhat hard to evaluate [58]. The measured uranium concentrations were of the order of 10^{-8} M in Sunder et al., with no notable difference between the H_2 and N_2 atmospheres. This is different to the results found in the present work, where the H_2 atmosphere resulted in significantly lower dissolved uranium concentrations. However, the XPS measurements by Sunder et al. gave a significantly lower surface oxidation state under H_2 atmosphere, indicating that the atmosphere had led to inhibition of the radiolytic oxidation. However, the reduction of U(VI) to U(IV) in Sunder et al. was likely due to thermal activation of H_2, as a temperature of 100 °C was used [58]. In the work of Ekeroth et al., a slow reduction of U(VI) to U(IV) by H_2 was found at temperatures of 74-100 °C [133]. However, Spahiu et al., observed no homogeneous reduction at 70 °C, in the absence of a UO_2 surface [79].

6.3.2. XPS – U4f spectra

Sputtering was carried out on a UO_2 pellet (with natural uranium composition) with a low surface oxidation state for one minute, using the Ar^+-beam to remove the pre-oxidized layer and other surface contamination. The resulting U4f spectrum is shown in Figure 6.3. The $U4f_{5/2}$ and $U4f_{7/2}$ peak positions are lower by 0.5 eV than expected from U(IV) compared to literature values (Table 3.2) [113, 116]. The spin-orbit splitting, or separation between the $U4f_{5/2}$ and $U4f_{7/2}$ peaks of 10.9 eV, corresponds well with the literature values [113, 134]. The spectrum

is, therefore, shifted to a lower energy by 0.5 eV. Van den Berge et. al. found a similar shift, which was believed to be due to charge correction procedures [117]. This is likely also the case in the present work. The clear $U4f_{5/2}$ and $U4f_{7/2}$ satellites are shifted by 6.9 eV from their main peaks, corresponding exactly with the shift of a U(IV) oxidation state (Table 3.2). Thus, the sputtered surface corresponds to a pure U(IV) state. This means the FWHM for the U(IV) component can be determined with a 70%-30% Gaussian-Lorentzian shape as 1.7 eV, which corresponds well with literature values. Furthermore, the value is on the lower end which indicates a fine resolution of the measurement [135]. These parameters were used throughout the work.

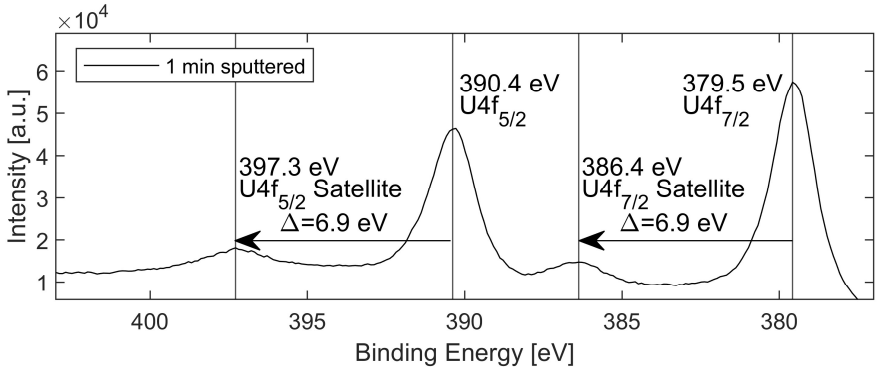

Figure 6.3. The U4f spectrum of a UO_2 pellet after washing and 1-minute Ar^+ ion sputtering.

6.3.3. 11-day exposure under Ar atmosphere

The initial surface oxidation state was measured with XPS directly after the washing process steps and after exposure to the Am-241 sources. This allows for a direct comparison of the surface oxidation state before and after exposure. The U4f spectra after the washing step and before exposure to the 1.85 and 3.30 MBq Am-241 sources are shown Figure 6.4a and Figure 6.4b respectively. The positions of the $U4f_{7/2}$ peaks have greater energy than the $U4f_{7/2}$ peak on the sputtered UO_2 surface (Figure 6.3), showing that some oxidation in the form of U(V) or U(VI), or a combination of the two, is still present on the surface after the washing procedure. This is due to a somewhat ineffective washing procedure or oxidizing conditions in the glove box atmosphere.

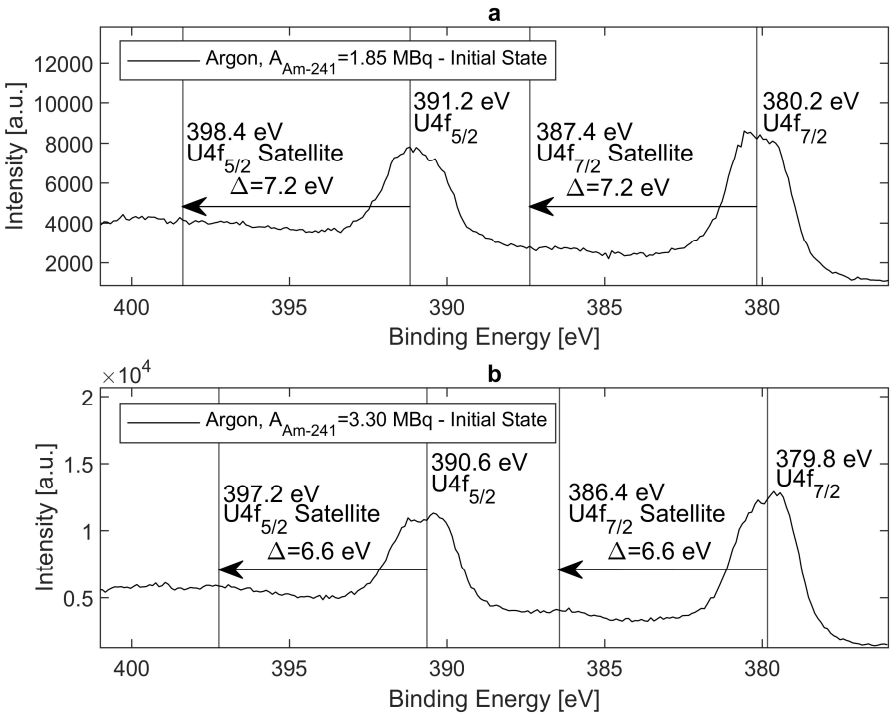

Figure 6.4. U4f spectra of the HCO_3-washed UO_2 pellets before exposure to the 1.85 (a) and 3.30 MBq (b) Am-241 sources under Ar atmosphere.

The U4f$_{7/2}$ peaks after 11 days' exposure to the 1.85 and 3.30 MBq sources in MQ solution under Ar atmosphere are shown in Figure 6.5a and Figure 6.5b respectively ("Ar, 10 bar 2" Table 6.1). The pellet exposed to the 1.85 MBq Am-241 source has a lower U4f$_{7/2}$ peak energy than measured before exposure, with a shift of 0.6 eV. This indicates that the surface oxidation state was reduced, likely due to dissolution of the pre-oxidized layer at a higher rate than the radiolytic oxidation caused by the 1.85 MBq Am-241 source. The resulting U4f$_{7/2}$ peak at 379.6 eV with a satellite shift of 6.8 eV corresponds to a pure U(IV) state on the pellet surface. The UO_2 pellet exposed to the 3.30 MBq Am-241 source shows a positive shift of the U4f$_{7/2}$ peak position by 0.8 eV. The satellites are quite diffuse with a shift of approximately 7.9 eV, indicative of a significant U(V) oxidation state on the surface. The value agrees well with the satellite shifts of 7.8-8.3 eV reported for U(V) compounds in Ilton and Bagus' review [113] and the work of Gouder et al. [136]. Duplicate experiments were carried out and showed good agreement (Table 6.1).

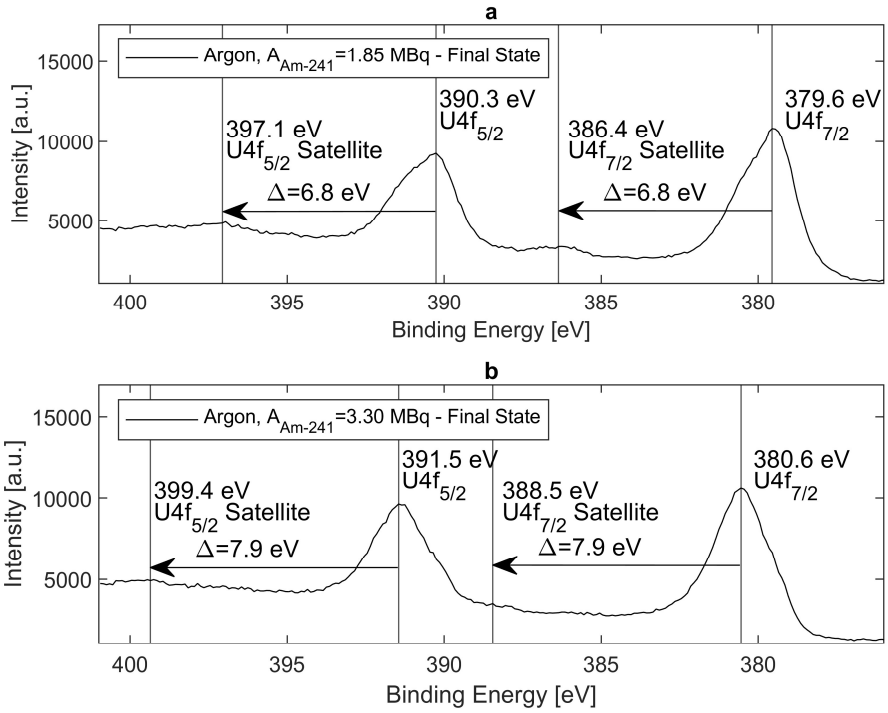

Figure 6.5. U4f spectra after 11 days' exposure to the 1.85 (a) and 3.30 MBq (b) Am-241 sources under Ar atmosphere.

The $U4f_{7/2}$ peak deconvolution into its U(IV), U(V) and U(VI) components is shown for the 1.85 and 3.30 MBq sources in Figure 6.6a and Figure 6.6b respectively. All reported deconvoluted results are after Shirley background subtraction. The deconvolution of the peak on the UO_2 pellet exposed to the 1.85 MBq source gave an oxidation state equal to $UO_{2.07}$. The pellet exposed to the 3.30 MBq source had a significantly higher shift in its $U4f_{7/2}$ peak position, which was deconvoluted to an oxidation state of $UO_{2.44}$. However, the results from the $U4f_{7/2}$ peak deconvolution are somewhat uncertain due to the non-negligible influence of U(IV)-, U(V)- and U(VI)-component positions in the fit. This means that rather small changes in the position of a single component can have a noticeable effect on the outcome of the deconvolution.

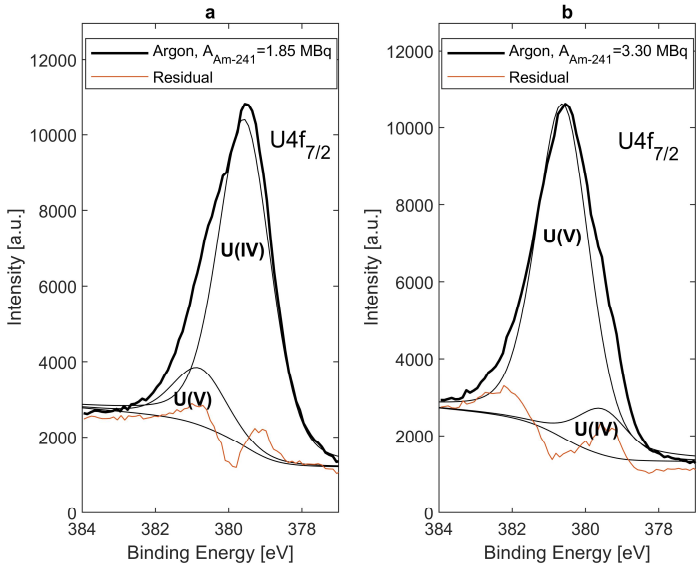

Figure 6.6. Deconvolution of the U4f$_{7/2}$ peaks measured on the surface of the UO$_2$ pellets exposed for 11 days to the (a) 1.85 and (b) 3.30 MBq Am-241 sources under Ar atmosphere.

6.3.4. 45-day exposure under Ar atmosphere

The U4f spectrum of the UO_2 pellet exposed to the 3.30 MBq source for 45 days under Ar atmosphere in MQ solution is shown in Figure 6.7. Both the U4f$_{7/2}$ peak position and satellite shifts are discernably higher than the initial state samples and sputtered pellet.

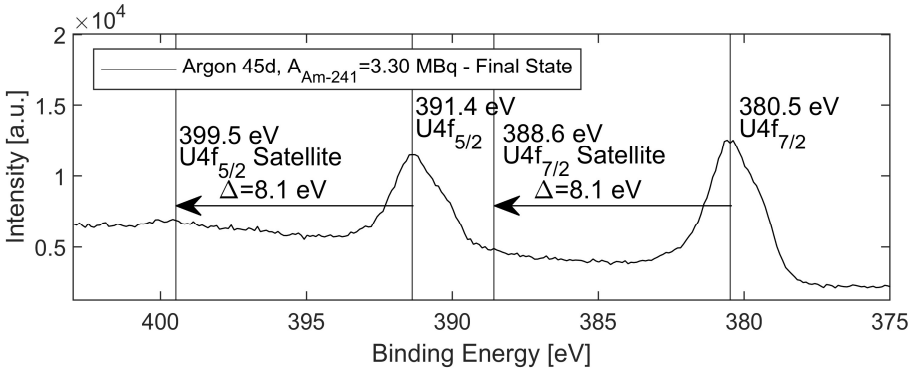

Figure 6.7. U4f spectrum of a UO$_2$ pellet after 45 days' exposure to the 3.30 MBq Am-241 source under Ar atmosphere.

The results of the deconvolution of the U4f$_{7/2}$ peak are shown in Figure 6.8. The main oxidation state is U(V) with a U(V)/U(IV) ratio of 1.88, equivalent to $UO_{2.33}$. The satellite shift of ~8.1 eV also corresponds well with a considerable U(V) oxidation state component. However, the satellites are diffuse and somewhat hard to pinpoint. Compared to the 11-day experiment, the oxidation state from the deconvolution indicates a lower amount of oxidation after the 45-day exposure. However, the solution volume was 3.5 times larger in the 45-day experiment, and the total dissolved uranium amounts were roughly a factor two larger, indicating that more uranium was oxidized on the surface (and subsequently dissolved) during the longer exposure.

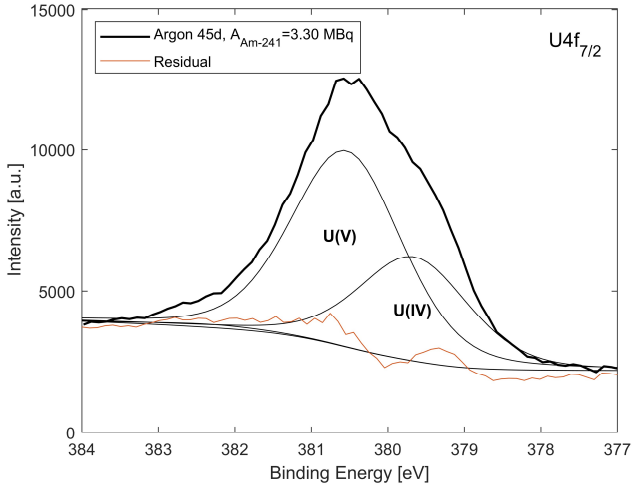

Figure 6.8. Deconvolution of the U4f$_{7/2}$ peak from a UO_2 pellet after 45 days' exposure to the 3.30 MBq Am-241 source under Ar atmosphere.

6.3.5. 11-day exposure under H_2 atmosphere

The surface status of the UO_2 pellets was measured after the initial washing process and after exposure to the 1.85 and 3.30 MBq Am-241 sources under 10 bar H_2 atmosphere for 11 days. The initial U4f spectrum is shown in Figure 6.9. The initial U4f states on both UO_2 pellets correspond well with the sputtered reference state. Both the peak energies and corresponding satellites indicate an almost pure U(IV) state. The somewhat less clear satellite peaks (compared to the sputtered sample) indicate a small influence of U(V).

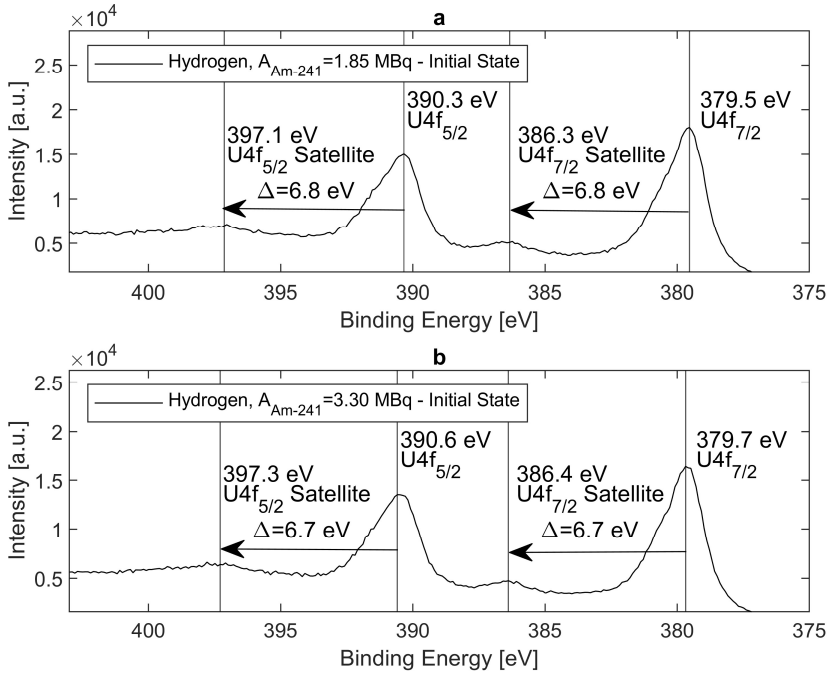

Figure 6.9. U4f spectra of the UO_2 pellets after the carbonate washing procedure, before exposure to the 1.85 (a) and 3.30 MBq (b) Am-241 sources under H_2 atmosphere.

The U4f spectrum after exposure to the Am-241 sources for 11 days under H_2 atmosphere can be seen in Figure 6.10 ("H_2, 10 bar 2" Table 6.1). The spectra have not changed notably compared to the initial state. The $U4f_{7/2}$ peak energy position on the surface exposed to the 1.85 MBq source was shifted to a somewhat lower energy, but this shift is almost negligible. The results from both spectra indicate an almost pure U(IV) state, judging from the $U4f_{7/2}$ peak and satellite energy positions. This shows that the H_2 atmosphere inhibits the radiolytic oxidation of the UO_2 surface exposed to the 3.30 MBq source, as significant oxidation was observed in the 10 bar Ar atmosphere experiments with this source strength. This is supported by the lower concentrations of dissolved uranium. These were an order of magnitude lower at the end of the H_2 atmosphere experiment of $3.5 \cdot 10^{-8}$ M, compared to $3.2 \cdot 10^{-7}$ M under Ar atmosphere (Table 6.1). The results were replicated in a second experiment with consistent results.

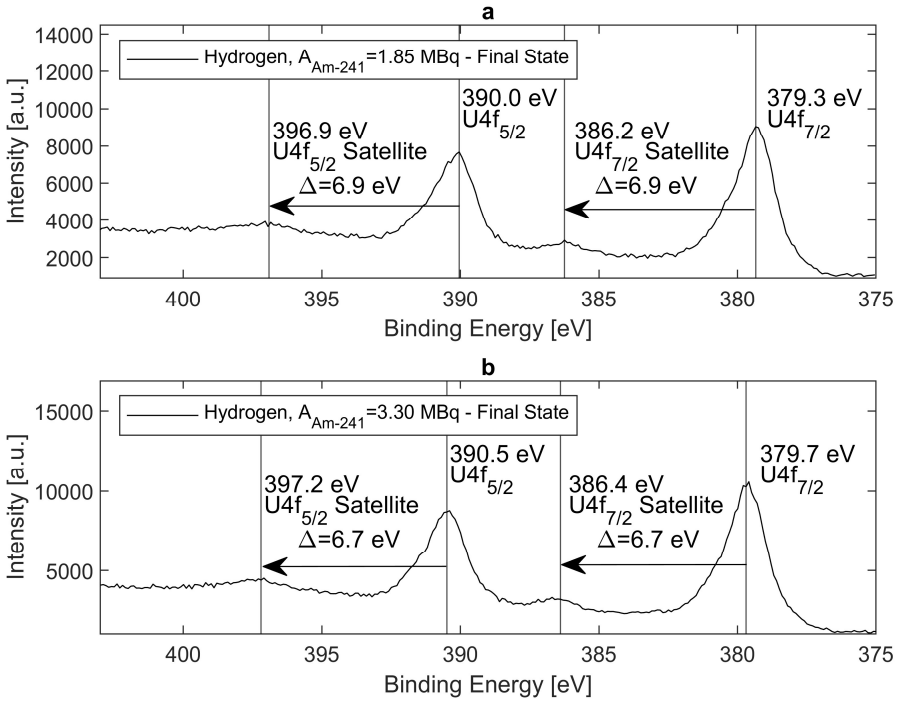

Figure 6.10. U4f spectra of the UO_2 pellets after 11 days' exposure to the 1.85 (a) and 3.30 MBq (b) Am-241 sources under H_2 atmosphere.

6.3.6. Valence band analysis

The analysis of the valence band region measured on the pellet surfaces before and after the 11-day exposure to the Am-241 sources under Ar and H_2 atmospheres are shown in Figure 6.11 and Figure 6.12 respectively. In the initial states of the UO_2 surfaces, the ratio between the areas of the O2p and U5f peaks is approximately 1.0. All reported area ratios between the O2p and U5f states are after Shirley background subtraction. The results are summarized in Table 6.2. After exposure to the 1.85 and 3.30 MBq sources under Ar atmosphere for 11 days, the O2p to U5f state area ratios are 1.1 and 1.9 respectively. This indicates negligible oxidation during exposure to the 1.85 MBq source, and significant oxidation during exposure to the 3.30 MBq source. The FWHM of the U5f peak on the UO_2 surface exposed to the 3.30 MBq source for 11 days under Ar atmosphere goes from an initial value of 1.28 eV to a final value of 1.13

eV. This agrees well with the results from Gouder et al., in which an FWHM of the U5f peak was measured on pure U_2O_5 (pure U(V)) as 1.19 eV [136]. That work shows that the U(V) oxidation state has a lower intensity and FWHM of the U5f signal compared to the pure U(IV) and U(VI) states, or a mixture of the two [136]. This makes the analysis of the U5f FWHM unambiguous for identifying U(V). At the end of the 45-day exposure to the 3.30 MBq Am-241 source under Ar atmosphere experiment, an FWHM of the U5f peak of 1.11 eV and an O2p to U5f area ratio of 1.9 was found. These results are very consistent with those found at the end of the 11-day experiment (Table 6.2), and support the $U4f_{7/2}$ peak deconvolution results. The results show that the radiolytic oxidation from U(IV) goes through oxidation to the U(V) state, and does not lead to the formation of a mixture of U(IV) and U(VI), which was also observed in the work of Gouder et al. [136].

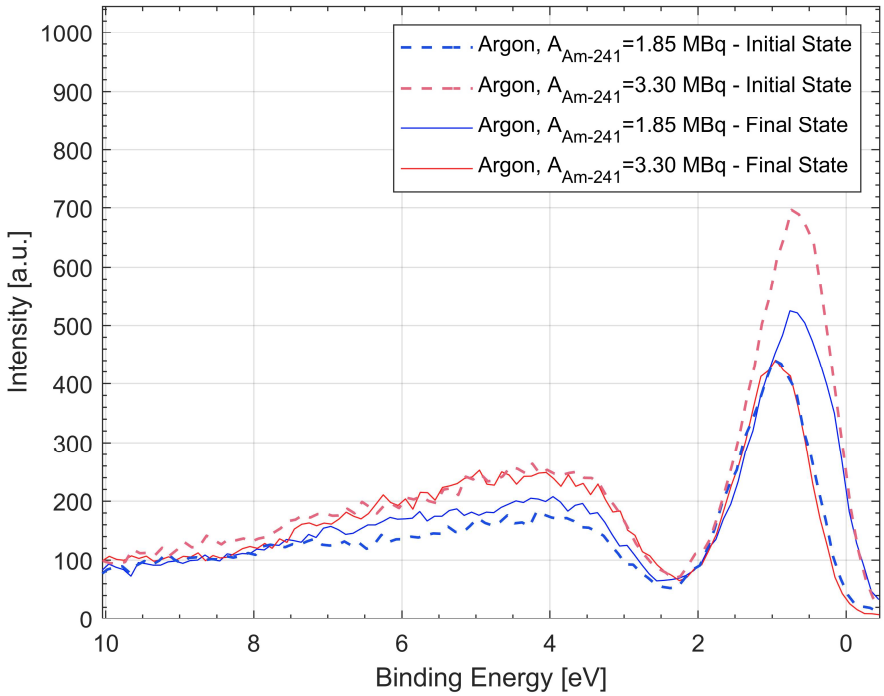

Figure 6.11. Valence band region showing the O2p and U5f peaks of the UO_2 pellets exposed to the 1.85 and 3.30 MBq Am-241 sources under Ar atmosphere.

In the exposure experiments under H_2 atmosphere, the area ratios of the O2p to U5f states are consistent over the experiment (at approximately 1.0), as shown in Figure 6.12 and Table 6.2. The surface oxidation is, therefore, negligible under H_2 atmosphere, as discussed in the U4f region analysis. The FWHMs of the U5f peaks of ~1.4 eV are consistent with the width seen on the sputtered pellet of 1.45 eV. These values are in good agreement with the work of Gouder et al., in which a FWHM of 1.46 eV was found in the measurement of pure U(IV) [136].

Table 6.2 - Valence band and bonding band peak positions from the XPS-measurements.

Condition	Valence band (V.B.) U5f [eV]	FWHM U5f [eV]	Bonding band (B.B.) $O2p_{3/2}$ [eV]	Area ratio (B.B./V.B.)
Ion-sputtered	0.8	1.45	4.1	1.0
Chemical washed	0.8	1.30	4.1	0.9
Ar atmosphere				
1.85 MBq – 11 days	0.7	1.35	4.0	1.1
3.30 MBq – 11 days	0.9	1.13	4.4	1.9
3.30 MBq – 45 days	0.9	1.11	3.4	1.9
H_2 atmosphere				
1.85 MBq – 11 days	0.5	1.45	3.9	1.0
3.30 MBq – 11 days	0.8	1.40	4.5	0.8

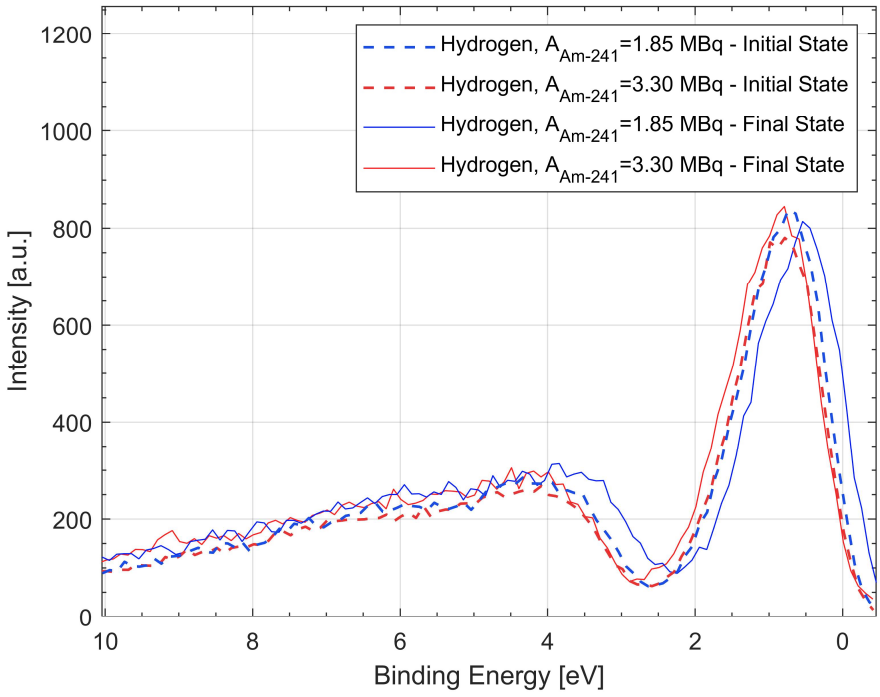

Figure 6.12. Valence band region showing the O2p and U5f peaks of the UO_2 pellets exposed to the 1.85 and 3.30 MBq Am-241 sources under H_2 atmosphere for 11 days.

6.4. Uranyl in contact with corroding iron foils (Paper VII)

6.4.1. Concentration measurements

The calcium, iron and uranium concentrations measured in the A-D experiment batch in contact with the iron foil under 3000 ppm CO_2 in Ar atmosphere using the $FeSO_4$ O_2-trap are shown in Figure 6.13. The initial uranium concentration of $4.2 \cdot 10^{-6}$ M decreased during the experiment toward 10^{-9} M at the end of the 1200 h period for all four experiment series. The calcium is observably stable throughout the experiment at the initial concentration of the groundwater composition. A few data points in experiment C show presence of calcium. This is due to contamination or interference between species with similar mass in the ICP-MS

measurement, as the 10-2 groundwater solution has zero calcium concentration. The iron concentrations are initially similar for all experiment series during the first 200 h, after which the series diverge, and a concentration of ~10^{-3} M is reached in series A and B. In experiment series C and D, the concentrations are in the order of 10^{-5} M.

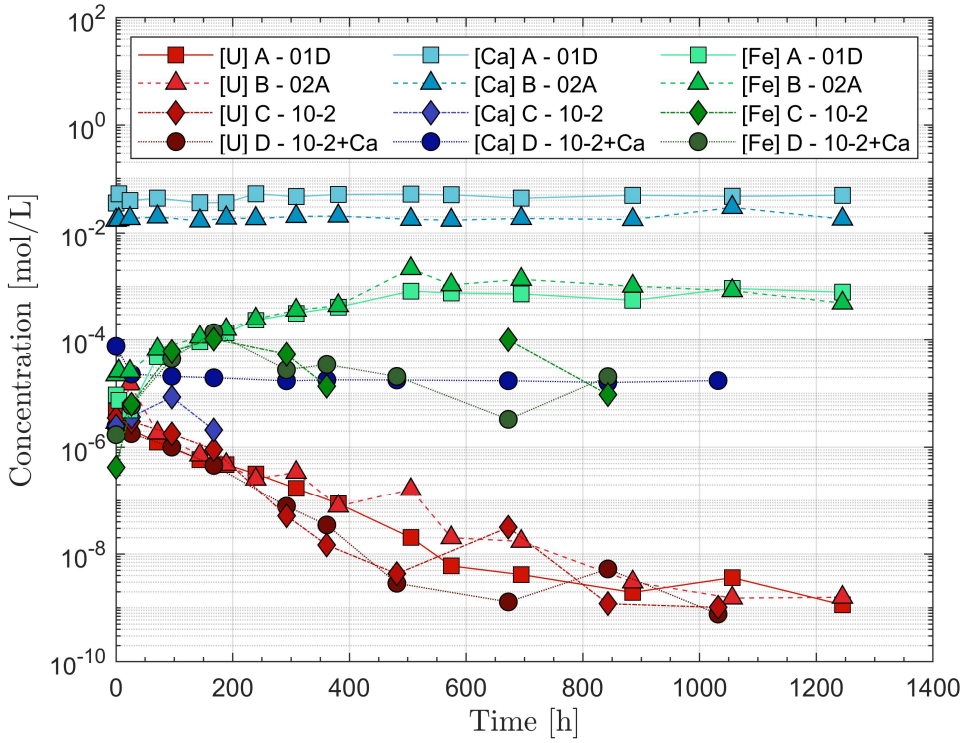

Figure 6.13. 3000 ppm CO_2 in Ar atmosphere batch experiment with samples A-D using the $FeSO_4$ O_2-trap.

Calcium, iron and uranium concentrations were measured in the E-H experiment batch under Ar atmosphere, with 400 ppm CO_2 using the $FeCO_3$ O_2-trap (Figure 6.14). The uranium concentrations decreased to 10^{-8} – 10^{-7} M before increasing somewhat during the final stages of the experiment. This increase is likely due to O_2-contamination, as the uranium concentrations were significantly lower in the A-D experiment batch. However, the calcium concentrations were stable throughout the experiment. Contamination or mass interference shows a low calcium concentration in experiment G (as discussed in the A-D batch). The iron concentrations reach somewhat lower concentrations than in the A-D batch of ~10^{-4} M in experiment series E and F, as compared to A and B of ~10^{-3} M (shown in Figure 6.13).

A duplicate batch with experiment series M-P was studied, under 400 ppm CO_2 in Ar atmosphere using the $FeCO_3$ O_2-trap. O_2-contamination occurred during this batch after approximately 600 – 800 h due to the glove box gas supply running empty. This resulted in an O_2 partial pressure of ~80 ppm in the glove box atmosphere. The data series is shown in Appendix A, Figure A.1.

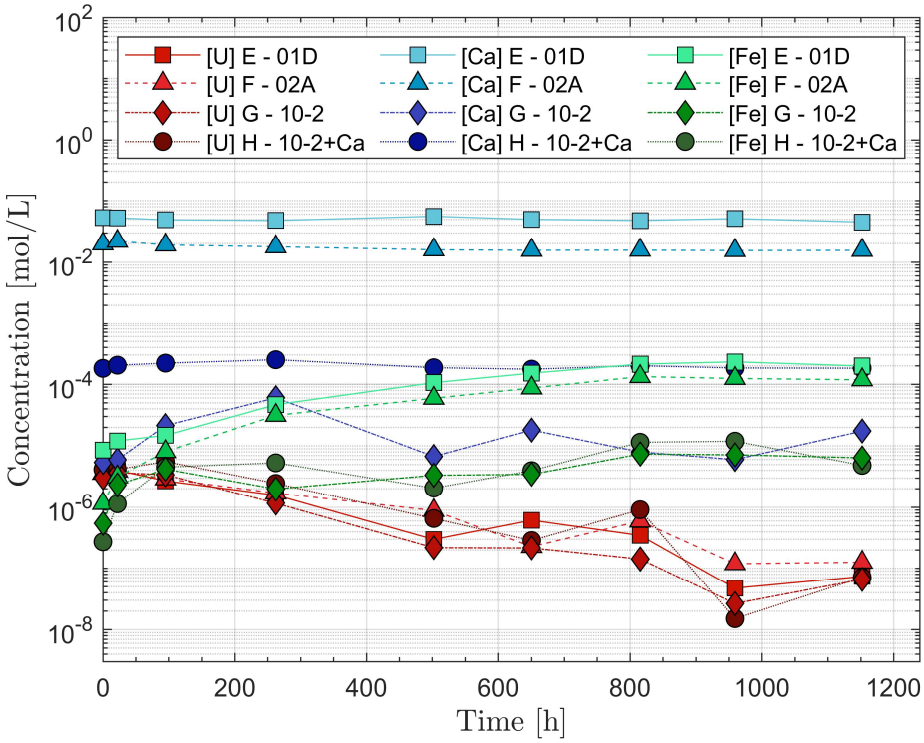

Figure 6.14. 400 ppm CO_2 in Ar atmosphere batch experiment with samples E-H using the $FeCO_3$ O_2-trap.

An additional batch with experiment series I-L was therefore run, under 400 ppm CO_2 in Ar atmosphere using the $FeSO_4$ O_2-trap. The measured calcium, iron, and uranium concentrations are shown in Figure 6.15. The uranium concentrations reached significantly lower values than in the E-H and M-P experiment batches using the $FeCO_3$ O_2-trap, and gave concentrations close to 10^{-9} M as found in the A-D batch. It should be emphasized that the duration was shorter in this batch, of 770 h. The calcium concentrations were stable throughout the experiments. The iron concentrations reached somewhat higher values than in the E-H batch.

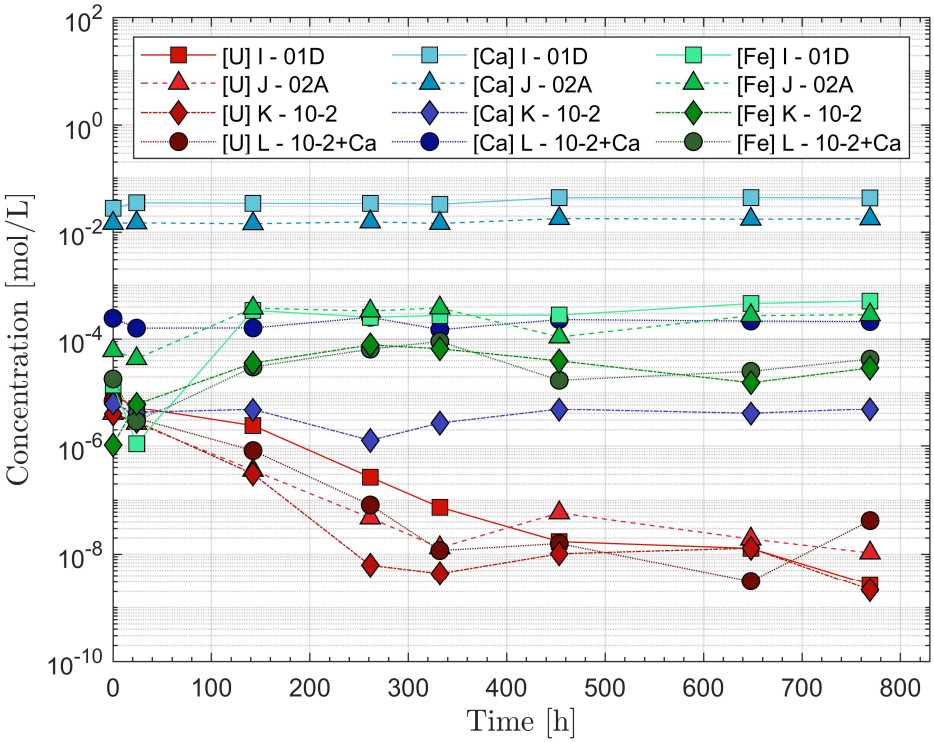

Figure 6.15. 400 ppm CO_2 in Ar atmosphere batch experiment with samples I-L using the $FeSO_4$ O_2-trap.

The kinetics of U(VI) reduction and precipitation in contact with a corroding iron foil was investigated by plotting $\ln(C_t/C_0)$ versus reaction time, where C_t and C_0 are U(VI) concentrations at time t and 0 respectively. Under the present experimental conditions, the reductive sites on the foil surface were well in excess of the dissolved U(VI), allowing the reduction to be approximated with pseudo-first-order reaction kinetics. The natural logarithm of the uranium concentration was taken for the 5-6 first data points in each experiment and the linear trend was fitted by least squares. The slope resulting from this fitting is reported in Table 6.3 as pseudo-first-order rate constants of U(VI) reduction.

Table 6.3. Pseudo-first-order rate constants for the reduction of U(VI) in contact with the corroding iron foil.

Atmosphere	Experiment	Pseudo-first-order rate constant [d^{-1}]
3000 ppm CO_2	A - 01D	$(8.4 \pm 0.48)\cdot 10^{-3}$
	B - 02A	$(8.4 \pm 2.3)\cdot 10^{-3}$
	C - 10-2	$(1.5 \pm 0.11)\cdot 10^{-2}$
	D - 10-2+Ca	$(1.2 \pm 0.08)\cdot 10^{-2}$
400 ppm CO_2	I - 01D	$(1.4 \pm 0.09)\cdot 10^{-2}$
	J - 02A	$(1.8 \pm 0.14)\cdot 10^{-2}$
	K - 10-2	$(2.2 \pm 0.20)\cdot 10^{-2}$
	L - 10-2+Ca	$(1.5 \pm 0.20)\cdot 10^{-2}$
400 ppm CO_2	M - 01D	$(5.2 \pm 0.46)\cdot 10^{-3}$
	N - 02A	$(3.0 \pm 0.16)\cdot 10^{-3}$
	O - 10-2	$(5.6 \pm 0.71)\cdot 10^{-3}$
	P - 10-2+Ca	$(4.6 \pm 1.0)\cdot 10^{-3}$

The corroding iron foils caused considerable reductive precipitation of the dissolved U(VI) in the synthetic groundwater solution. The experiment batches with lower uranium concentrations were accompanied by somewhat higher concentrations of dissolved iron. This might have been due to stronger reducing conditions, or the reduction being promoted by the dissolved iron concentrations. Higher dissolved calcium concentrations had a rather small effect on the reductive precipitation of uranium. The reduction of uranium also seemed to occur to a lesser extent in experiments using the $FeCO_3$ trap. This would be expected given the comparatively low solubility of $FeCO_3$ compared to $FeSO_4$ [137]. The lower solubility would lead to less efficient removal of O_2 from the CO_2 + Ar gas mixture and more O_2-contamination in the glove box atmosphere.

6.4.2. SEM/EDS on iron foils

After removing the iron foils from the synthetic groundwater solution at the end of the experiments, dark-green and blue-green spots were observed on the foil surfaces, characteristic of green rust [138, 139] (Figure 6.16).

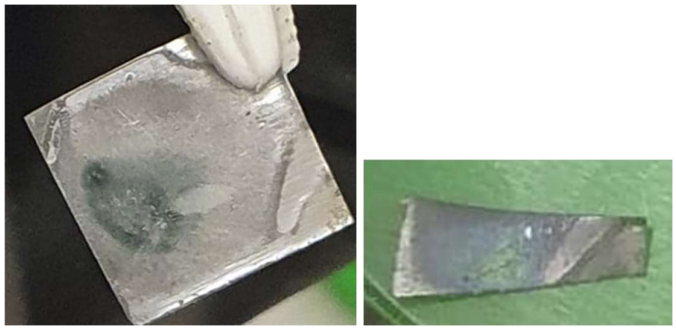

Figure 6.16. Pictures of foil pieces on which a clear green rust spot (a) and a blue-green spot (b) were found at the end of experiments E and F.

The iron foils from batches with experiments E-H and I-L were analyzed using SEM/EDS. The other batches were potentially compromised by O_2-contamination during storage. The SEM images of the iron foils from samples E and F are shown in Figure 6.17. Rather large UO_2 grains can be observed on the iron foil surface, considering the rather low total amount of uranium ($8.4 \cdot 10^{-8}$ moles) present in the experiment. Thus, the uranium is not evenly distributed across the iron foil surfaces, but rather agglomerated on quite few particles. In the iron foils from the experiments using the 01D and 02A groundwaters, features showing quite intricate compositions were found. However, in the EDS analysis of the uranium grains, the composition was found to be rather simple, with almost exclusively O, U, Fe and C. Elemental mapping of the UO_2 grains on the E and F iron foil surfaces showed the grains to be precipitated together with carbon, or on top of carbon-rich spots on the iron foil surface. In Cui and Spahiu's work, which studied very similar experimental conditions (with simpler groundwater composition), uranium was found to have precipitated on top of the carbonate green rust formed on the iron foil surfaces as they corroded under anoxic conditions [67]. Therefore, the carbon content found in the elemental analysis of the UO_2 grains probably belongs to the iron foil corrosion product, on which the uranium was reductively precipitated.

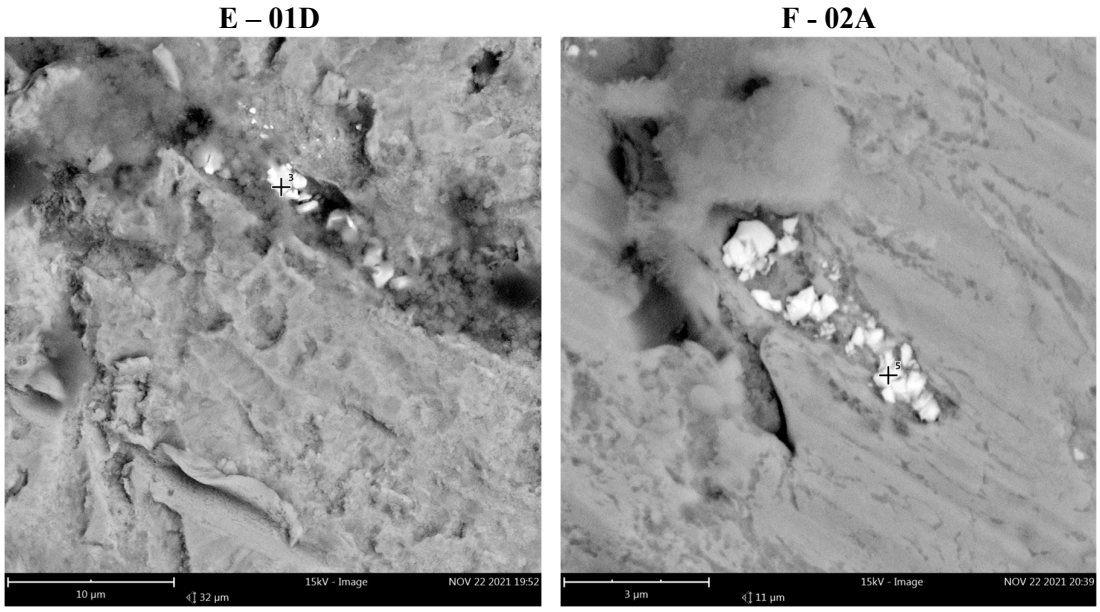

Figure 6.17. SEM analysis of foils E and F, showing the rather simple composition of the precipitated uranium grains.

Generally, a somewhat higher carbon content was found in experiments studying carbonate-rich groundwaters. In the SEM images of the iron foils from experiments K and L, significantly larger uranium grains were found on the iron foil from experiment K. This corresponds well with the ICP-MS solution analysis of experiment K, where very low U concentrations were found. More details may be found in Paper VII.

6.4.3. XPS on iron foils

After the solution experiments, the 375 – 405 eV U4f and the 703 – 720 eV $Fe2p_{3/2}$ regions were analyzed on the iron foils using XPS. Several of the elements present in the synthetic groundwaters 01D and 02A have binding energies in the valence band region, making analysis of this energy region non-viable. The experiment batch with samples A-D was also omitted from the XPS analysis, due to the potential O_2 influence of the iron foil surfaces during sample storage. The rather low total uranium amounts precipitated on the iron foil surfaces led to low intensities in some XPS measurements, making analysis of the spectra more difficult. The U4f spectra of the iron foils from the E-H experiment batch are shown in Figure 6.18. The FWHM of the peaks is small, corresponding to a single oxidation state present on the surface.

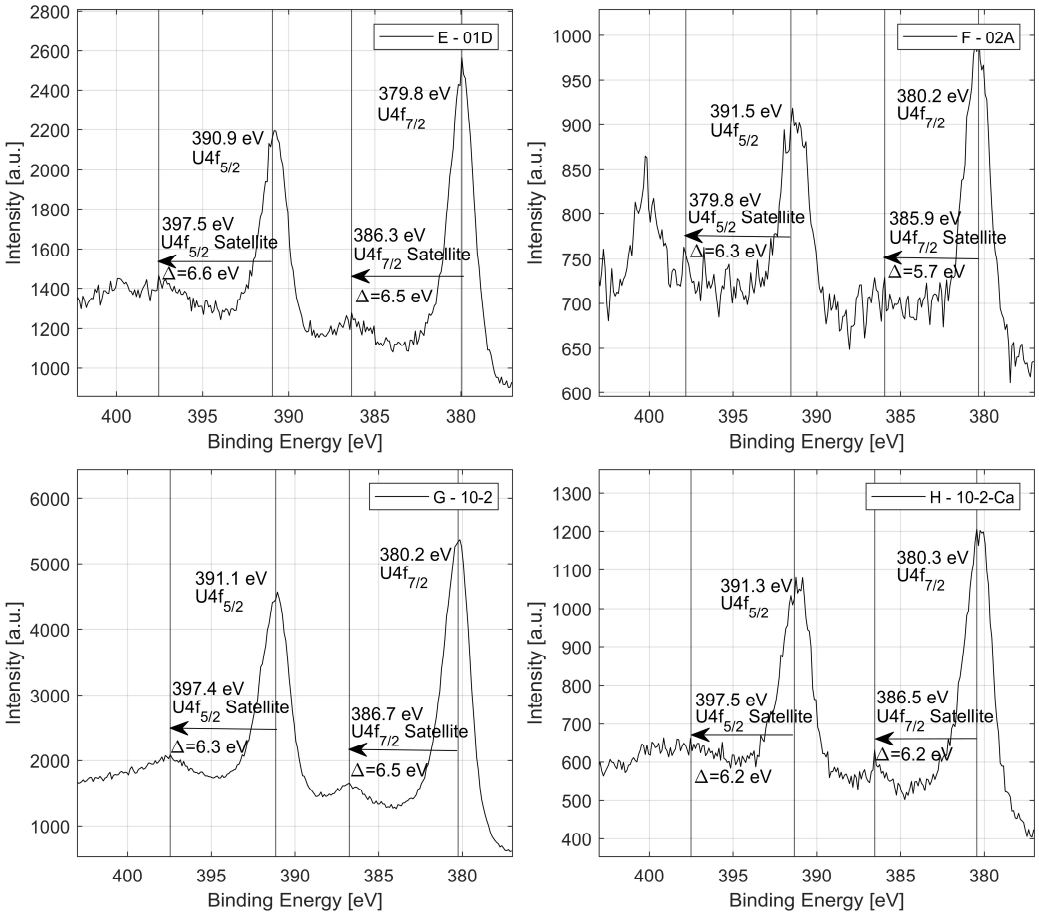

Figure 6.18. $U4f_{7/2}$ and $U4f_{5/2}$ peak XPS measurements with corresponding satellites.

The energies of the $U4f_{7/2}$ peaks in the E-H experiment batch are very similar to that of U(IV), as shown in Table 3.2. This indicates that the uranium has precipitated out of solution due to the low solubility of reduced uranium in the U(IV) state. In the external irradiation experiments of UO_2 pellets (discussed in Chapter 6.3), the $U4f_{7/2}$ peak position was shifted by approximately 0.5 eV toward lower energies, giving a pure U(IV) state at 379.5 eV. The energy positions of the $U4f_{7/2}$ and $U4f_{5/2}$ peaks shown in Figure 6.18 indicate that the shift to lower energy is not present on the iron foil surfaces. The $U4f_{7/2}$ and $U4f_{5/2}$ satellites correspond quite well with the U(IV) satellite energy shift of ~6.9 eV (Table 3.2). This supports the notion that the spectrum is not shifted toward lower energies, as was found on the UO_2 pellets. However, the satellite shifts are somewhat lower than the expected U(IV) value. Even so, this does not indicate U(V), as the satellites would have a higher energy shift from the main $U4f_{7/2}$ and $U4f_{5/2}$ peaks as compared to U(IV). There might, therefore, be a slight influence of U(VI). It should also be mentioned that the shift in the spectrum to the adventitious carbon C1s signal of 284.8 eV might introduce some uncertainty into the measurements, as this signal may depend on the carbon's chemical state.

The U4f spectra measured on the iron foils from the I-L experiment batch are shown in Figure 6.19. The FWHM of the $U4f_{7/2}$ peaks is small, corresponding to a single oxidation state. The energies of the $U4f_{7/2}$ peaks on the I and K samples are approximately 1 eV lower, as compared

to what was observed on the iron foils from the J and L experiments, and the experiment batch E-H shown in Figure 6.18. As this is a significant shift, U(IV) might be present in a different chemical state to that on the other foil surfaces. In the final data point, the uranium concentrations found in the solution analysis of experiments I and K show concentrations approximately one order of magnitude lower than in experiments J and L. However, the lower energy may be due to a different C1s component on the surface, shifting the energy of the spectrum down by a notable amount.

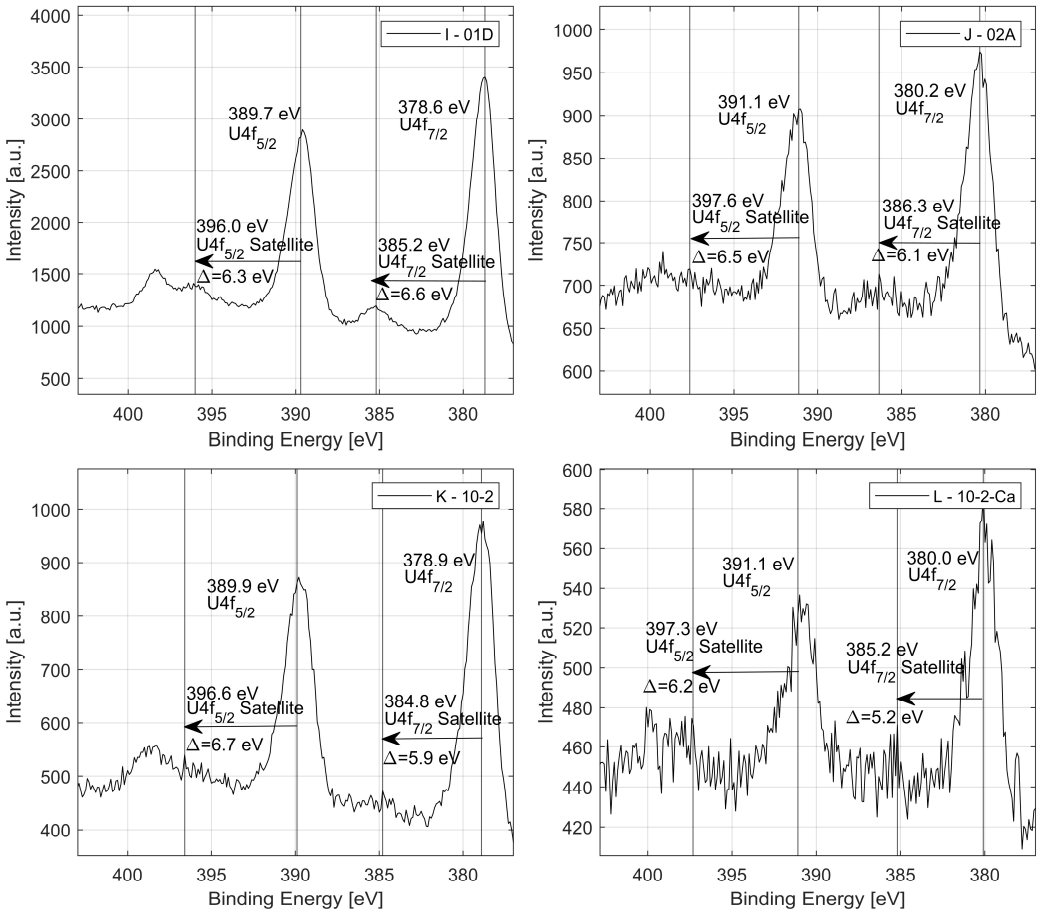

Figure 6.19. U4f$_{7/2}$ and U4f$_{5/2}$ peak XPS measurements with corresponding satellites.

The U4f spectrum measured on the iron foil from the O_2-contaminated experiment M was found to still have a general U4f$_{7/2}$ peak position of 380.3 eV, corresponding to a very low oxidation state. However, a few crystallite features were also observed on this foil. The U4f spectra of these features are shown in Figure 6.20. Feature 2 has significantly higher U4f$_{7/2}$ peak energy than the energy measured on the iron foils from experiments E-H and I-L, indicating that some spots were significantly oxidized. Thus the oxidation was not uniform on the uranium spots on the iron foil surface, but rather concentrated to significantly oxidized spots.

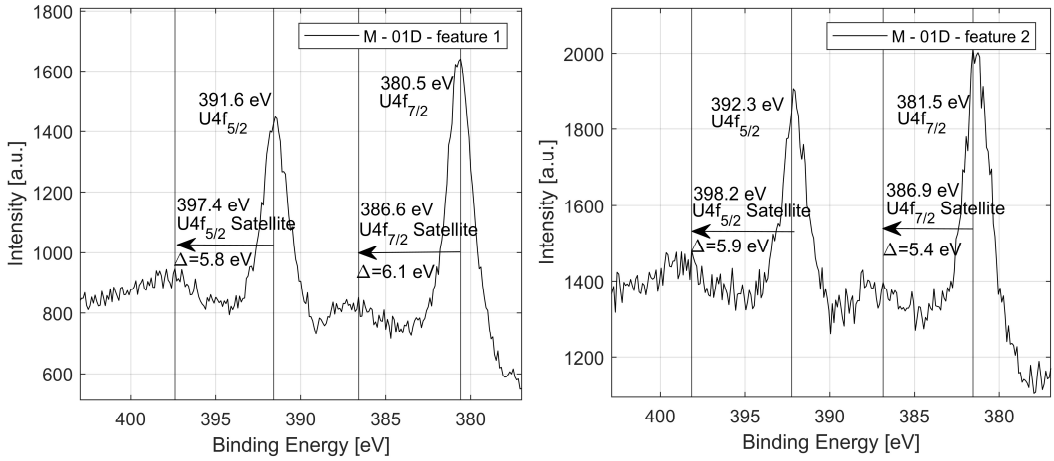

Figure 6.20. XPS measurement of the U4f$_{7/2}$ and U4f$_{5/2}$ peaks of the iron foil from experiment M. The second feature represents an oxidized state, likely due to the O_2-contamination during the experiment.

The Fe2p$_{3/2}$ peaks were also analyzed on the E-H and I-L iron foil surfaces, and were deconvoluted into its Fe(0), Fe(II)$_{oct}$, Fe(III)$_{oct}$, Fe(III)$_{tet}$, Fe(II)$_{sat}$ and Fe(III)$_{sat}$ components. The Fe(III)/Fe(II) ratio gives values fairly close to 1 for all foils, which represents a higher amount of Fe(II) than is present in magnetite, which has a ratio of 2. The ratio also corresponds to an oxide with a lower amount of Fe(II) than would be expected from most green rust compositions, e.g., carbonate green rust has a ratio of 0.5 [138]. This could indicate a mixture of the two corrosion products. Further details may be found in Paper VII.

Dewey et al. found that the calcium-uranyl-carbonato complexes significantly limited the homogeneous reduction of uranium in the presence of Fe(II)(aq) [89]. They also found that, in the heterogeneous reduction of U(VI) by ferrihydrite, the calcium-uranyl-carbonato complexes lead to a stabilization of U(V) which was not further reduced to U(IV) to any substantial extent. A much weaker influence of the calcium-uranyl-carbonato complex has therefore been found in the present work.

6.5. SIMFUEL leaching experiment (Paper II)

The concentrations from the SIMFUEL leaching experiment, using 2.5 mM initial H_2O_2 concentration under 10 bar D_2 atmosphere, are shown in Figure 6.21 (with dissolved uranium amounts on the left y-axis and consumed H_2O_2 on the right y-axis). The ratio between dissolved uranium and consumed H_2O_2 was on average $1.69 \cdot 10^{-4}$. This demonstrated a very efficient H_2O_2 decomposition without oxidative dissolution of the UO_2 matrix under D_2 atmosphere. This effect would be important in a future water-intrusion scenario in the deep geological repository, where a low oxidation state can be maintained by H_2 activation on ε-particles, even under high oxidant concentration conditions. HDO analysis is shown alongside the MOX leaching experiment data in Chapter 6.6.6 in Figure 6.27.

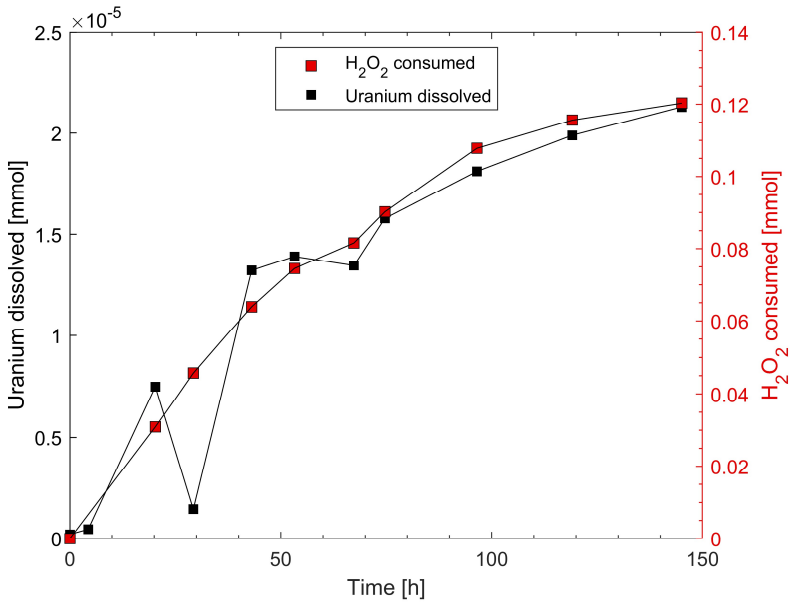

Figure 6.21. Dissolved uranium from the SIMFUEL pellet under D_2 atmosphere using an initial addition of H_2O_2. The consumed H_2O_2 is also shown on the right y-axis.

6.6. MOX pellet leaching experiment (Papers I and VI)

6.6.1. XRD spectroscopy

A 10 wt.% Pu-doped MOX pellet annealed at 1200 °C for 5 h in N_2 with 5% H_2 (with additional 1 h heating and cooling periods) was measured using XRD. The spectrum is shown in Figure 6.22. The majority of the peaks could be fitted to an FCC structure with a=5.4592 Å. This is 99.92% of the theoretical lattice parameter of $(U_{0.90}Pu_{0.10})O_2$ of 5.4635 Å, calculated using Vergard's Law. For all MOX compositions, the lattice parameter decreases as the O/M ratio increases [140]. The peaks correspond well to a $(U_{0.85}Pu_{0.15})O_2$ phase (red lines, shown in Figure 6.22). However, it is hard to discern the Pu content in $(U_{1-x}Pu_x)O_2$ with any great precision using XRD without precise calibration. This explains why the Pu content is somewhat overestimated. However, the secondary peaks at 29.11, 33.70, 48.37 and 57.40 degrees 2θ could not be fitted using the $(U_{0.85}Pu_{0.15})O_2$ structure. These peaks correspond to an FCC phase with lattice parameter 5.322 Å at hkl indices 111, 200, 220 and 311. This could potentially correspond to a uranium nitride phase, such as UN_2 which is reported as 5.31 Å [141]. A uranium nitride phase was included in the XRD spectrum (blue lines, Figure 6.22). A secondary annealing was carried out using 5% H_2 in Ar at 1200 °C for 5h. The secondary peaks were removed entirely, which supports the hypothesis that the peaks correspond to a nitride phase.

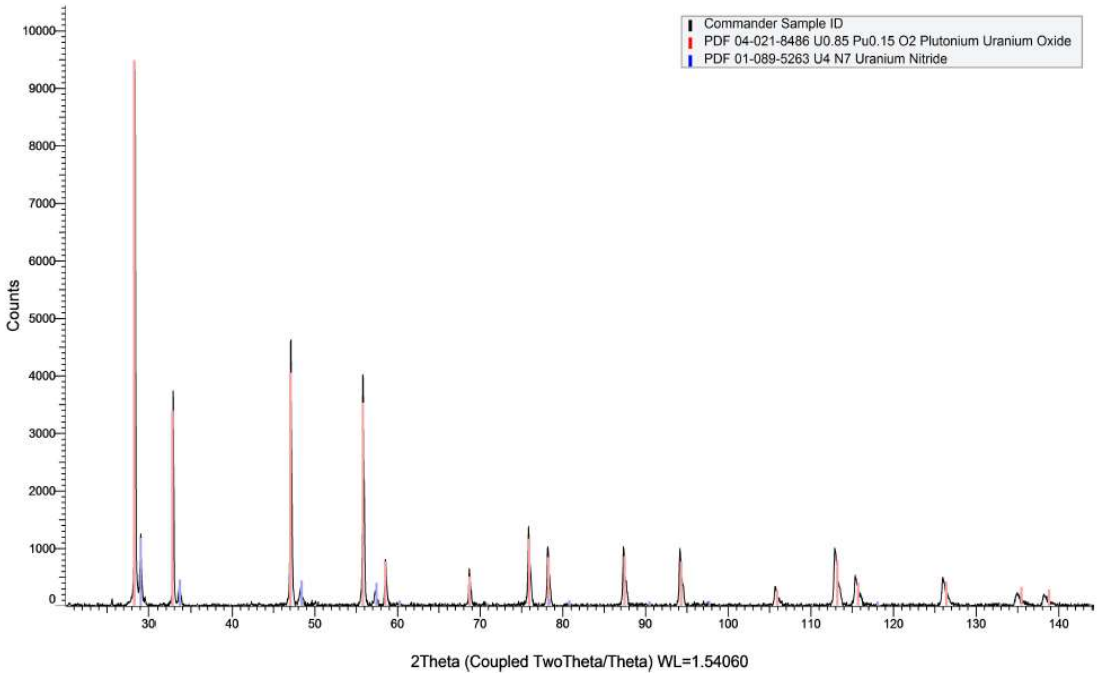

Figure 6.22. XRD measurement of a 10 wt.% Pu-doped MOX pellet after annealing at 1200 °C in N_2 with 5% H_2 for 5h with 1 h heating and cooling periods. The peaks from a $(U_{0.85}Pu_{0.15})O_2$ structure and a uranium nitride structure are shown in red and blue respectively.

6.6.2. MOX leaching under Ar atmosphere

Leaching experiments of the 10 and 24 wt.% Pu-doped MOX pellets were conducted for 60 – 400 days under 10 bar Ar atmosphere. The samples were ultracentrifuged prior to ICP-MS measurements to remove any particles or colloids. The concentration evolution for the initial 85-day period is shown in Figure 6.23. The dissolution was initially very slow during the first 20 days, after which the dissolved uranium concentrations started to increase around the 30 – 40 day mark. The slow initial dissolution phase may have been due to the stoichiometric (or potentially sub stoichiometric) surface after the annealing procedure. The faster dissolution regime might have required considerable amounts of U(V) and U(VI) to have formed on the pellet surface [28], as the stoichiometric oxide is relatively unreactive toward oxidants such as H_2O_2. However, fast onsets in dissolution were observed in the works of Kerleguer et al., and Odorowski et al., in which the MOX pellets were washed in carbonate solutions after the annealing process and prior to the leaching experiments [118, 128]. As the release rates in the washing steps were relatively high, it cannot be ruled out that the carbonate washing steps are not completely dissolving the oxidized uranium formed due to the extensive radiolysis occurring at the MOX-H_2O interface. This was observed in the external radiation experiments of the present work (Chapter 6.3), in which a lower oxidation state was found on the sputtered pellet, as compared to the pellets which were carbonate-washed prior to XPS measurement. This shows that the carbonate wash did not completely dissolve the oxidized surface layer.

Experiments labelled A and B were conducted with the 10 wt.% Pu-doped MOX pellets annealed in N_2 with 5% H_2. The uranium dissolution trends in these experiments show somewhat of a disparity. During the initial 40 days, the 10 wt.% Pu-doped pellet in experiment B had a significantly higher release rate than the pellet in experiment A. However, this disparity

became rather small toward the end of the experiments. No indication of corrosion products from the T316 stainless steel dip tube was found at the end of the Ar atmosphere experiments. Experiment C was conducted using a dip tube made of PEEK instead of T316 stainless steel. The pellet was annealed in 5% H_2 in Ar. The dissolution trend in experiment C was a lot less noisy, although this could have been influenced by the small number of sample points taken during the early stages of the experiment, which may have allowed less potential O_2 in-leakage. The fewer sample outtakes also led to a lower pressure drop. The concentrations in experiment C were also significantly lower than those found in the other 10 wt.% Pu-doped MOX experiments (Figure 6.23).

Plutonium concentrations were also measured using ICP-MS. With the exception of a few samples, the concentrations were below the ICP-MS measurement limit due to the very strong sorption of dissolved plutonium on the glass beaker surfaces. A desorption test was conducted at the end of experiment D, which found a total of $2.8 \cdot 10^{-8}$ moles Pu-239. This is three orders of magnitude below the level of dissolved uranium.

The 24 wt.% MOX pellet studied in experiments D and E were annealed in N_2 with 5% H_2. The release rate at the end of experiment D (using the 24 wt.% Pu-doped MOX pellet) is $(1.94 \pm 0.17) \cdot 10^{-6}$ $M \cdot d^{-1}$. This can be compared to experiment E, in which a release rate of $(2.37 \pm 0.12) \cdot 10^{-6}$ $M \cdot d^{-1}$ was found at the end of the experiment. However, significantly higher release rates were measured at the start of experiment E.

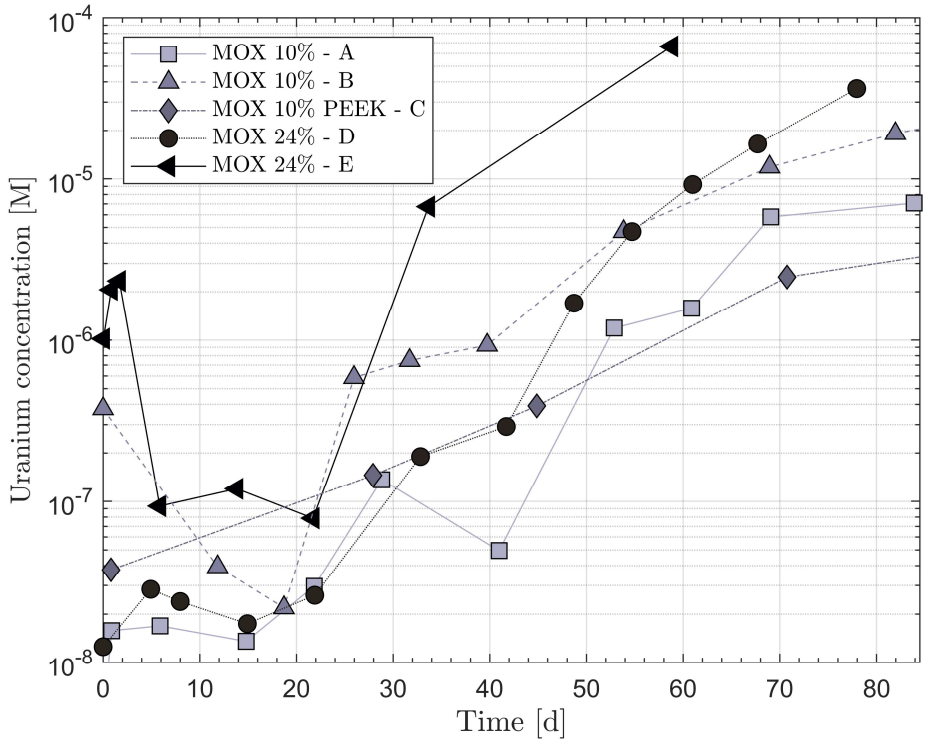

Figure 6.23. 10 and 24 wt.% Pu-doped leaching experiments under 10 bar initial pressure Ar atmosphere.

Toward the end of the 10 wt.% Pu-doped MOX pellet experiments, the release rates were significantly lower than at the end of the 24 wt.% Pu-doped ones. At the end of experiment B,

the release rate was $(5.61\pm0.78)\cdot10^{-7}$ $M\cdot d^{-1}$. This was lower than in the 24 wt.% Pu-doped experiments by a factor of approximately five (Figure 6.23). The release rate at the end of the 85-day period of experiment A was somewhat lower than in experiment B, of $(2.39\pm0.20)\cdot10^{-7}$ $M\cdot d^{-1}$, (calculated from the last three points, as these are highly nonlinear). Using the PEEK dip tube in experiment C, the release rate at the end of the 85 day period (shown in Figure 6.23) was considerably lower, of $(6.69\pm0.10)\cdot10^{-8}$ $M\cdot d^{-1}$. Experiment C however reached very similar release rates to experiments A and B somewhat later, around ~100 days. The higher release rates from the 24 wt.% Pu-doped pellets as compared to the 10 wt.% Pu-doped ones likely stemmed from the higher radiolytic production by a factor of three due to the higher α-activity. It should however be emphasized that the 24 wt.% Pu-doped pellet studied in this work had a rather low theoretical density, of 93%, which could contribute to the higher release rates. Kerleguer et al. studied 24 wt.% Pu-doped MOX with homogeneous microstructure. Their work found that the microstructure provided a stabilizing effect to the MOX matrix, as compared to leaching a 7.5 wt.% Pu-doped MOX pellet with a heterogeneous MIMAS microstructure [128]. This was because the homogeneously distributed PuO_2 had a significant stabilizing effect on the UO_2, which was not observed on the MOX pellets with heterogeneously distributed Pu [128].

Odorowski et al. studied the oxidative dissolution of a 7.5 wt.% Pu-doped pellet with a MIMAS MOX heterogeneous microstructure under air and Ar atmospheres [118]. A negligible influence of the air atmosphere was found compared to the Ar atmosphere. This indicated that the α-radiolytic production had a significantly higher contribution toward the oxidative dissolution than the O_2 from the air atmosphere. However, the MOX leaching experiments in the present work have found a high sensitivity toward O_2-contamination. Under H_2 atmosphere, even small leakages led to a significantly higher dissolution, showing that despite the rather large overpressures in the autoclaves during the experiments, counterdiffusion could not be neglected. In the work of Fors, the rate of counter diffusion through a slit or hole was derived, which was shown to be strongly influenced by the geometry of the opening [17]. The derivation shows that counterdiffusion is feasible, even across the rather large pressure gradients.

The large discrepancies during the early stages of dissolution in the present work might be due to variations related to sample preparation. The in-leakage of O_2 during experiments due to insufficient or uneven pressure on the graphite gaskets, or counterdiffusion during sampling might also have a notable influence.

6.6.3. MOX leaching under D_2 atmosphere

A dissolution experiment under 8 bar D_2 atmosphere using the 24 wt.% Pu-doped MOX pellet was conducted using a T316 stainless steel dip tube. The initial slow dissolution phase was even more pronounced than under the Ar atmosphere experiments. After approximately 80 days, a plateau of $4\cdot10^{-7}$ M was reached, which lasted until the end of the experiment. However, upon opening the autoclave, a visually apparent amber-colored precipitate was observed, matching the visual characteristics of Fe(III)-containing minerals, such as goethite or hematite [142]. The precipitate was not visually apparent in the samples taken through the dip tube during the experiment. The presence of this precipitate would explain the very low measured uranium concentrations, due to the strong adsorbing characteristic of Fe(III)-containing

minerals toward U(VI) [143]. The series may be seen in Appendix A, Figure A2. An additional experiment was conducted using a T316 stainless steel dip tube and the 24 wt.% Pu-doped pellet with 15 bar D_2 initial pressure, in which quite a rapid uranium release was initially measured due to a notable D_2 leakage. After this dissolution phase, the dissolved concentrations decreased significantly, resulting in concentrations below detection limit. The amber-colored rust precipitate was found when opening the autoclave at the end of the experiment, which explains the very low dissolved uranium concentrations. The data series is shown in Appendix A, Figure A.3. Both of these series were performed with annealing in 5% H_2 in N_2.

Due to the issues regarding the corroding dip tubes, the experiment was repeated using a PEEK dip tube with the 24 wt.% Pu-doped pellet under 10 bar D_2 atmosphere. The pellet was annealed in 5% H_2 in Ar. The dissolved uranium and D_2 concentrations using Henry's Law constant of $7.9 \cdot 10^{-6}$ $mol \cdot m^{-3} \cdot Pa^{-1}$ [144] are shown in Figure 6.24. The uranium release in the early stages of the experiment was slower than that observed during the Ar atmosphere experiments. A plateau at a concentration of $3 \cdot 10^{-5}$ M was reached after approximately 130 days, which was significantly higher than in the T316 stainless steel dip tube experiments under D_2 atmosphere. The dissolved uranium concentration plateaued before it reached the levels of the 24 wt.% Pu-doped pellet Ar atmosphere experiments, in which it went above $3 \cdot 10^{-5}$ M rather quickly. Between 79 and 127 days, the highest release rate was found to be $4.3 \cdot 10^{-7}$ $M \cdot d^{-1}$; approximately one order of magnitude lower than under Ar atmosphere. This was also found in Paper I, where an order of magnitude lower concentrations were found under D_2 atmosphere as compared to under Ar atmosphere. This shows an inhibiting effect of D_2 toward the oxidative dissolution by α-radiolysis. It should be mentioned that the hydrogen effect of D_2 might be weaker than of H_2 due to kinetic isotope effects [145].

At the end of the 10 bar D_2 PEEK experiment, a yellow precipitate was found on the pellet surface, matching the visual characteristics of schoepite. Thus, the steady-state concentration was due to equilibrium with the precipitated phase. However, the concentrations were somewhat lower than the solubilities of schoepite found in the literature [146]. The precipitated phase was difficult to analyze using XRD due to the curvature of the half-cylinder geometry of the MOX pellet. Therefore, this phase was not experimentally verified.

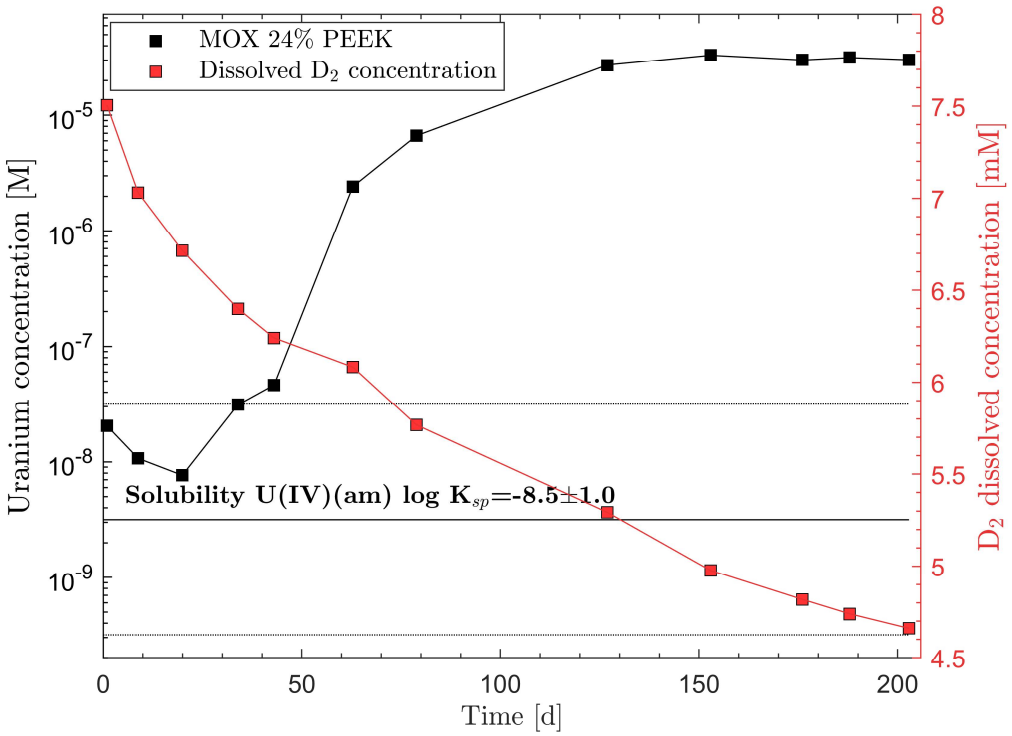

Figure 6.24. Leaching of the 24 wt.% Pu-doped MOX pellet under 10 bar initial D_2 pressure using a PEEK dip tube. The dissolved D_2 concentration is shown on the red y-axis.

6.6.4. H_2O_2 measurement

The Ghormley method was used to measure H_2O_2 concentrations in experiment C, where the small 10 wt.% Pu-doped MOX pellet was studied under 10 bar Ar atmosphere using a PEEK dip tube, and in the last sample of the 10 bar D_2 atmosphere PEEK dip tube experiment using the 24 wt.% Pu-doped MOX pellet. The concentrations are shown in Figure 6.25. The difference in radiolytic oxidant production between the two different doping levels of the MOX pellets is almost a factor of three ($1.24 \cdot 10^{-7}$ mol·d^{-1} compared to $3.67 \cdot 10^{-8}$ mol·d^{-1}). Given this fact, the D_2 atmosphere clearly had a suppressing effect, leading to a lower H_2O_2 concentration. No H_2O_2 concentrations were detected in the T316 stainless steel dip tube experiments, which showed that a significant consumption of H_2O_2 occurred on the corroding dip tube surfaces. The steady-state concentration found in the 10 wt.% Pu-doped MOX pellet experiment under 10 bar Ar atmosphere with a PEEK dip tube was $2.61 \cdot 10^{-5}$ M. The single data point from the last sample in the 10 bar D_2 PEEK experiment gave a concentration of $3.3 \cdot 10^{-6}$ M. The measured concentrations were in good agreement with the theoretical steady-state concentrations amounts modelled using the empirical relationships from Trummer and Jonsson [109], of $4.10 \cdot 10^{-5}$ M and $2.77 \cdot 10^{-6}$ M for the Ar and D_2 experiments respectively. It should be mentioned that the H_2 pressure was below the theoretically predicted critical H_2 concentration needed to suppress H_2O_2 in 2 mM HCO_3^- solution, as discussed by Trummer and Jonsson [109]. Caution should also be taken when analyzing a single data point.

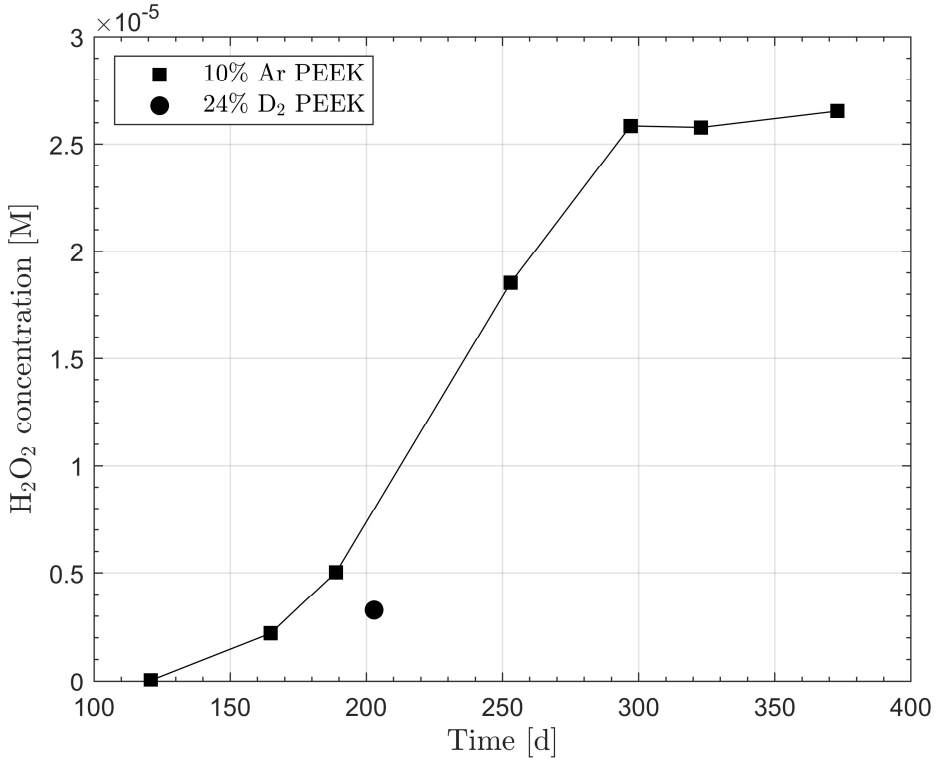

Figure 6.25. Ghormley method H_2O_2 concentration evolution of the 10% Ar PEEK and last data point of the 24% D_2 PEEK experiments.

6.6.5. MOX dissolution yields

Taking the solution volumes into account, volume-specific H_2O_2 production rates were modelled throughout the experiments using the stepwise isotropic emission model (described in Chapter 3.1). The dissolution yield, i.e., the ratio between the dissolved uranium concentration and radiolytically produced H_2O_2, is shown on the right-hand y-axis in Figure 6.26, with the dissolved uranium concentrations and modelled H_2O_2 concentrations on the left-hand y-axis. The first data point from the yields has been omitted due to measurable uranium concentrations giving incredibly high yields (compared to the almost zero theoretically produced H_2O_2 amounts). The yields were very low during the initial slow-release-rate phase, after which the yields increased quite significantly. This supports the notion that a considerable amount of U(V) or U(VI), or a combination of the two states, needs to be formed on the UO_2 surface before noticeable dissolution takes place. The maximum dissolution yield of 24% in the 10 bar D_2 experiment using the 24 wt.% Pu-doped MOX pellet is found between 127 – 153 days.

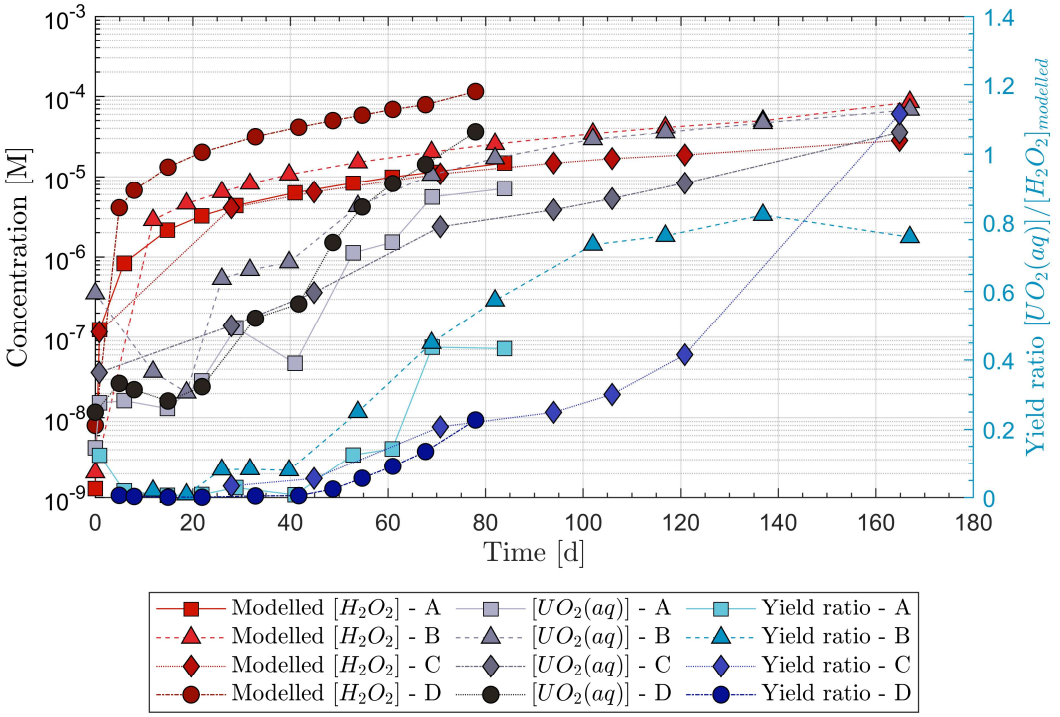

Figure 6.26. Comparison between modelled H_2O_2 concentration evolutions and measured uranium concentrations. The yield ratios are shown on the right-hand y-axis.

The modelled yields are significantly higher than the results found in Kerleguer et al., in which no measurable H_2O_2 concentrations were found using chemiluminescence with a detection limit of 10^{-7} M [128]. In that work, the resulting dissolution yields between the measured uranium concentrations and modelled H_2O_2 production rates were found to be less than 1%. The main explanation given by the authors was the homogeneous microstructure of the MOX pellet, which contributed to the catalytic decomposition of H_2O_2. Odorowski et al. studied a 7.5 wt.% Pu-doped MOX pellet with a MIMAS MOX heterogeneous microstructure and similar dose rate [118]. This pellet was very similar to the 10 wt.% Pu-doped MOX pellets studied in the present work. Very similar experimental conditions were also studied, with the exception of the solution being in contact with the TiO_2 autoclave surfaces in the works of Odorowski et al. and Kerleguer et al. [118, 128]. A resulting H_2O_2 concentration of almost $1.4 \cdot 10^{-6}$ M was measured by Odorowski et al. after ~400 days, which was ~20 times lower than the concentration measured in the present work. The only surface not included in the present work, but which could react with H_2O_2, is TiO_2. This was reported by Kerleguer et al. in a benchmark test to have consumed less than 1% of the H_2O_2 per day [128]. However, over a 400-day experiment, a consumption close to 1% per day may produce a notable influence. Additionally, the test by Kerleguer et al. was conducted at concentrations above their limit of detection (10^{-7} M), which might not be entirely valid for the lower concentrations under the MOX leaching experiment. Thus, the consumption on the TiO_2 surfaces might be non-negligible, and might explain the differences between the present work and that of Odorowski et al.

6.6.6. HDO analysis

The measured isotopic H/D ratio is expressed as HDO concentrations relative to SMOW. The 8 bar D_2 experiment using the 10 wt.% Pu-doped MOX pellet (Figure A.2), and 24 wt.% Pu-doped MOX pellet are shown alongside reference experiments in Figure 6.27. Reference experiments were conducted, using both T316 and PEEK dip tubes. An HDO data series from the SIMFUEL study (Paper II) is also shown, in which 2.5 mM H_2O_2 was added at the start of the experiment. The SIMFUEL experiment was shown to have increased HDO production due to the catalytic decomposition of H_2O_2 under D_2 atmosphere (further details may be found in Paper II). All other data series correspond very well, with the exception of an early data point after ~9 days in the 10 bar D_2 experiment using the 24 wt.% Pu-doped pellet.

The HDO data series from the 10 bar D_2 experiment using 10 wt.% Pu-doped MOX (Figure 6.24) was omitted due to the concentrations being significantly lower than those shown in the other data series. The only difference between this experiment and the others was the annealing process. This was carried out under 5% H_2 in Ar , as compared to the other two pellets which were annealed under 5% H_2 in N_2. It however seems unlikely that the differing annealing processes would cause significant decomposition of the formed HDO.

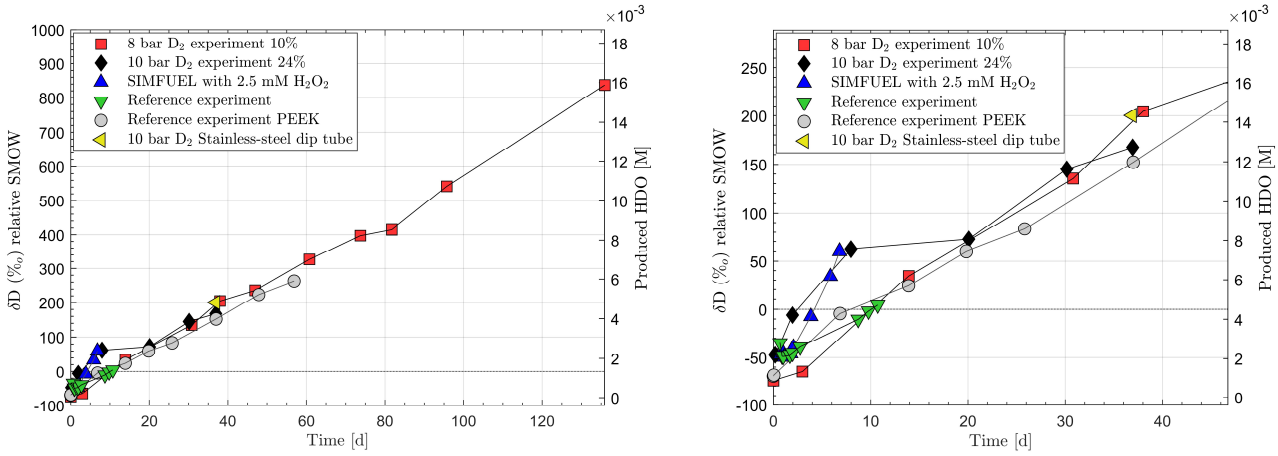

Figure 6.27. HDO concentrations throughout the D_2 experiments, including reference experiments and data from the SIMFUEL study, in which 2.5 mM H_2O_2 was initially added. The data during the early stages may be seen more clearly in the right-hand figure, in which the first 50 days are magnified.

The results show that the formation of HDO in the MOX leaching experiments is likely purely due to isotopic exchange on the surfaces present in the system, and does not give further information about the H_2 effect in the presence of a MOX pellet surface (as was hypothesized in Paper I).

6.7. Kinetic modelling (Papers V and VIII)

The combined radiolytic production, kinetic and diffusion model (described in Chapter 3.1) was optimized for spatial and temporal resolutions. The model was benchmarked by reproducing a Fricke-dosimeter and modelling the G-value of Fe^{3+} from Fe^{2+} in an irradiated solution. This gave results identical to the theoretically predicted value. Further details about the spatial and temporal settings optimization and benchmarking may be found in Paper V.

6.7.1. Surface site reaction system

Using the experimental data from Barreiro Fidalgo et al. [80], the surface site reaction system with the rate constants ks1, ks2, ks3 (described by Eq.(7)–(9) in Table 2.2) and ks4 (Eq.(21)) was fitted. The MATLAB function, lsqnonlin, was used to output the residual sum of squares between the experimental data and the modelled reaction system. This was minimized through iterations over the rate constants. Stoichiometric UO_2 at t=0 was used in the model. The experimental data series with 0.2, 0.5, 1.0 and 2.0 mM initial H_2O_2 concentrations were fitted individually as well as simultaneously. In the simultaneous fit of the rate constants, a weight factor was used to normalize the weights of the individual data series. The specific surface-to-volume ratio, S/V=5400 m^{-1} from Barreiro Fidalgo et al.'s experiments [80] was used to convert the surface site area density into concentrations in the innermost solution layer.

The fitted rate constants for the individual concentration series and full (simultaneous) system fit are shown in Table 6.4. The rate constants fitted to the different individual data series are in quite good agreement with each other. The fits are insensitive to the value of ks4, which may vary by an order of magnitude without any significant influence on the dissolution rates or residual values of the fit. This means that the oxidation of U(IV) to U(V) is the rate-determining step, after which dissolution occurs quickly, as would be expected in a carbonate-rich solution. This corresponds well with the results of Ekeroth et al., which showed that the rate-determining step is the one-electron transfer between H_2O_2 and UO_2 [131].

Table 6.4. Fitted rate constants to the OH·(ads) surface reaction system.

$[H_2O_2]_0$	ks1 ($M^{-1}\cdot s^{-1}$)	ks2 (s^{-1})	ks3 ($M^{-1}\cdot s^{-1}$)	ks4 ($M^{-1}\cdot s^{-1}$)
0.2 mM	$8.66\cdot10^{-1}$	$5.48\cdot10^{-1}$	$1.06\cdot10^{2}$	$1.41\cdot10^{1}$
0.5 mM	$5.03\cdot10^{-1}$	$2.25\cdot10^{-1}$	$1.76\cdot10^{2}$	$2.23\cdot10^{1}$
1.0 mM	$3.50\cdot10^{-1}$	$2.09\cdot10^{-1}$	$1.86\cdot10^{2}$	$2.21\cdot10^{1}$
2.0 mM	$2.33\cdot10^{-1}$	$2.49\cdot10^{-1}$	$1.96\cdot10^{2}$	$2.42\cdot10^{1}$
Full system	$4.62\cdot10^{-1}$	$1.91\cdot10^{-1}$	$1.97\cdot10^{2}$	$3.41\cdot10^{1}$

The individual data series fit with 0.2 mM initial H_2O_2 concentration is shown in Figure 6.28, and the weighted full system fit is shown in Figure 6.29. The constants in the full system fit can describe all data series quite accurately and will therefore be used to describe the surface site reaction system henceforth.

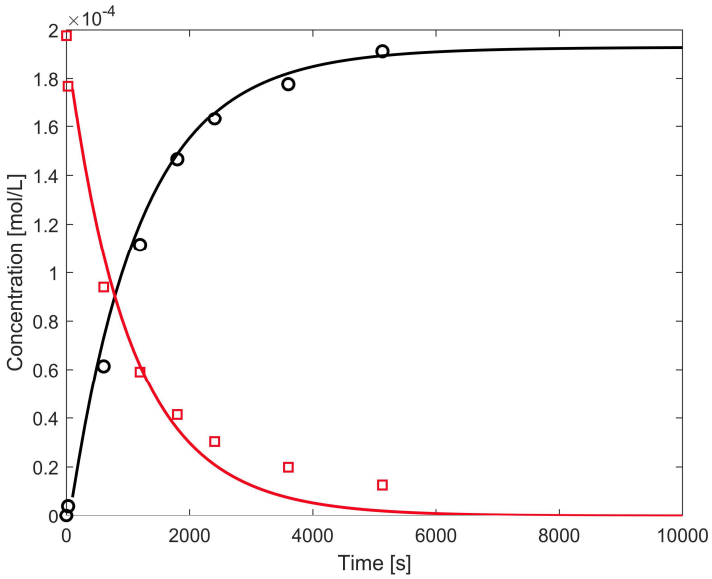

Figure 6.28. Individual data series fit of the 0.2 mM initial H_2O_2 concentration of the Barreiro Fidalgo data, with stoichiometric UO_2 at t=0 with the constants ks1, ks2, ks3 and ks4 shown in Table 6.4.

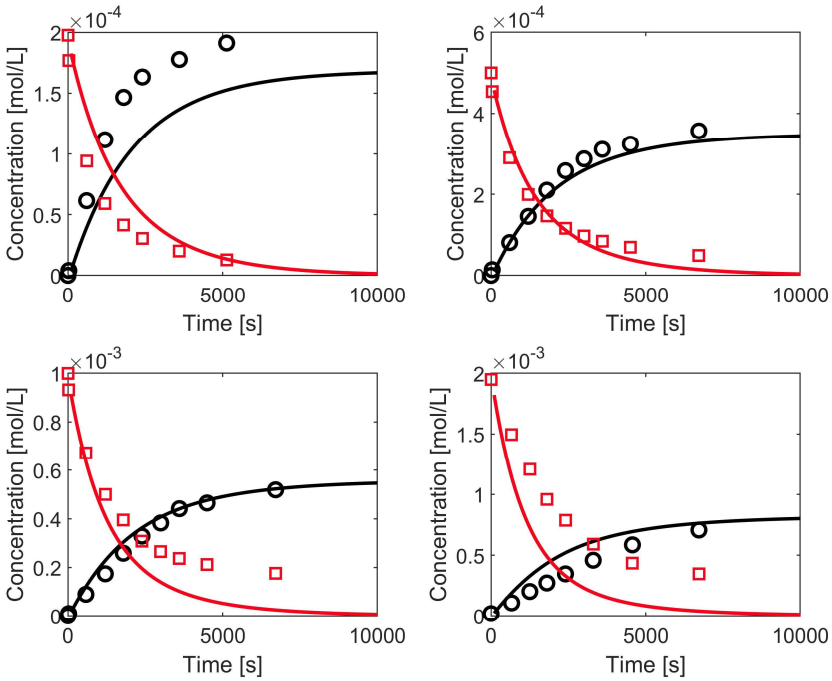

Figure 6.29. Full system fit of the Barreiro Fidalgo data [80], with stoichiometric UO_2 at t=0 with the constants ks1, ks2, ks3 and ks4 shown in Table 6.4.

6.7.2. Modelling of MOX pellet leaching

The oxidative dissolution of the 10 and 24 wt.% Pu-doped MOX pellets can be modelled using the fitted surface site reaction system (with rate constants ks1, ks2, ks3, described by Eq.(7)–(9) in Table 2.2, and ks4) and the rate constant from Hossain et al. [107]. However, as the matrix consists of up to 24 wt.% Pu, the Hossain rate constant and fitted surface reaction system

might not be perfectly applicable. This is because the matrix has a considerable PuO_2 component which behaves quite differently toward H_2O_2 than UO_2.

The MOX leaching system was generalized in the modeling through homogenization, as diffusion plays a rather insignificant role in the rather tiny closed system over long timescales. (See Paper V for further details.) Additionally, the sampling introduces advection to the system, which affects the mass transfer. The S/V ratios for the experiments were calculated by considering the average solution volume throughout the experiment. The S/V ratios were in the range of 0.6 – 1.6 m^{-1}, which was very low compared to the value of 5400 m^{-1} in the work of Barreiro Fidalgo et al. that was used in the fit for the surface site reaction system. As the surface area was scaled down by the smaller S/V ratio, the oxidation from U(V) to U(VI) followed by dissolution became significantly slower due to a rate dependence of reaction Eq.(21) with rate constant ks4. This is due to the square dependence of the S/V ratio in reaction (21), leading to accumulation of U(V). The value of ks4 was therefore scaled by the difference in S/V ratio between the two systems.

Modelling the 24 wt.% Pu-doped pellet under Ar atmosphere, the resulting H_2O_2 concentrations after 373 days (corresponding to the time of the last data point in the Ghormley measurement of experiment C, Figure 6.25) were $7.96 \cdot 10^{-5}$ M, using the fitted surface site reaction system, and $9.20 \cdot 10^{-5}$ using the Hossain et al. reaction constant (solid and dashed lines respectively in Figure 6.30). After 78 days (corresponding to the last data point in experiment series D using the 24 wt.% Pu-doped MOX pellet, Figure 6.23), the modelled uranium concentrations were $2.93 \cdot 10^{-5}$ and $2.10 \cdot 10^{-5}$ M using the fitted surface site reaction system and the Hossain et al. reaction constant respectively. The surface site reaction system described the dissolution of experiment series D somewhat accurately which, at that point, had a dissolved uranium concentration of $3.64 \cdot 10^{-5}$ M (Figure 6.23).

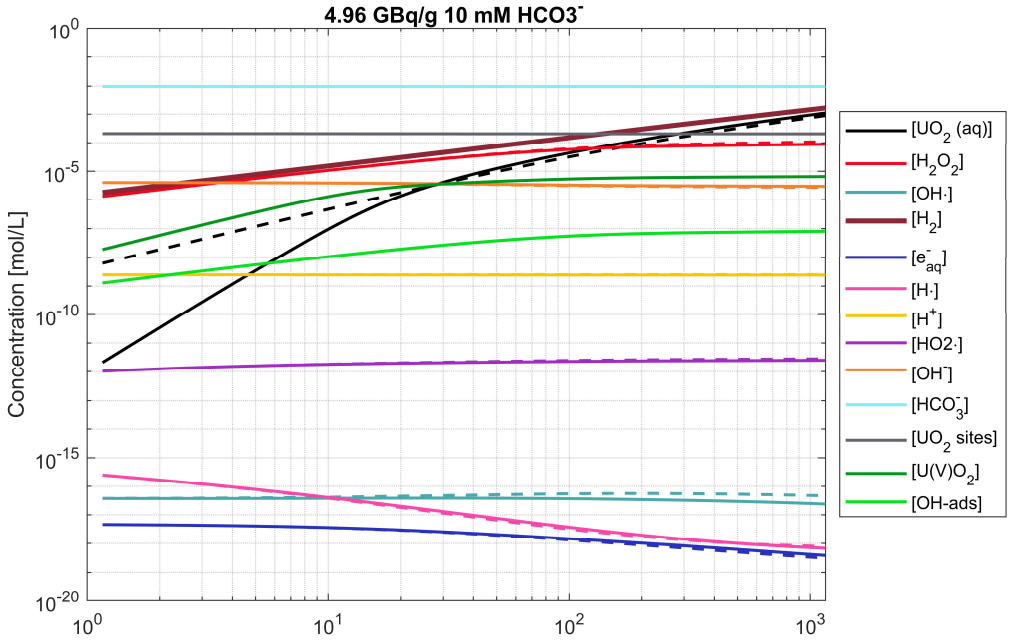

Figure 6.30. Modelled dissolution of experiment D of the 24 wt.% Pu-doped MOX pellet using the Hossain et al. dissolution rate constant and the fitted surface site reaction system.

Modelling the small 10 wt.% Pu-doped pellet under Ar atmosphere (experiment C), the resulting H_2O_2 concentrations after 373 days were $2.55 \cdot 10^{-5}$ M using the fitted surface site reaction system, and $2.72 \cdot 10^{-5}$ M using the Hossain et al., reaction constant (solid and dashed lines respectively, Figure 6.31). This corresponded very well with the steady-state concentration of $2.61 \cdot 10^{-5}$ M, measured using the Ghormley method (Figure 6.25). After 71 days, the modelled uranium concentrations were $1.33 \cdot 10^{-6}$ M and $1.53 \cdot 10^{-6}$ M using the fitted surface site reaction system, and Hossain et al. constant respectively. Comparing this to the experimentally measured value of $2.47 \cdot 10^{-6}$ M, the dissolution is described quite accurately. Thus, the MIMAS MOX heterogeneous microstructure seems to be described quite accurately as dissolution of UO_2.

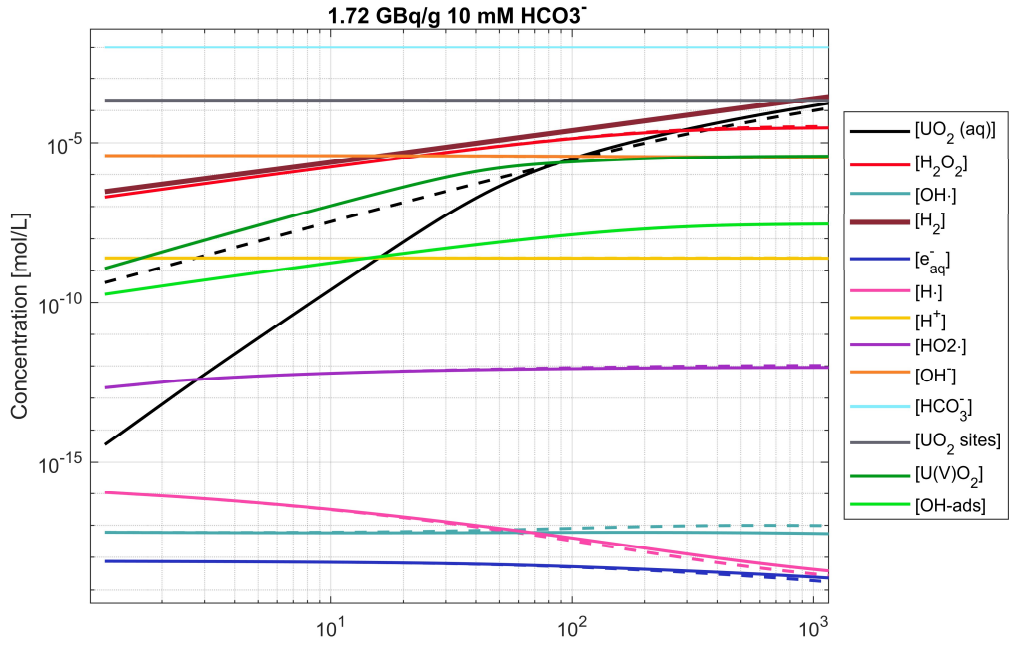

Figure 6.31. Modelled dissolution of experiment C using the PEEK dip tube and the 10 wt.% Pu-doped MOX pellet with the Hossain et al. dissolution rate constant (dashed lines) and the fitted surface site reaction system (solid lines).

6.7.3. The effect of H_2

H_2 can reduce H_2O_2 concentrations under an α-radiation field through reactions with the radicals formed as radiolysis products, as shown in the reaction table in Appendix B (Table S.1). However, this effect was found to be rather weak, amounting to less than a 10% decrease in uranium dissolution when modelling the 24 wt.% Pu-doped MOX pellet under 10 bar H_2 atmosphere for 100 days.

In order to describe the effect of H_2, the reaction between H_2 and the surface adsorbed ·OH, the reaction rate, ks6, was fitted. In order to decrease the release rate of the 24 wt.% Pu-doped MOX by an order of magnitude as was found in the experimental results, a value of ks6 = 20 $M^{-1} \cdot s^{-1}$ was found. In order to fit the data of the external irradiation experiments of UO_2 using the Am-241 sources, a value of ks6 = $2 \cdot 10^2$ $M^{-1} \cdot s^{-1}$ was fitted. Quite a large spread in the effect of H_2 (in the absence of ε-particles) has been found in previous studies, from rather weak effects to a complete suppression of UO_2 dissolution [147]. The value of ks6 therefore has a very high uncertainty.

As the dissolution of U(VI) in the presence of HCO_3^- is expected to be very fast, ks5 (Eq.(22)) was set to diffusion controlled, meaning ks5 = 10^3 $M^{-1}\cdot s^{-1}$. Using this value, the reaction rate between H_2 and ε-particles, ks7, was conservatively estimated as 10^2 $M^{-1}\cdot s^{-1}$, based on the experimental data of Trummer et al. [111]. Using this value, modelling a high dose rate of 10 $kGy\cdot h^{-1}$ with an ε-particle surface coverage of 1%, the dissolution was already suppressed with a H_2 pressure of 1.4 bar using ks6 = 0, and 1.2 bar with ks6 = 10^2 $M^{-1}\cdot s^{-1}$. Therefore, the reaction between the surface adsorbed OH· radical and H_2 has a considerably weaker effect on the oxidative dissolution than the reaction between the ε-particles and H_2. The rather low H_2 pressures required to suppress dissolution show that under water intrusion conditions, the SNF will remain reduced in the U(IV) state by a wide margin. This is due to the fact that the value of ks7, the ε-particle coverage, and H_2 pressure will all exceed the values used in this modelling. Further details may be found in Paper VIII.

7. Summary and Conclusion

The KBS-3 concept could solve the spent nuclear fuel disposal issue. The concept entails encapsulating the spent nuclear fuel in copper canisters buried in crystalline bedrock at a depth of 500 m. The safety assessment of such a repository involves predicting the chemical behavior of the fuel in contact with groundwater.

The H_2 atmosphere (produced under anoxic conditions in the repository from iron corrosion) had a significant inhibiting effect on the radiolytic oxidation of UO_2 pellets irradiated by exposing a 30 µm water layer between the pellet surface and Am-241 sources. The H_2 atmosphere inhibited both the surface oxidation and the release into solution of uranium from the surface. Dissolved uranium concentrations one order of magnitude lower were found in the 11 and 45-day exposure experiments with both MQ and $NaHCO_3$-solutions under the H_2 atmosphere, as compared to under the Ar atmosphere. Exposure to the 1.85 MBq Am-241 source showed negligible oxidation under both atmospheres. The analysis of the valence band region showed decreased intensity and a smaller FWHM of the U5f peak, which indicates a significant U(V) component. The results show that the oxidation of U(IV) occurs through the formation of a significant U(V) component, and does not form a mixed U(IV) and U(VI) oxidation state.

The presence of D_2 in the MOX leaching experiments inhibited the dissolution rate somewhat as compared to under Ar atmosphere, but could not suppress it completely. Except for an initial stage, the HDO production was not notably increased in the MOX fuel leaching studies under D_2 atmosphere. SIMFUEL containing ε-particles was shown to be very resistant towards oxidative dissolution under D_2 atmosphere and high initial H_2O_2 concentrations. The strength of the H_2 effect is therefore highly dependent on the experimental conditions.

The presence of corroding iron foils in synthetic groundwater solutions containing 1 ppm uranyl caused efficient reductive precipitation, decreasing dissolved uranium concentrations by up to three orders of magnitude. The formation of the calcium-uranyl-carbonato complexes could to a small extent slow down the reductive precipitation. However, this kinetic effect is insignificant under deep geological conditions, due to the immense relevant timescales.

The fitted surface site reaction system can explain the experimental data observed in several studies, and account for the formation of U(V) and surface-adsorbed ·OH. The fitted system gives uranium dissolution rates in quite good agreement with the Hossain et al. rate constant, which was expected, as the same process is described with varying degrees of complexity. The H_2O_2 and dissolved uranium concentrations in the MOX experiments were quite accurately modelled using the surface site reaction system. The modelled rate constants in the H_2-surface site reaction system with ε-particles indicate that that the SNF will remain reduced under a water intrusion scenario.

The combined effects of iron and H_2 will therefore ensure that the fuel will remain reduced in the scenario of water intrusion. Additionally, if oxidation would occur, the corroding iron will efficiently reductively precipitate the uranium, which contributes to the safety of the repository under such conditions.

8. Future work

The influence of corroding iron on the dissolution of MOX would give further information about this effect under a very strong radiation field over extended periods. The influence of groundwater composition on the H_2 effect in MOX leaching experiments could also give valuable information. Higher H_2 pressures would be very important to study, as the pressures experimentally studied in this work are too low to accurately represent repository conditions. These studies should be combined with further surface characterization, such as XRD and SEM.

Further characterization of corroding iron foils in leaching experiments using e.g. XRD or EXAFS would give important information for the mechanism behind the reductive precipitation of uranium. This would not only further the understanding of uranium under repository conditions, but also of uranium behavior in environmental systems in general.

Experiments conducted to optimize the data used for describing the surface site reaction system would be very useful. An important step would be an accurate description of the formation of U(V), which requires dissolution in water without carbonate, combined with XPS analysis. The surface site system could further be used to explain other reactions occurring at the UO_2-H_2O interface in the presence of radiolytic oxidants.

Acknowledgements

I would like to start by thanking Kastriot, Christian, Mats, Lovisa, Eric, Marcus, and Stellan for very valuable and insightful discussions regarding the work. Without all your interesting and insightful feedback, the work would never have succeeded. You have all shown to be fantastic people in general, and I've very much enjoyed working with you. Special thanks to Lovisa and Artem for teaching me so much about the topic of nuclear chemistry and giving me the necessary knowledge to be able to continue on this interesting project.

A big thanks to all my funny, wonderful, eccentric, and friendly colleagues who have made breaks, fikas, lunches, after-work gatherings, parties and time spent at Chalmers great. I would not have survived without you :) May there forever be stray Arnolds around the department.

An extra thanks to Marcus and Thea for being amazing office mates who have always been open to discussions about anything, and have made the office such a fun and interesting place to be.

Thanks to all my amazing friends, for listening to my rants about nuclear, supporting me in so many ways, and for having a great sense of humor. Atomkraft? Ja bitte!

An enormous thanks to my very supportive and loving mom, dad, and brother. Without you, I would not have gotten anywhere in life.

Special thanks to my cat Majken who has kept me company when writing late at night.

All my love to my wonderful wife Olivia who has supported and motivated me through this challenging period, and to Agnes who is my biggest ray of sunshine. I'm very lucky to have you.

The Swedish Nuclear Fuel and Waste Management Company, SKB, is gratefully acknowledged for its funding of this project.

References

[1] IEA, Electricity Market Report - January 2022, (2022).

[2] IEA, Key World Energy Statistics 2021, International Energy Agency, (2021).

[3] IEA, Nuclear Power in a Clean Energy System, International Energy Agency, (2019).

[4] Birkholzer, J., Houseworth, J., Tsang, C.-F., Geologic disposal of high-level radioactive waste: Status, key issues, and trends, Annual Review of Environment and Resources, 37 (2012) 79-106. https://doi.org/10.1146/annurev-environ-090611-143314

[5] Steg, L., Limiting climate change requires research on climate action, Nature Climate Change, 8 (2018) 759-761. https://doi.org/10.1038/s41558-018-0269-8

[6] Marcus, G.H., Nuclear power around the world, Nature Reviews Physics, 1 (2019) 172. https://doi.org/10.1038/s42254-019-0020-z

[7] IAEA, The Power Reactor Information System (PRIS) and its extension to non-electrical applications, decommissioning and delayed projects information e technical reports series no. 428, International Atomic Energy Agency, 2005, accessed 26 April 2022, http:// www-pub.iaea.org/MTCD/Publications/PDF/TRS428_web.pdf.

[8] Aaltonen, I., Engström, J., Gehör, S., Kosunen, P., Kärki, A., Paananen, M., Paulamäki, S., Mattila, J.A., Geology of Olkiluoto, Posiva Report, 2016-16 (2016).

[9] Svensk Kärnbränslehantering AB, Technical Report TR-11-01 - Long-term safety for the final repository for spent nuclear fuel at Forsmark, (2011).

[10] Ewing, R.C., Weber, W.J., Clinard Jr, F.W., Radiation effects in nuclear waste forms for high-level radioactive waste, Progress in nuclear energy, 29 (1995) 63-127. https://doi.org/10.1016/0149-1970(94)00016-Y

[11] Grenthe, I., Drożdżyński, J., Fujino, T., Buck, E.C., Albrecht-Schmitt, T.E., Wolf, S.F., Uranium, in: The chemistry of the actinide and transactinide elements, Springer, 2008, pp. 253-698. https://doi.org/10.1007/1-4020-3598-5_5

[12] Hammond, C., The elements, Handbook of chemistry and physics, 81 (2000).

[13] Hazen, R.M., Ewing, R.C., Sverjensky, D.A., Evolution of uranium and thorium minerals, Am. Mineral., 94 (2009) 1293-1311. https://doi.org/10.2138/am.2009.3208

[14] Choppin, G., Liljenzin, J.-O., Rydberg, J., Ekberg, C., Chapter 14 - The Actinide and Transactinide Elements, in: Radiochemistry and Nuclear Chemistry (Fourth Edition), Academic Press, Oxford, 2013, pp. 405-444. https://doi.org/10.1016/B978-0-12-405897-2.00014-8

[15] Holden, N., Isotopic composition of the elements and their variation in nature: a preliminary report, in, Brookhaven National Lab., 1977.

[16] Kutty, T., Hegde, P., Khan, K., Basak, U., Pillai, S., Sengupta, A., Jain, G., Majumdar, S., Kamath, H., Purushotham, D., Densification behaviour of UO2 in six different atmospheres, J. Nucl. Mater., 305 (2002) 159-168. https://doi.org/10.1016/S0022-3115(02)00934-0

[17] Fors, P., The effect of dissolved hydrogen on spent nuclear fuel corrosion, Chalmers University of Technology, 2009. http://dx.doi.org/10.13140/RG.2.1.5125.4244

[18] Choppin, G., Liljenzin, J.-O., Rydberg, J., Ekberg, C., Chapter 21 - The Nuclear Fuel Cycle, in: Radiochemistry and Nuclear Chemistry (Fourth Edition), Academic Press, Oxford, 2013, pp. 685-751. https://doi.org/10.1016/B978-0-12-405897-2.00021-5

[19] Kessler, G., Uranium Enrichment, in: Sustainable and Safe Nuclear Fission Energy, Springer, 2012, pp. 59-71. https://doi.org/10.1007/978-3-642-11990-3_4

[20] Diven, B., Martin, H., Taschek, R., Terrell, J., Multiplicities of fission neutrons, Physical Review, 101 (1956) 1012. https://doi.org/10.1103/PhysRev.101.1012

[21] Choppin, G., Liljenzin, J.-O., Rydberg, J., Ekberg, C., Chapter 17 - Production of Radionuclides, in: Radiochemistry and Nuclear Chemistry (Fourth Edition), Academic Press, Oxford, 2013, pp. 513-544. https://doi.org/10.1016/B978-0-12-405897-2.00017-3

[22] Seaborg, G.T., Mcmillan, E.M., Kennedy, J.W., Wahl, A., Radioactive element 94 from deuterons on uranium, Physical Review, 69 (1946) 366. https://doi.org/10.1103/PhysRev.69.366.2

[23] Clark, D.L., Hecker, S.S., Jarvinen, G.D., Neu, M.P., Plutonium, in: The chemistry of the actinide and transactinide elements, Springer, 2008, pp. 813-1264. https://doi.org/10.1007/1-4020-3598-5_7

[24] Ewing, R.C., Long-term storage of spent nuclear fuel, Nature Materials, 14 (2015) 252-257. https://doi.org/10.1038/nmat4226

[25] Bruno, J., Ewing, R.C., Spent nuclear fuel, Elements, 2 (2006) 343-349. https://doi.org/10.2113/gselements.2.6.343

[26] Holm, M., RadTox, a computer program for assessing radiotoxicity curves for used nuclear fuel., Chalmers University of Technology, Department of Nuclear Chemistry, Master's thesis, (2011).

[27] George, K., Masters, A.J., Livens, F.R., Sarsfield, M.J., Taylor, R.J., Sharrad, C.A., A review of technetium and zirconium extraction into tributyl phosphate in the PUREX process, Hydrometallurgy, (2022) 105892. https://doi.org/10.1016/j.hydromet.2022.105892

[28] Shoesmith, D., Fuel corrosion processes under waste disposal conditions, J. Nucl. Mater., 282 (2000) 1-31. https://doi.org/10.1016/S0022-3115(00)00392-5

[29] Kleykamp, H., The solubility of selected fission products in UO 2 and (U, Pu) O 2, J. Nucl. Mater., 206 (1993) 82-86. https://doi.org/10.1016/0022-3115(93)90236-R

[30] Johnson, L., Ferry, C., Poinssot, C., Lovera, P., Spent fuel radionuclide source-term model for assessing spent fuel performance in geological disposal. Part I: Assessment of the instant release fraction, J. Nucl. Mater., 346 (2005) 56-65.

[31] Näslund, J.-O., Brandefelt, J., Liljedahl, L.C., Climate considerations in long-term safety assessments for nuclear waste repositories, Ambio, 42 (2013) 393-401.

[32] Brookins, D., Radionuclide behavior at the Oklo nuclear reactor, Gabon, Waste Manage. (Oxford), 10 (1990) 285-296. https://doi.org/10.1016/0956-053X(90)90102-Q

[33] Rosborg, B., Werme, L., The Swedish nuclear waste program and the long-term corrosion behaviour of copper, J. Nucl. Mater., 379 (2008) 142-153. https://doi.org/10.1016/j.jnucmat.2008.06.025

[34] King, F., Ahonen, L., Taxén, C., Vuorinen, U., Werme, L., Copper corrosion under expected conditions in a deep geologic repository, in, Swedish Nuclear Fuel and Waste Management Co., 2001.

[35] Puigdomenech, I., Ambrosi, J., Eisenlohr, L., Lartigue, J., Banwart, S., Bateman, K., Milodowski, A., West, J., Griffault, L., Gustafsson, E., O2 depletion in granitic media. The Rex project, in, Swedish Nuclear Fuel and Waste Management Co., 2001.

[36] Swedish Ministry of the Environment, Final disposal of spent nuclear fuel, 2022, accessed 26 April 2022, https://www.government.se/articles/2022/01/final-disposal-of-spent-nuclear-fuel/.

[37] Choppin, G., Liljenzin, J.-O., Rydberg, J., Ekberg, C., Chapter 5 - Unstable Nuclei and Radioactive Decay, in: Radiochemistry and Nuclear Chemistry (Fourth Edition), Academic Press, Oxford, 2013, pp. 85-123. https://doi.org/10.1016/B978-0-12-405897-2.00005-7

[38] Choppin, G., Liljenzin, J.-O., Rydberg, J., Ekberg, C., Chapter 8 - Radiation Effects on Matter, in: Radiochemistry and Nuclear Chemistry (Fourth Edition), Academic Press, Oxford, 2013, pp. 209-237. https://doi.org/10.1016/B978-0-12-405897-2.00008-2

[39] Pastina, B., LaVerne, J.A., Effect of molecular hydrogen on hydrogen peroxide in water radiolysis, J. Phys. Chem. A, 105 (2001) 9316-9322. https://doi.org/10.1021/jp012245j

[40] Elliot, A.J., McCracken, D.R., Computer modelling of the radiolysis in an aqueous lithium salt blanket: Suppression of radiolysis by addition of hydrogen, Fusion Eng. Des., 13 (1990) 21-27. https://doi.org/10.1016/0920-3796(90)90028-5

[41] Pastina, B., LaVerne, J.A., Hydrogen peroxide production in the radiolysis of water with heavy ions, J. Phys. Chem. A, 103 (1999) 1592-1597. https://doi.org/10.1021/jp984433o

[42] Schwarz, H.A., Caffrey Jr, J.M., Scholes, G., Radiolysis of Neutral Water by Cyclotron Produced Deuterons and Helium Ions1, Journal of the American Chemical Society, 81 (1959) 1801-1809. https://doi.org/10.1021/ja01517a008

[43] LaVerne, J.A., Schuler, R.H., Burns, W., Track effects in radiation chemistry: production of hydroperoxo radical within the track core in the heavy-particle radiolysis of water, J. Phys. Chem., 90 (1986) 3238-3242. https://doi.org/10.1021/j100405a037

[44] LaVerne, J.A., The production of OH radicals in the radiolysis of water with ^{4}He ions, Radiat. Res., 118 (1989) 201-210. https://doi.org/10.2307/3577437

[45] LaVerne, J.A., Yoshida, H., Production of the hydrated electron in the radiolysis of water with helium ions, J. Phys. Chem., 97 (1993) 10720-10724. https://doi.org/10.1021/j100143a033

[46] LaVerne, J.A., Pimblott, S., New mechanism for H2 formation in water, J. Phys. Chem. A, 104 (2000) 9820-9822. https://doi.org/10.1021/jp002893n

[47] Neck, V., Kim, J., Solubility and hydrolysis of tetravalent actinides, Radiochimica Acta, 89 (2001) 1-16.

[48] Sunder, S., Miller, N., Shoesmith, D., Corrosion of uranium dioxide in hydrogen peroxide solutions, Corros. Sci., 46 (2004) 1095-1111.

[49] Ekeroth, E., Roth, O., Jonsson, M., The relative impact of radiolysis products in radiation induced oxidative dissolution of UO2, J. Nucl. Mater., 355 (2006) 38-46. https://doi.org/10.1016/j.jnucmat.2006.04.001

[50] Ilton, E.S., Pacheco, J.S.L., Bargar, J.R., Shi, Z., Liu, J., Kovarik, L., Engelhard, M.H., Felmy, A.R., Reduction of U (VI) incorporated in the structure of hematite, Environ. Sci. Technol., 46 (2012) 9428-9436. https://doi.org/10.1021/es3015502

[51] Ilton, E.S., Haiduc, A., Cahill, C.L., Felmy, A.R., Mica surfaces stabilize pentavalent uranium, Inorg. Chem., 44 (2005) 2986-2988.

[52] Santos, B., Nesbitt, H., Noel, J., Shoesmith, D., X-ray photoelectron spectroscopy study of anodically oxidized SIMFUEL surfaces, Electrochim. Acta, 49 (2004) 1863-1873. https://doi.org/10.1016/j.electacta.2003.12.016

[53] Santos, B., Noël, J., Shoesmith, D., The effect of pH on the anodic dissolution of SIMFUEL (UO2), J. Electroanal. Chem., 586 (2006) 1-11. https://doi.org/10.1016/j.jelechem.2005.09.021

[54] Ulrich, K.-U., Ilton, E.S., Veeramani, H., Sharp, J.O., Bernier-Latmani, R., Schofield, E.J., Bargar, J.R., Giammar, D.E., Comparative dissolution kinetics of biogenic and chemogenic uraninite under oxidizing conditions in the presence of carbonate, Geochim. Cosmochim. Acta, 73 (2009) 6065-6083. https://doi.org/10.1016/j.gca.2009.07.012

[55] Grossmann, K., Arnold, T., Steudtner, R., Weiss, S., Bernhard, G., Visualizing different uranium oxidation states during the surface alteration of uraninite and uranium tetrachloride, Naturwissenschaften, 96 (2009) 963-974. https://doi.org/10.1007/s00114-009-0558-1

[56] Leinders, G., Bes, R., Pakarinen, J., Kvashnina, K., Verwerft, M., Evolution of the uranium chemical state in mixed-valence oxides, Inorg. Chem., 56 (2017) 6784-6787.

[57] Kvashnina, K., Butorin, S.M., Martin, P., Glatzel, P., Chemical state of complex uranium oxides, Phys. Rev. Lett., 111 (2013) 253002.

[58] Sunder, S., Boyer, G.D., Miller, N.H., XPS Studies of UO2 oxidation by alpha radiolysis of water at 100°C, J. Nucl. Mater., 175 (1990) 163-169. https://doi.org/10.1016/0022-3115(90)90201-W

[59] Song, K.W., Kim, K.S., Kim, Y.M., Jung, Y.H., Sintering of mixed UO2 and U3O8 powder compacts, J. Nucl. Mater., 277 (2000) 123-129.

[60] Bonin, B., Colin, M., Dutfoy, A., Pressure building during the early stages of gas production in a radioactive waste repository, J. Nucl. Mater., 281 (2000) 1-14. https://doi.org/10.1016/S0022-3115(00)00184-7

[61] Scott, T., Allen, G., Heard, P., Randell, M., Reduction of U (VI) to U (IV) on the surface of magnetite, Geochim. Cosmochim. Acta, 69 (2005) 5639-5646. https://doi.org/10.1016/j.gca.2005.07.003

[62] Spahiu, K., Eklund, U.-B., Cui, D., Lundström, M., The influence of near field redox conditions on spent fuel leaching, Mater. Res. Soc. Symp. Proc., 713 (2001) 1-6. https://doi.org/10.1557/PROC-713-JJ14.5

[63] Ekeroth, E., Granfors, M., Schild, D., Spahiu, K., The effect of temperature and fuel surface area on spent nuclear fuel dissolution kinetics under H2 atmosphere, J. Nucl. Mater., 531 (2020) 151981. https://doi.org/10.1016/j.jnucmat.2019.151981

[64] Puranen, A., Barreiro, A., Evins, L.-Z., Spahiu, K., Spent fuel corrosion and the impact of iron corrosion–The effects of hydrogen generation and formation of iron corrosion

products, J. Nucl. Mater., 542 (2020) 152423. https://doi.org/10.1016/j.jnucmat.2020.152423

[65] Odorowski, M., Jegou, C., De Windt, L., Broudic, V., Jouan, G., Peuget, S., Martin, C., Effect of metallic iron on the oxidative dissolution of UO2 doped with a radioactive alpha emitter in synthetic Callovian-Oxfordian groundwater, Geochim. Cosmochim. Acta, 219 (2017) 1-21. https://doi.org/10.1016/j.gca.2017.08.043

[66] Grambow, B., Smailos, E., Geckeis, H., Müller, R., Hentschel, H., Sorption and reduction of uranium (VI) on iron corrosion products under reducing saline conditions, Radiochimica Acta, 74 (1996) 149-154. https://doi.org/10.1524/ract.1996.74.special-issue.149

[67] Cui, D., Spahiu, K., The reduction of U (VI) on corroded iron under anoxic conditions, Radiochimica Acta, 90 (2002) 623-628. https://doi.org/10.1524/ract.2002.90.9-11_2002.623

[68] Pan, Z., Bártová, B., LaGrange, T., Butorin, S.M., Hyatt, N.C., Stennett, M.C., Kvashnina, K.O., Bernier-Latmani, R., Nanoscale mechanism of UO2 formation through uranium reduction by magnetite, Nature communications, 11 (2020) 1-12. https://doi.org/10.1038/s41467-020-17795-0

[69] O'Loughlin, E.J., Kelly, S.D., Cook, R.E., Csencsits, R., Kemner, K.M., Reduction of uranium (VI) by mixed iron (II)/iron (III) hydroxide (green rust): formation of UO2 nanoparticles, Environ. Sci. Technol., 37 (2003) 721-727. https://doi.org/10.1021/es0208409

[70] Liger, E., Charlet, L., Van Cappellen, P., Surface catalysis of uranium (VI) reduction by iron (II), Geochim. Cosmochim. Acta, 63 (1999) 2939-2955. https://doi.org/10.1016/S0016-7037(99)00265-3

[71] Johnson, L., Shoesmith, D., Ewing, R., Spent fuel. In: Radioactive Waste Forms for the Future, North-Holland, Amsterdam, 635 (1988) 698.

[72] Nilsson, S., Jonsson, M., On the catalytic effects of UO2 (s) and Pd (s) on the reaction between H2O2 and H2 in aqueous solution, J. Nucl. Mater., 372 (2008) 160-163. https://doi.org/10.1016/j.jnucmat.2007.03.040

[73] King, F., Shoesmith, D., TR-04-20 Electrochemical studies of the effect of H2 on UO2 dissolution in, Swedish Nuclear Fuel and Waste Management Co., 2004.

[74] Spahiu, K., Cui, D., Lundström, M., The fate of radiolytic oxidants during spent fuel leaching in the presence of dissolved near field hydrogen, Radiochimica Acta, 92 (2004) 625-629. https://doi.org/10.1524/ract.92.9.625.54990

[75] Fors, P., Carbol, P., Van Winckel, S., Spahiu, K., Corrosion of high burn-up structured UO2 fuel in presence of dissolved H2, J. Nucl. Mater., 394 (2009) 1-8. https://doi.org/10.1016/j.jnucmat.2009.07.004

[76] Jonsson, M., Nielsen, F., Roth, O., Ekeroth, E., Nilsson, S., Hossain, M.M., Radiation induced spent nuclear fuel dissolution under deep repository conditions, Environ. Sci. Technol., 41 (2007) 7087-7093. https://doi.org/10.1021/es070832y

[77] Nilsson, S., Jonsson, M., On the catalytic effect of Pd (s) on the reduction of UO22+ with H2 in aqueous solution, J. Nucl. Mater., 374 (2008) 290-292. https://doi.org/10.1016/j.jnucmat.2007.08.010

[78] King, F., Quinn, M., Miller, N., The effect of hydrogen and gamma radiation on the oxidation of UO 2 in 0.1 mol*(dm)-3 NaCl solution, in, Swedish Nuclear Fuel and Waste Management Co., 1999.

[79] Spahiu, K., Devoy, J., Cui, D., Lundström, M., The reduction of U (VI) by near field hydrogen in the presence of UO2 (s), Radiochimica Acta, 92 (2004) 597-601. https://doi.org/10.1524/ract.92.9.597.54985

[80] Barreiro Fidalgo, A., Kumagai, Y., Jonsson, M., The role of surface-bound hydroxyl radicals in the reaction between H2O2 and UO2, J. Coord. Chem., 71 (2018) 1799-1807. https://doi.org/10.1080/00958972.2018.1466287

[81] Kumagai, Y., Barreiro Fidalgo, A., Jonsson, M., Impact of Stoichiometry on the Mechanism and Kinetics of Oxidative Dissolution of UO2 Induced by H2O2 and γ-Irradiation, J. Phys. Chem. C, 123 (2019) 9919-9925. https://doi.org/10.1021/acs.jpcc.9b00862

[82] Lousada, C.M., Trummer, M., Jonsson, M., Reactivity of H2O2 towards different UO2-based materials: The relative impact of radiolysis products revisited, J. Nucl. Mater., 434 (2013) 434-439. https://doi.org/10.1016/j.jnucmat.2011.06.003

[83] Smellie, J., Laaksoharju, M., Wikberg, P., Äspö, SE Sweden: a natural groundwater flow model derived from hydrogeochemical observations, J. Hydrol., 172 (1995) 147-169. https://doi.org/10.1016/0022-1694(95)02720-A

[84] Guillamont, R., Fanghanel, T., Grenthe, I., Neck, V., Palmer, D., Rand, M., Update on the chemical thermodynamics of uranium, neptunium, plutonium, americium and technetium, Nuclear Energy Agency Data Bank, Organization for Economic Co-operation, Development, 5 (2003).

[85] Schenk, H., Astheimer, L., Witte, E., Schwochau, K., Development of sorbers for the recovery of uranium from seawater. 1. Assessment of key parameters and screening studies of sorber materials, Sep. Sci. Technol., 17 (1982) 1293-1308.

[86] Endrizzi, F., Rao, L., Chemical speciation of uranium (VI) in marine environments: complexation of calcium and magnesium Ions with [(UO2)(CO3) 3] 4− and the effect on the extraction of uranium from seawater, Chemistry–A European Journal, 20 (2014) 14499-14506. https://doi.org/10.1002/chem.201403262

[87] Shoesmith, D., Sunder, S., Bailey, M., Wallace, G., The corrosion of nuclear fuel (UO2) in oxygenated solutions, Corros. Sci., 29 (1989) 1115-1128. https://doi.org/10.1016/0010-938X(89)90048-6

[88] Du, X., Boonchayaanant, B., Wu, W.-M., Fendorf, S., Bargar, J., Criddle, C.S., Reduction of uranium (VI) by soluble iron (II) conforms with thermodynamic predictions, Environ. Sci. Technol., 45 (2011) 4718-4725. https://doi.org/10.1021/es2006012

[89] Dewey, C., Sokaras, D., Kroll, T., Bargar, J.R., Fendorf, S., Calcium-uranyl-carbonato species kinetically limit U (VI) reduction by Fe (II) and lead to U (V)-bearing ferrihydrite, Environ. Sci. Technol., 54 (2020) 6021-6030. https://doi.org/10.1021/acs.est.9b05870

[90] Bernhard, G., Geipel, G., Brendler, V., Nitsche, H., Speciation of uranium in seepage waters of a mine tailing pile studied by time-resolved laser-induced fluorescence spectroscopy (TRLFS), Radiochimica Acta, 74 (1996) 87-92. https://doi.org/10.1524/ract.1996.74.special-issue.87

[91] Kalmykov, S.N., Choppin, G.R., Mixed Ca2+/UO22+/CO32-complex formation at different ionic strengths, Radiochimica Acta, 88 (2000) 603-608.

[92] Bernhard, G., Geipel, G., Reich, T., Brendler, V., Amayri, S., Nitsche, H., Uranyl (VI) carbonate complex formation: Validation of the Ca2UO2 (CO3) 3 (aq.) species, Radiochimica Acta, 89 (2001) 511-518. https://doi.org/10.1524/ract.2001.89.8.511

[93] Dong, W., Brooks, S.C., Determination of the formation constants of ternary complexes of uranyl and carbonate with alkaline earth metals (Mg2+, Ca2+, Sr2+, and Ba2+) using anion exchange method, Environ. Sci. Technol., 40 (2006) 4689-4695. https://doi.org/10.1021/es0606327

[94] Grenthe, I., Gaona, X., Second update on the chemical thermodynamics of uranium, neptunium, plutonium, americium and technetium, OECD/NEA Publishing, 2020. https://doi.org/10.1787/bf86a907-en

[95] Brooks, S.C., Fredrickson, J.K., Carroll, S.L., Kennedy, D.W., Zachara, J.M., Plymale, A.E., Kelly, S.D., Kemner, K.M., Fendorf, S., Inhibition of bacterial U (VI) reduction by calcium, Environ. Sci. Technol., 37 (2003) 1850-1858. https://doi.org/10.1021/es0210042

[96] Belli, K.M., DiChristina, T.J., Van Cappellen, P., Taillefert, M., Effects of aqueous uranyl speciation on the kinetics of microbial uranium reduction, Geochim. Cosmochim. Acta, 157 (2015) 109-124. https://doi.org/10.1016/j.gca.2015.02.006

[97] Fox, P.M., Davis, J.A., Zachara, J.M., The effect of calcium on aqueous uranium (VI) speciation and adsorption to ferrihydrite and quartz, Geochim. Cosmochim. Acta, 70 (2006) 1379-1387. https://doi.org/10.1016/j.gca.2005.11.027

[98] Stewart, B.D., Mayes, M.A., Fendorf, S., Impact of uranyl− calcium− carbonato complexes on uranium (VI) adsorption to synthetic and natural sediments, Environ. Sci. Technol., 44 (2010) 928-934. https://doi.org/10.1021/es902194x

[99] Shao, M.-Z., Badler, N., Spherical sampling by archimedes' theorem, Technical Reports (CIS), (1996) 184.

[100] Nielsen, F., Jonsson, M., Geometrical α-and β-dose distributions and production rates of radiolysis products in water in contact with spent nuclear fuel, J. Nucl. Mater., 359 (2006) 1-7. https://doi.org/10.1016/j.jnucmat.2006.08.001

[101] Toftegaard, J., Lühr, A., Sobolevsky, N., Bassler, N., Improvements in the stopping power library libdEdx and release of the web GUI dedx. au. dk, in: J. Phys. Conf. Ser., IOP Publishing, 2014, pp. 012003. https://doi.org/10.1088/1742-6596/489/1/012003

[102] Elliot, A.J., Chenier, M.P., Radiolysis of 4.5 mol dm− 3 LiOH with 6Li (n, α) 3H ion recoil, J. Nucl. Mater., 187 (1992) 230-238. https://doi.org/10.1016/0022-3115(92)90502-C

[103] Buxton, G.V., Greenstock, C.L., Helman, W.P., Ross, A.B., Critical review of rate constants for reactions of hydrated electrons, hydrogen atoms and hydroxyl radicals (· OH/· O− in aqueous solution, J. Phys. Chem. Ref. Data, 17 (1988) 513-886. https://doi.org/10.1063/1.555805

[104] Mezyk, S.P., Bartels, D.M., Direct EPR measurement of Arrhenius parameters for the reactions of H˙ atoms with H 2 O 2 and D˙ atoms with D 2 O 2 in aqueous solution, J. Chem. Soc., Faraday Trans., 91 (1995) 3127-3132. https://doi.org/10.1039/FT9959103127

[105] Elliot, A.J., Buxton, G.V., Temperature dependence of the reactions OH + O and OH + HO2 in water up to 200 °C, J. Chem. Soc., Faraday Trans., 88 (1992) 2465-2470. https://doi.org/10.1039/FT9928802465

[106] Cai, Z., Li, X., Katsumura, Y., Urabe, O., Radiolysis of bicarbonate and carbonate aqueous solutions: product analysis and simulation of radiolytic processes, Nucl. Technol., 136 (2001) 231-240. https://doi.org/10.13182/NT01-A3241

[107] Hossain, M.M., Ekeroth, E., Jonsson, M., Effects of HCO3-on the kinetics of UO2 oxidation by H2O2, J. Nucl. Mater., 358 (2006) 202-208. https://doi.org/10.1016/j.jnucmat.2006.07.008

[108] Nielsen, F., Lundahl, K., Jonsson, M., Simulations of H_2O_2 concentration profiles in the water surrounding spent nuclear fuel, J. Nucl. Mater., 372 (2008) 32-35. https://doi.org/10.1016/j.jnucmat.2007.01.279

[109] Trummer, M., Jonsson, M., Resolving the H2 effect on radiation induced dissolution of UO2-based spent nuclear fuel, J. Nucl. Mater., 396 (2010) 163-169. https://doi.org/10.1016/j.jnucmat.2009.10.067

[110] Trummer, M., Nilsson, S., Jonsson, M., On the effects of fission product noble metal inclusions on the kinetics of radiation induced dissolution of spent nuclear fuel, J. Nucl. Mater., 378 (2008) 55-59. https://doi.org/10.1016/j.jnucmat.2008.04.018

[111] Trummer, M., Roth, O., Jonsson, M., H2 inhibition of radiation induced dissolution of spent nuclear fuel, J. Nucl. Mater., 383 (2009) 226-230. https://doi.org/10.1016/j.jnucmat.2008.09.021

[112] Hollander, J.M., Jolly, W.L., X-ray photoelectron spectroscopy, Acc. Chem. Res., 3 (1970) 193-200. https://doi.org/10.1021/ar50030a003

[113] Ilton, E.S., Bagus, P.S., XPS determination of uranium oxidation states, Surf. Interface Anal., 43 (2011) 1549-1560.

[114] Teterin, Y.A., Popel, A.J., Maslakov, K.I., Teterin, A.Y., Ivanov, K.E., Kalmykov, S.N., Springell, R., Scott, T.B., Farnan, I., XPS study of ion irradiated and unirradiated UO2 thin films, Inorg. Chem., 55 (2016) 8059-8070.

[115] Cox, L., Farr, J., 4f binding-energy shifts of the light-actinide dioxides and tetrafluorides, Phys. Rev. B, 39 (1989) 11142. https://doi.org/10.1103/PhysRevB.39.11142

[116] Maslakov, K.I., Teterin, Y.A., Stefanovsky, S.V., Kalmykov, S.N., Teterin, A.Y., Ivanov, K.E., XPS study of uranium-containing sodium-aluminum-iron-phosphate glasses, J. Alloys Compd., 712 (2017) 36-43.

[117] Van den Berghe, S., Laval, J.-P., Gaudreau, B., Terryn, H., Verwerft, M., XPS investigations on cesium uranates: mixed valency behaviour of uranium, J. Nucl. Mater., 277 (2000) 28-36. https://doi.org/10.1016/S0022-3115(99)00146-4

[118] Odorowski, M., Jégou, C., De Windt, L., Broudic, V., Peuget, S., Magnin, M., Tribet, M., Martin, C., Oxidative dissolution of unirradiated Mimas MOX fuel (U/Pu oxides) in carbonated water under oxic and anoxic conditions, J. Nucl. Mater., 468 (2016) 17-25. https://doi.org/10.1016/j.jnucmat.2015.09.059

[119] Lucuta, P., Verrall, R., Matzke, H., Palmer, B., Microstructural features of SIMFUEL—simulated high-burnup UO2-based nuclear fuel, J. Nucl. Mater., 178 (1991) 48-60. https://doi.org/10.1016/0022-3115(91)90455-G

[120] Nassar, M.Y., Ahmed, I.S., Mohamed, T.Y., Khatab, M., A controlled, template-free, and hydrothermal synthesis route to sphere-like α-Fe 2 O 3 nanostructures for textile dye removal, Rsc Advances, 6 (2016) 20001-20013. https://doi.org/10.1039/C5RA26112K

[121] Laaksoharju, M., Smellie, J., Tullborg, E.-L., Gimeno, M., Hallbeck, L., Molinero, J., Waber, N., Bedrock hydrogeochemistry Forsmark. Site descriptive modelling SDM-Site Forsmark, (2008).

[122] Willey, T.M., Vance, A.L., Van Buuren, T., Bostedt, C., Terminello, L., Fadley, C., Rapid degradation of alkanethiol-based self-assembled monolayers on gold in ambient laboratory conditions, Surf. Sci., 576 (2005) 188-196. https://doi.org/10.1016/j.susc.2004.12.022

[123] Seah, M., Summary of ISO/TC 201 Standard: VII ISO 15472: 2001—surface chemical analysis—x-ray photoelectron spectrometers—calibration of energy scales, Surface and Interface Analysis: An International Journal devoted to the development and application of techniques for the analysis of surfaces, interfaces and thin films, 31 (2001) 721-723.

[124] Yamada, N., Kinetic energy discrimination in collision/reaction cell ICP-MS: Theoretical review of principles and limitations, Spectrochimica Acta Part B: Atomic Spectroscopy, 110 (2015) 31-44. https://doi.org/10.1016/j.sab.2015.05.008

[125] Allen, A.O., Hochanadel, C., Ghormley, J., Davis, T., Decomposition of water and aqueous solutions under mixed fast neutron and γ-radiation, J. Phys. Chem., 56 (1952) 575-586. https://doi.org/10.1021/j150497a007

[126] Hochanadel, C., Effects of cobalt γ-radiation on water and aqueous solutions, J. Phys. Chem., 56 (1952) 587-594. https:/doi.org/10.1021/j150497a008

[127] Ghormley, J., Stewart, A., Effects of γ-Radiation on Ice, Journal of the American Chemical Society, 78 (1956) 2934-2939. https://doi.org/10.1021/ja01594a004

[128] Kerleguer, V., Jégou, C., De Windt, L., Broudic, V., Jouan, G., Miro, S., Tocino, F., Martin, C., The mechanisms of alteration of a homogeneous U0. 73Pu0. 27O2 MOx fuel under alpha radiolysis of water, J. Nucl. Mater., 529 (2020) 151920. https://doi.org/10.1016/j.jnucmat.2019.151920

[129] Hansson, N., Ekberg, C., Spahiu, K., Alpha dose rate calculations for UO_2 based materials using stopping power models, Nucl. Mater. Energy, 22 (2020) 100734. https://doi.org/10.1016/j.nme.2020.100734

[130] Grenthe, I., Ferri, D., Salvatore, F., Riccio, G., Studies on metal carbonate equilibria. Part 10. A solubility study of the complex formation in the uranium (VI)–water–carbon dioxide (g) system at 25° C, J. Chem. Soc., Dalton Trans., (1984) 2439-2443. https://doi.org/10.1039/DT9840002439

[131] Ekeroth, E., Jonsson, M., Oxidation of UO2 by radiolytic oxidants, J. Nucl. Mater., 322 (2003) 242-248. https://doi.org/10.1016/j.jnucmat.2003.07.001

[132] De Pablo, J., Casas, I., Clarens, F., El Aamrani, F., Rovira, M., The effect of hydrogen peroxide concentration on the oxidative dissolution of unirradiated uranium dioxide, Mater. Res. Soc. Symp. Proc., 663 (2000). https://doi.org/10.1557/PROC-663-409

[133] Ekeroth, E., Jonsson, M., Eriksen, T.E., Ljungqvist, K., Kovács, S., Puigdomenech, I., Reduction of UO22+ by H2, Journal of Nuclear Materials, 334 (2004) 35-39.

[134] Allen, G.C., Crofts, J.A., Curtis, M.T., Tucker, P.M., Chadwick, D., Hampson, P.J., X-ray photoelectron spectroscopy of some uranium oxide phases, J. Chem. Soc., Dalton Trans., (1974) 1296-1301. https://doi.org/10.1039/DT9740001296

[135] Ilton, E.S., Bagus, P.S., Many-body effects in the 4 f x-ray photoelectron spectroscopy of the U 5+ and U 4+ free ions, Phys. Rev. B, 71 (2005) 195121.

[136] Gouder, T., Eloirdi, R., Caciuffo, R., Direct observation of pure pentavalent uranium in U2O5 thin films by high resolution photoemission spectroscopy, Scientific reports, 8 (2018) 1-7. https://doi.org/10.1038/s41598-018-26594-z

[137] Bénézeth, P., Dandurand, J., Harrichoury, J., Solubility product of siderite (FeCO3) as a function of temperature (25–250 C), Chem. Geol., 265 (2009) 3-12. https://doi.org/10.1016/j.chemgeo.2009.03.015

[138] Chaves, L.H., The role of green rust in the environment: a review, Revista Brasileira de Engenharia Agrícola e Ambiental, 9 (2005) 284-288. https://doi.org/10.1590/S1415-43662005000200021

[139] Taylor, R., McKenzie, R., The influence of aluminum on iron oxides. VI. The formation of Fe (II)-Al (III) hydroxy-chlorides,-sulfates, and-carbonates as new members of the pyroaurite group and their significance in soils, Clays Clay Miner., 28 (1980) 179-187. https://doi.org/10.1346/CCMN.1980.0280303

[140] Kato, M., Konashi, K., Lattice parameters of (U, Pu, Am, Np) O2− x, J. Nucl. Mater., 385 (2009) 117-121. https://doi.org/10.1016/j.jnucmat.2008.09.037

[141] Wyckoff, R., Crystal structures, 1: New York, Fluorite structure, New York, Interscience Publishers, (1963) 239-444.

[142] Schwertmann, U., Transformation of hematite to goethite in soils, Nature, 232 (1971) 624-625. https://doi.org/10.1038/232624a0

[143] Giammar, D.E., Hering, J.G., Time scales for sorption− desorption and surface precipitation of uranyl on goethite, Environ. Sci. Technol., 35 (2001) 3332-3337. https://doi.org/10.1021/es0019981

[144] Sander, R., Compilation of Henry's law constants (version 4.0) for water as solvent, Atmospheric Chem. Phys., 15 (2015) 4399-4981. https://doi.org/10.5194/acp-15-4399-2015

[145] Matsugi, A., Suma, K., Miyoshi, A., Deuterium kinetic isotope effects on the gas-phase reactions of C 2 H with H 2 (D 2) and CH 4 (CD 4), Physical Chemistry Chemical Physics, 13 (2011) 4022-4031. https://doi.org/10.1039/C0CP02056G

[146] Jang, J.-H., Dempsey, B.A., Burgos, W.D., Solubility of schoepite: comparison and selection of complexation constants for U (VI), Water Res., 40 (2006) 2738-2746. https://doi.org/10.1016/j.watres.2006.04.014

[147] Carbol, P., Fors, P., Gouder, T., Spahiu, K., Hydrogen suppresses UO2 corrosion, Geochim. Cosmochim. Acta, 73 (2009) 4366-4375. https://doi.org/10.1016/j.gca.2009.04.041

[148] Zuo, Z., Cai, Z., Katsumura, Y., Chitose, N., Muroya, Y., Reinvestigation of the acid–base equilibrium of the (bi) carbonate radical and pH dependence of its reactivity with inorganic reactants, Radiat. Phys. Chem., 55 (1999) 15-23. https://doi.org/10.1016/S0969-806X(98)00308-9

Appendix A – Concentration series

Iron foil experiment batch M-P

Experiment series M-P which was significantly influenced by O_2-contamination in the order of 80 ppm around 600 – 800 h is shown in Figure A.1.

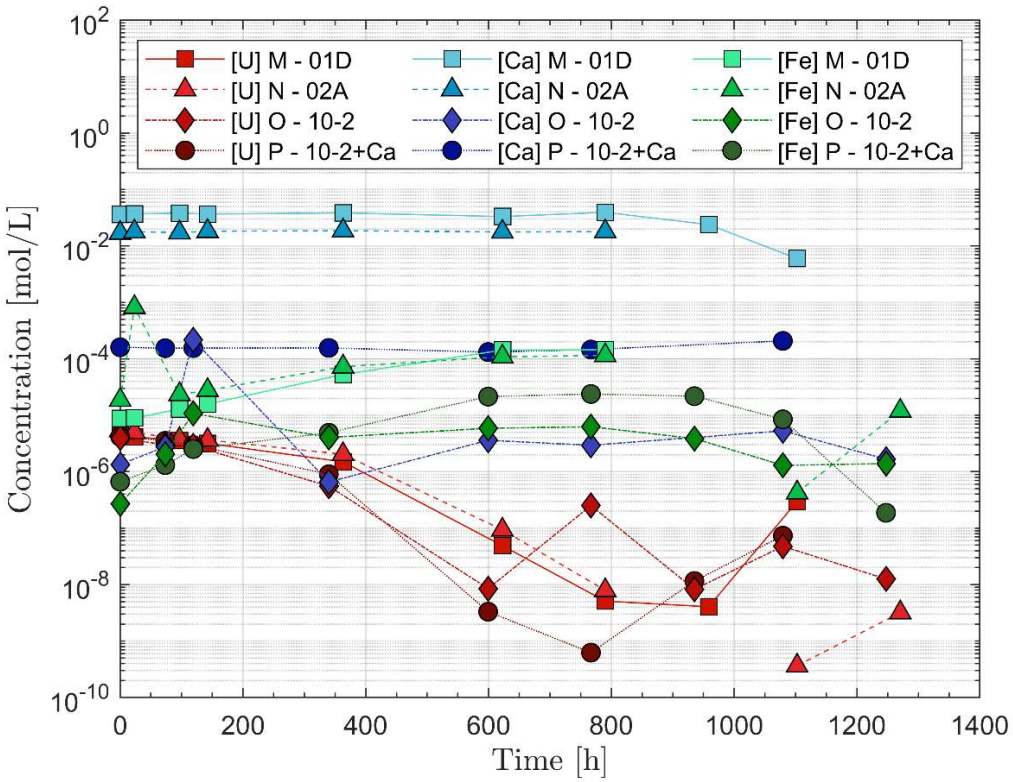

Figure A.1. 400 ppm CO_2 in Ar atmosphere batch samples M-P using the $FeCO_3$ O_2-trap. O_2-contamination after 600-800 h led to comparatively high uranium concentrations in solution.

MOX pellet leaching under D_2 atmosphere

The 8 bar D_2 experiment using the 10 wt.% Pu-doped MOX pellet with a plateau of ~$4 \cdot 10^{-7}$ M is shown in Figure A.2.

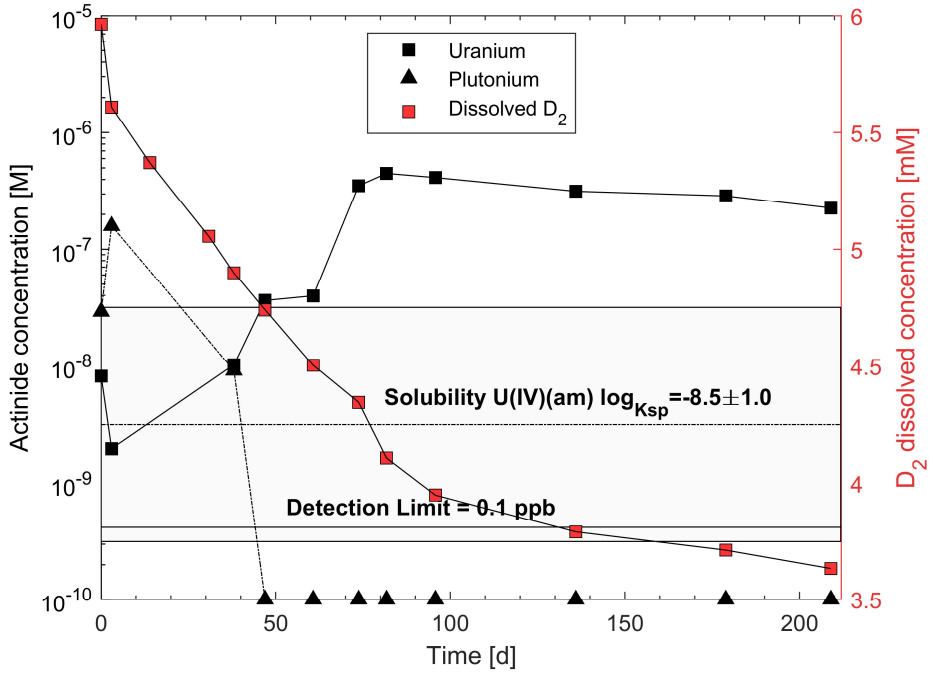

Figure A.2. 10 wt.% Pu-doped MOX under 8 bar initial D_2 pressure. The solution consists of 10 mM NaCl and 2mM $NaHCO_3$.

The 15 bar D_2 experiment showing a quite significant D_2 leakage and increase of dissolved uranium concentrations followed by a significant decrease in uranium concentrations.

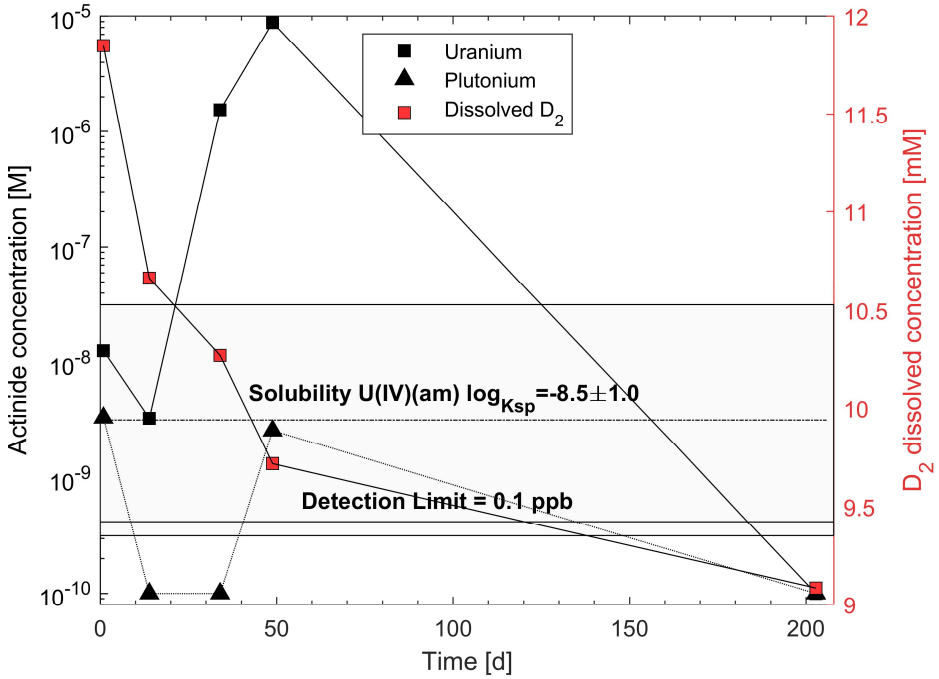

Figure A.3. 15 bar D_2 experiment using the 24 wt.% Pu-doped MOX pellet. The dissolved uranium concentration is affected by the corrosion of the stainless-steel components of the autoclave system.

Appendix B – Kinetic model

The kinetic reaction rate system discussed in Chapters 3.1 and 6.7.1 is shown in Table S.1 below.

Table S.1. Reactions and rate constants used in the kinetic model

Reaction number	Reaction	Rate constant ($M^{-1}\cdot s^{-1}$ or s^{-1})
	Radiolysis Product Reactions [102-105]	
kW	$H^+ + OH^- \rightarrow H_2O$	1.43e11
kWr	$H_2O \rightarrow H^+ + OH^-$	2.6e-5
k1	$e_{aq}^- + H_2O \rightarrow H\cdot + OH^-$	1.9e1
k2	$2e_{aq}^- + 2H_2O \rightarrow H_2 + 2OH^-$	1.1e10 (2k)
k3	$e_{aq}^- + H\cdot \rightarrow H_2 + OH^-$	2.5e10
k4	$e_{aq}^- + OH\cdot \rightarrow OH^-$	3.0e10
k5	$e_{aq}^- + O^- \rightarrow 2OH^-$	2.2e10
k6	$e_{aq}^- + H^+ \rightarrow H\cdot$	2.3e10
k7	$e_{aq}^- + H_2O_2 \rightarrow OH^- + OH\cdot$	1.1e10
k8	$e_{aq}^- + HO_2^- \rightarrow O^- + OH^-$	3.5e9
k8b	$e_{aq}^- + HO_2\cdot \rightarrow HO_2^-$	2.0e10
k9	$e_{aq}^- + O_2 \rightarrow O_2^-$	1.9e10
k10	$e_{aq}^- + O_2^- \rightarrow HO_2^- + OH^-$	1.3e10
k11	$H\cdot + H_2O \rightarrow H_2 + OH\cdot$	1.1e1
k12	$H\cdot + H\cdot \rightarrow H_2$	1.55e10 (2k)
k13	$H\cdot + OH\cdot \rightarrow H_2O$	7.0e9
k14	$H\cdot + OH^- \rightarrow e_{aq}^-$	2.2e7
k15	$H\cdot + H_2O_2 \rightarrow OH\cdot + H_2O$	9.0e7
k16	$H\cdot + O_2 \rightarrow HO_2\cdot$	2.1e10
k16b	$H\cdot + O_2^- \rightarrow HO_2^-$	1.8e10
k17	$H\cdot + HO_2\cdot \rightarrow H_2O_2$	1.8e10
k18	$OH\cdot + OH\cdot \rightarrow H_2O_2$	3.6e10 (2k)
k19	$OH\cdot + O^- \rightarrow HO_2^-$	2.5e10
k20	$OH\cdot + H_2 \rightarrow H\cdot + H_2O$	4.3e7
k21	$OH\cdot + OH^- \rightarrow O^- + H_2O$	1.3e10
k22	$OH\cdot + H_2O_2 \rightarrow H_2O + HO_2\cdot$	2.7e7
k23	$OH\cdot + HO_2^- \rightarrow OH^- + HO_2\cdot$	7.5e9
k24	$HO_2^- + H_2O \rightarrow H_2O_2 + OH^-$	5.74e4
k25	$OH\cdot + HO_2\cdot \rightarrow H_2O + O_2$	6.0e9
k26	$OH\cdot + O_2^- \rightarrow OH^- + O_2$	8.2e9
k27	$O^- + H_2O \rightarrow OH^- + OH\cdot$	1.86e6
k28	$O^- + O^- \rightarrow HO_2^- + OH^-$	1.0e9
k29	$O^- + H_2 \rightarrow H\cdot + OH^-$	8.0e7
k30	$O^- + H_2O_2 \rightarrow O_2^- + H_2O$	5.0e8
k31	$O^- + HO_2^- \rightarrow O_2^- + OH^-$	4.0e8
k32	$O^- + O_2 \rightarrow O_3^-$	3.6e9
k33	$O^- + O_2^- \rightarrow 2OH^- + O_2$	6.0e8
kL9	$H_2O_2 \rightarrow H^+ + HO_2^-$	0.112
kL10	$H^+ + HO_2^- \rightarrow H_2O_2$	5.0e10
kL11	$H_2O_2 + OH^- \rightarrow HO_2^- + H_2O$	1.3e10
kL15	$H\cdot \rightarrow e_{aq}^- + H^+$	3.91
kL20	$O^- + H^+ \rightarrow OH\cdot$	1.0e11
kL21	$HO_2 \rightarrow O_2^- + H^+$	1.35e6
kL22	$O_2^- + H^+ \rightarrow HO_2$	5.0e10
kL23	$HO_2 + OH^- \rightarrow O_2^- + H_2O$	5.0e10
kL24	$O_2^- + H_2O \rightarrow HO_2 + OH^-$	18.62
kL34	$e_{aq}^- + O_3^- \rightarrow O_2 + 2OH^-$	1.6e10
kL35	$e_{aq} + O_3 \rightarrow O_3^-$	3.6e10
kL36	$H\cdot + H_2O \rightarrow H_2 + OH\cdot$	1.1e1
kL37	$H\cdot + O^- \rightarrow OH^-$	1.0e10
kL38	$H\cdot + HO_2^- \rightarrow OH\cdot + OH^-$	9.0e7
kL39	$H\cdot + O_3^- \rightarrow OH^- + O_2$	1.0e10
kL46	$H\cdot + O_3 \rightarrow HO_3$	3.8e10
kL54	$OH\cdot + O_3^- \rightarrow O_3 + OH^-$	2.6e9
kL55	$OH\cdot + O_3^- \rightarrow 2O_2^- + H^+$	6.0e9
kL56	$OH\cdot + O_3 \rightarrow HO_2 + O_2$	1.1e8
kL57	$HO_2 + O_2^- \rightarrow HO_2^- + O_2$	8.0e7
kL58	$HO_2 + HO_2 \rightarrow H_2O_2 + O_2$	7.0e5
kL59	$HO_2 + O^- \rightarrow O_2 + OH^-$	6.0e9
kL60	$HO_2 + H_2O_2 \rightarrow OH\cdot + O_2 + H_2O$	5.0e-1
kL61	$HO_2 + HO_2^- \rightarrow OH\cdot + O_2 + OH^-$	5.0e-1
kL62	$HO_2 + O_3^- \rightarrow 2O_2 + OH^-$	6.0e9
kL63	$HO_2 + O_3 \rightarrow HO_3 + O_2$	5.0e8

kL64	$2O_2^- + 2H_2O \rightarrow H_2O_2 + O_2 + OH^-$	1.0e2
kL66	$O_2^- + H_2O_2 \rightarrow OH\cdot + O_2 + OH^-$	1.3e-1
kL67	$O_2^- + HO_2^- \rightarrow O\cdot^- + O_2 + OH^-$	1.3e-1
kL68	$O_2^- + O_3 \rightarrow 2O_2 + 2OH^-$	1.0e3
kL69	$O_2^- + O_3 \rightarrow O_3^- + O_2$	1.5e9
kL75	$O^- + O_3 \rightarrow 2O_2^-$	7.0e8
kL78	$O_3^- + H^+ \rightarrow O_2 + OH\cdot$	9.0e10
kL79	$HO_3 \rightarrow O_2 + OH\cdot$	1.1e5
	Surface Reactions [107]	Rate constant ($m \cdot s^{-1}$)
kU1	$UO_2 + H_2O_2 \rightarrow UO_2^{2+} + 2OH^-$	7.56e-8
	Carbonate Reactions [106]	Rate constant ($M^{-1} \cdot s^{-1}$ or s^{-1})
k36	$CO_2 + H_2O \rightarrow HCO_3^- + H^+$	2.0e4
k37	$HCO_3^- + H^+ \rightarrow CO_2 + H_2O$	5.0e10
k38	$HCO_3^- \rightarrow CO_3^{2-} + H^+$	2.0e0
k39	$CO_3^{2-} + H^+ \rightarrow HCO_3^-$	5.0e10
k40	$CO_2 + e_{aq}^- \rightarrow CO_2^-$	7.7e9
k41	$CO_3^{2-} + e_{aq}^- \rightarrow CO_2^- + 2OH^-$	3.9e5
k42	$HCO_3^- + H\cdot \rightarrow CO_3^- + H_2$	4.4e4
k43	$HCO_3^- + OH\cdot \rightarrow CO_3^- + H_2O$	8.5e6
k44	$CO_3^{2-} + OH\cdot \rightarrow CO_3^- + OH^-$	3.9e8
k45	$2CO_3^{2-} \rightarrow C_2O_6^{2-}$	1.4e7
k46	$C_2O_6^{2-} \rightarrow C_2O_4^{2-} + O_2$	1.0e0
k46b	$C_2O_6^{2-} + H_2O \rightarrow HO_2^- + OH^- + 2CO_2$	2.0e2
k47	$CO_3^- + H_2O_2 \rightarrow CO_3^{2-} + O_2^- + 2H^+$	9.8e5 [148]
k48	$CO_3^- + HO_2^- \rightarrow CO_3^{2-} + O_2^- + H^+$	1.0e7
k49	$CO_3^- + O_2^- \rightarrow CO_3^{2-} + O_2$	4.0e8
k50	$CO_3^- + CO_2^- \rightarrow CO_3^{2-} + CO_2$	3.0e8
k51	$CO_2^- + e_{aq}^- \rightarrow HCOO^- + OH^-$	9.0e8
k52	$2CO_2^- \rightarrow C_2O_4^{2-}$	6.5e8
k53	$CO_2^- + H_2O_2 \rightarrow CO_2 + OH\cdot + OH^-$	7.3e5
k54	$CO_2^- + HCO_3^- \rightarrow CO_3^- + HCOO^-$	1.0e3
k55	$CO_3^- + HCOO^- \rightarrow HCO_3^- + CO_2^-$	1.5e5
k56	$OH\cdot + HCOO^- \rightarrow CO_2^- + H_2O$	3.2e9
k57	$H\cdot + HCOO^- \rightarrow CO_2^- + H_2$	2.1e8
k58	$e_{aq}^- + HCOO^- \rightarrow CO_2^- + H^+$	8.0e3
k59	$OH\cdot + C_2O_4^{2-} \rightarrow CO_2^- + CO_2 + OH^-$	4.0e7
k60	$CO_2^- \rightarrow O_2 \rightarrow CO_2 + O_2^-$	2.0e9
k61	$CO_3^- + C_2O_4^{2-} \rightarrow C_2O_4^- + CO_3^{2-}$	3.0e3